

Measurement of the D^{*+} -meson production in
Pb–Pb collisions at $\sqrt{s_{\text{NN}}} = 5.02$ TeV with ALICE

Syaefudin Jaelani

Copyright © 2021 by Syaefudin Jaelani
All rights reserved

No part of this publication may be reproduced, stored in a retrieval system, or transmitted in any form or by any means, electronic, mechanical, photocopying, recording or otherwise, without the prior permission in writing from the author.

Cover designed by Yan Fahmi
Layout by www.LaTeXTemplates.com
Printed by ProefschriftMaken
ISBN: 978-94-6423-310-0

**Measurement of the D^{*+} -meson production in
Pb–Pb collisions at $\sqrt{s_{\text{NN}}} = 5.02$ TeV with ALICE**

**Meting van de productie van D^{*+} mesonen in
Lood-Lood botsingen met $\sqrt{s_{\text{NN}}} = 5.02$ TeV met
ALICE**

(met een samenvatting in het Nederlands)

Proefschrift

ter verkrijging van de graad van doctor aan de

Universiteit Utrecht

op gezag van de

rector magnificus, prof.dr. H.R.B.M. Kummeling,

ingevolge het besluit van het college voor promoties

in het openbaar te verdedigen op

woensdag 30 juni 2021 des middags te 12.15 uur

door

Syaefudin Jaelani

geboren op 28 februari 1989

te Tangerang, Indonesië

Promotor:

Prof. dr. R.J.M. Snellings

Copromotor:

Dr. A. Grelli

Abstract

In the Standard Model of particle physics, Quantum Chromodynamics (QCD) is the theory describing the strong interaction among quarks and gluons. Under extreme conditions of temperature and/or pressure, QCD predicts a phase transition from ordinary matter to the so-called Quark-Gluon Plasma (QGP), in which quarks and gluons are deconfined.

QGP can be created at accelerators, like the Large Hadron Collider at CERN, by colliding heavy-ion at ultra-relativistic speed. Due to its short lifetime, the QGP cannot be observed directly and, therefore, the investigation of its properties proceeds by means of probes. The idea is that quarks interact with the hot and dense medium losing energy in the process and acquiring collective features. Afterward, once the plasma cools down below a certain temperature, they dress to form hadrons. By investigating the properties of those hadrons with respect to reference properties evaluated in a system where QGP is not created, it is possible to infer information on the plasma thermodynamical and transport properties.

A well established experimental observable is the so-called nuclear modification factor. It is based on the comparison of the yield of particles produced in heavy-ion collisions to a reference evaluated in proton-proton collisions. In this thesis dissertation, we will discuss recent measurements of the D^{*+} meson production in lead-lead collisions at $\sqrt{s_{NN}} = 5.02$ TeV and relative nuclear modification factor. In addition, the detailed comparison with theoretical models will be discussed.

Contents

Abstract	iii
1 Heavy-ion physics	1
1.1 Introduction to the Quark-Gluon Plasma	1
1.2 In-medium energy loss	5
1.2.1 General overview	5
1.2.2 Implementation of heavy-quark energy loss in models	7
1.3 Signatures of Quark-Gluon Plasma	8
1.3.1 Nuclear modification factor	8
1.3.2 Azimuthal anisotropy	9
2 The ALICE detector	11
2.1 Inner Tracking System	13
2.2 Time Projection Chamber	15
2.3 Time-Of-Flight	17
2.4 V0	18
3 Pb–Pb data samples at $\sqrt{s_{\text{NN}}} = 5.02$ TeV	21
3.1 Triggering	21
3.2 Quality assurance	23
3.2.1 2015 data sample	25
3.2.2 2018 data sample	26
4 D^{*+} analysis	27
4.1 D^{*+} reconstruction	27
4.2 D^0 reconstruction	29
4.3 Selection criteria	29
4.3.1 Event selection	30
4.3.2 Track selection	30
4.3.3 Particle identification	31
4.3.4 Topological selection	31
4.4 D^{*+} yield extraction	34
4.4.1 Invariant mass analysis	34
4.4.2 Signal extraction	34
4.5 Corrections	35

5	D^{*+} analysis using Pb–Pb 2015 data sample	39
5.1	Introduction	39
5.2	Raw yield extraction	41
5.3	Efficiencies	44
5.4	Systematic uncertainties	46
5.5	D ^{*+} corrected transverse momentum distributions	54
5.6	Proton-proton reference	56
5.7	D ^{*+} meson nuclear modification factor	57
5.8	Average nuclear modification factor (D ⁰ , D ⁺ and D ^{*+})	58
5.9	D mesons nuclear modification factor vs models	60
6	High precision measurements using Pb–Pb 2018 data sample	63
6.1	Introduction	63
6.2	Raw yield extraction	66
6.3	Efficiencies	70
6.4	Systematic uncertainties	71
6.5	D ^{*+} transverse momentum distributions	77
6.6	Proton-proton reference: with 2017 pp at $\sqrt{s_{NN}} = 5.02$ TeV data sample	79
6.7	D meson nuclear modification factor	80
6.8	Heavy vs light flavour sector	81
6.9	Comparison with theory and investigation of hadronisation via recombination	82
6.10	D ^{*+} meson nuclear modification factor as a function of centrality	86
7	Conclusions and outlook	91
7.1	Conclusions	91
7.2	Future direction	93
	Bibliography	99
	Summary in English	105
	Samenvatting in het Nederlands	107
	Curriculum Vitae	109
	Acknowledgements	111

Chapter 1

Heavy-ion physics

1.1 Introduction to the Quark-Gluon Plasma

Theoretical and experimental advances in our understanding of the fundamental structure of matter made in the second half of the past century, have led to the so-called “Standard Model of particle physics”. Over the last five decades almost all the experimental results confirmed the validity of the model predictions making it the best established theory of fundamental particles and their interactions. Developed in the late seventies, it successfully describes three of the four fundamental forces and classifies all the known elementary particles. The Standard Model categorizes the components of matter into two types of particles: quarks and leptons. Both of them are fermions, which have half-integer spin and follow Fermi-Dirac statistics. Both quarks and leptons interact with each other via boson exchange. Leptons interact weakly via W^+ , W^- , Z^0 exchange, and electromagnetically via γ exchange. In addition, quarks interact via gluon exchange and the corresponding fundamental force is known as “strong interaction”. The elementary particle classification is shown in figure 1.1 as well as listed in Table 1.1.

The strong interaction between quarks and gluons is described by Quantum Chromodynamics (QCD). In particle physics, quarks and gluons are collectively called partons and are considered the elementary constituents of the hadrons. Quarks have various intrinsic properties, such as electric charge, mass, colour charge, and spin. Colour charge comes in three states: red (r), green (g), and blue (b). The exchange particles,

Flavour	Charge (e)	Bare mass (MeV/c^2)	Constituent mass (MeV/c^2)
up	$+\frac{2}{3}$	$2.3^{+0.7}_{-0.5}$	220-360
down	$-\frac{1}{3}$	$4.8^{+0.5}_{-0.3}$	220-360
charm	$+\frac{2}{3}$	1275 ± 25	1550-1710
strange	$-\frac{1}{3}$	95 ± 5	419-540
top	$+\frac{2}{3}$	$173210 \pm 510 \pm 710$	-
beauty	$-\frac{1}{3}$	4180 ± 30	~ 4000

TABLE 1.1: Quarks with their charges, bare masses [1] and constituent masses [2, 3].

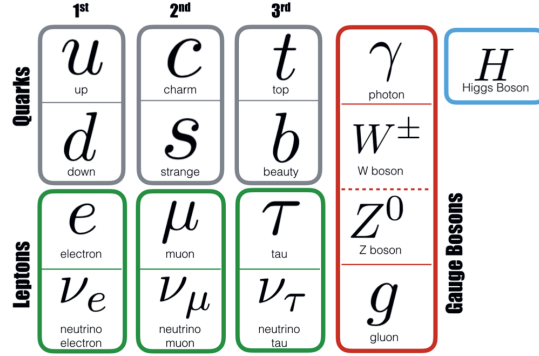


FIGURE 1.1: The elementary particles of the Standard Model. Figure from [4].

the gluons, also carry the colour charge of the strong interaction. This makes gluons qualitatively different from the exchange particle in Quantum Electrodynamics, the photon, which mediates the electromagnetic interaction but carries no charge. Quarks cannot be observed freely. They are confined inside mesons and baryons. A meson is composed of a quark-antiquark pair, while a baryon consists of three quarks that carry three different colours. Gluons can produce quark-antiquark pairs. At any given momentum, there is a probability that a proton contains extra quark pairs, i.e. $u\bar{u}$, or $d\bar{d}$, or $s\bar{s}$. In addition, it can contain even heavier quark pairs though the possibility is very small because of their large masses, i.e. $c\bar{c}$, or $b\bar{b}$, or $t\bar{t}$. The quarks that contribute to the quantum numbers of hadrons are called valence quarks, while the additional $q\bar{q}$ pairs that do not influence the quantum numbers are called sea quarks.

All quarks, along with their masses and charges, are listed in Table 1.1. The Standard Model predicts that the mass of quarks is determined by the combination of their coupling to the Higgs field (the bare masses) and spontaneous chiral symmetry breaking. Figure 1.2 shows the Higgs component of the quark mass on the y -axis and the total quark mass on the x -axis. The heavy-quark masses (c , b , and t) are due to Higgs coupling in the electroweak sector, while the light-quark masses (u , d , and s) have a significant contribution from chiral symmetry breaking in the QCD vacuum.

Due to confinement, quarks cannot be observed experimentally as free particles. Their properties can be deduced from observing the behaviour of hadrons. This is studied via the properties of the QCD interaction potential between a quark-antiquark pair, expressed by:

$$V_{\text{QCD}}(r) = -\frac{4\alpha_s}{3r} + \sigma \cdot r, \quad (1.1)$$

where V_{QCD} is the QCD potential between the quark and antiquark, r is the distance

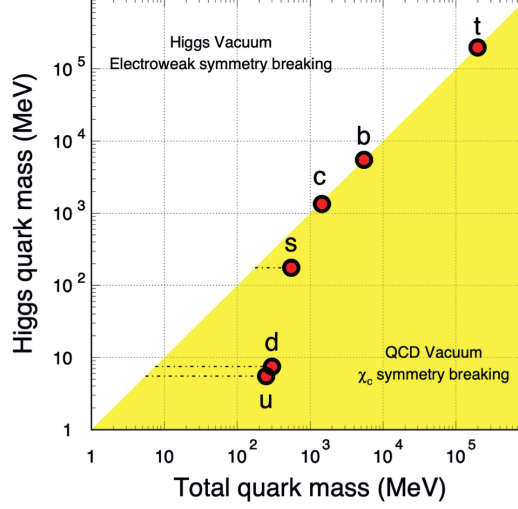


FIGURE 1.2: Plot of quark masses in the Higgs vacuum (y -axis) and in the QCD vacuum (x -axis). For the light quarks (u , d , s), a large proportion of their masses arises due to chiral symmetry breaking in the QCD vacuum [2].

between the two of them, α_s is the QCD coupling and σ is the QCD string tension. The first term in Eq.1.1 is known as a Coulomb-like term with a $1/r$ component. This component $1/r$ arises from the exchange of a single massless spin-1 boson.

The coupling constant α_s is a function of r , the distance between the two partons. This variation, expressed as a function of the four-momentum transfer Q^2 , is shown in figure 1.3 and usually referred as “running coupling constant”. Large Q^2 values correlate with higher collision energies and smaller separation between partons, while small Q^2 values relate to lower collision energies and larger separation between partons.

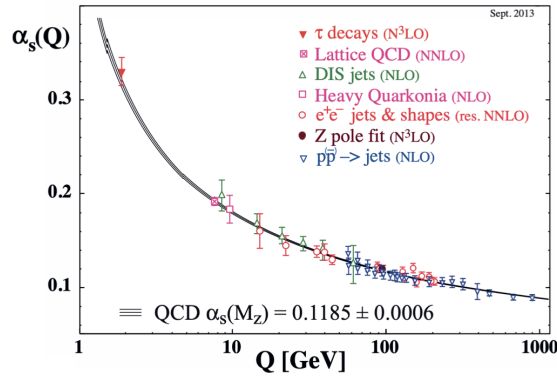


FIGURE 1.3: Running of the QCD coupling constant α_s as a function of the four-momentum transfer Q^2 [3].

The strength of α_s can be determined by perturbative QCD (pQCD) calculations. The running coupling constant α_s can be expressed in terms of the four-momentum transfer of the gluons as follows [5]

$$\alpha_s(Q^2) = \frac{12\pi}{(33 - 2n_f)\ln(Q^2/\Lambda_{\text{QCD}}^2)}, \quad (1.2)$$

where n_f is the number of active quark flavors and Λ_{QCD} is the QCD scale parameter, which represents the momentum scale at which the perturbative coupling $\alpha_s(Q^2)$ becomes divergent. Λ_{QCD} is a free parameter, which is determined from experimental data, and is of the order of ~ 200 MeV [3]. This behaviour of the running coupling constant has been verified at various energy scales using results from relativistic colliders, as shown in Fig. 1.3 [3]. In Eq. 1.1, the second term will dominate at large separation between quark and antiquark. It leads to a linear increase of the QCD potential as a function of r . Therefore, the quarks require an infinite amount of energy to be freed from this potential. This phenomenon is called confinement. On the contrary when $r \rightarrow 0$ (i.e. large Q^2), the second term in Eq. 1.1 becomes less relevant, and the coupling constant becomes very small. In this condition, the hadron constituents can be considered free and weakly interacting. Such a behaviour is referred as asymptotic freedom. In the latter region where $\alpha_s \ll 1$, it is possible to perform perturbative calculations.

Perturbative calculations are possible only for small values of the coupling constant. Therefore, lattice QCD is developed to perform QCD calculations in the non-perturbative regime. Lattice QCD is a numerical technique which is based on the approximation of continuous space-time by a finite lattice of points. Lattice QCD calculations predict that a phase transition from hadronic matter to a plasma state of deconfined quarks and gluons can occur at extremely high temperature and/or pressure of the strongly interacting system.

Figure 1.4 shows the phase diagram, temperature versus net baryon density, of QCD matter. The region, at low temperature and low density, contains normal nuclear matter. By increasing the baryon density and keeping the temperature low, equal to compressing nuclear matter, a phase transition is expected to take place when the density reaches about four times the ordinary nuclear matter density. This condition is expected to be present in the core of neutron stars. By increasing the temperature and keeping the density low, a hadronic gas state is created in which the quarks are under confinement conditions. At extremely high temperature and/or density with respect to hadronic gas, a new state of matter called Quark-Gluon Plasma (QGP) is expected to be formed. In this state, quarks and gluons are effectively deconfined. The QGP is a plasma of strongly interacting partons and it is assumed to have been the state of matter of our Universe a few microseconds after the Big Bang.

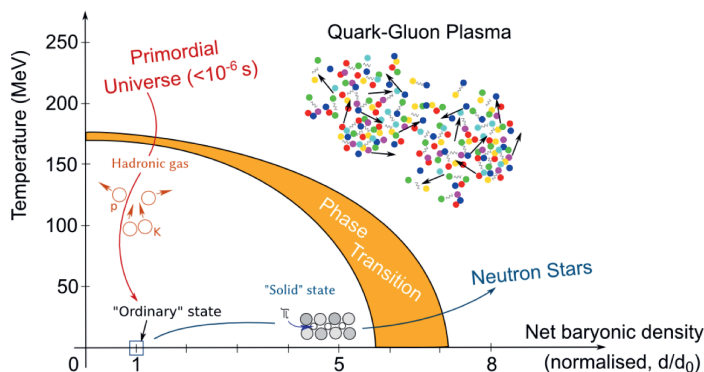


FIGURE 1.4: Phase diagram, temperature vs net baryon density, of QCD matter, ranging from regular nuclear matter to Quark-Gluon Plasma [6].

1.2 In-medium energy loss

1.2.1 General overview

The QGP state of matter can be created in high-energy heavy-ion collisions and investigated by means of probes. Typically those probes are themselves elementary particles, like quarks and gluons. During the propagation through the medium, the probes interact with its constituents and lose energy via elastic scatterings with the partons of the medium (collisional energy loss) [7, 8, 9] and gluon radiation [10, 11]. The first mechanism is similar to the ionization energy loss of charged particles which are moving through matter and are exposed to electromagnetic interaction with the electrons of atoms in the material. The second mechanism is similar to Bremsstrahlung for electromagnetic processes and also known as radiative energy loss.

In general, the energy loss ΔE depends on the properties of the particle traversing in a medium (i.e. energy E , mass m , and charge) as well as on the medium properties, such as temperature T , the interaction coupling constant α , and thickness L . We can express the energy loss ΔE as a function of energy E , mass m , temperature T , coupling constant α , and thickness L as: $\Delta E(E, m, T, \alpha, L)$. There are several variables that are useful to characterise the interaction of a particle inside a medium:

- the mean free path λ is the average distance traveled by a moving particle between successive collisions. It is expressed as $\lambda = 1/\rho\sigma$, where ρ is the medium density and σ is the cross-section,
- the opacity N is the number of scatterings experienced by a particle traveling through a medium. It is expressed as $N = L/\lambda$, where L is the thickness of the medium,
- the Debye mass m_D is important for a phenomenological discussion of the QGP formation,

- the transport coefficient \hat{q} contains information about the properties of the plasma medium and is defined as $\hat{q} \equiv m_D^2/\lambda = m_D^2\rho\sigma$,
- the spatial diffusion constant ($2\pi TD_s$) characterises the dynamics of heavy non-relativistic particles traveling through the plasma.

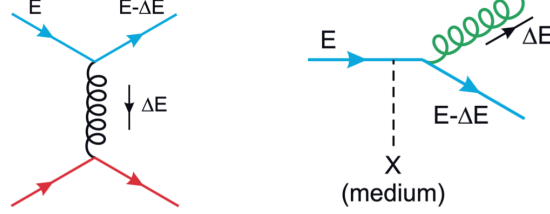


FIGURE 1.5: Energy loss diagrams for collisional (left) and radiative (right) mechanisms of a quarks of energy E traversing a quark-gluon medium [12].

The total energy loss experienced by a particle traveling through a medium is the sum of collisional and radiative mechanisms,

$$\Delta E = \Delta E_{\text{coll}} + \Delta E_{\text{rad}}. \quad (1.3)$$

Figure 1.5, on the left, shows the collisional energy loss through elastic scatterings with the medium constituents, while on the right it shows radiative energy loss (gluon radiation) through inelastic scatterings. In case of a high energy parton, the dominant energy loss mechanism is expected to be gluon radiation (radiative energy loss). It can be described by a theoretical model, i.e. the Baier-Dokshitzer-Mueller-Peigne-Schiff model [11]. According to this model, the average energy loss $\langle \Delta E \rangle$ is expressed by:

$$\langle \Delta E \rangle \propto \alpha_s C_R \hat{q} L^2, \quad (1.4)$$

where L is the distance traversed in the medium, α_s is the coupling constant of the parton-medium interaction, C_R is the colour factor (which is equal to 3 for gluons and equal to 4/3 for quarks) and \hat{q} is the transport coefficient given above. The mean energy loss depends on the gluon density (and therefore the energy density) of the medium. Moreover, the dead cone effect [13] predicts that the radiative energy loss decreases with increasing mass of the travelling parton, since the gluon emission is forbidden at angles smaller than

$$\theta_c = M_q/E_q, \quad (1.5)$$

where M_q and E_q are the mass and the energy of the quark respectively.

At the time this thesis work started, there was an important open debate on the theoretical formulation of the in-medium energy loss and, therefore, a strong need of precise experimental data. In particular, there were several ideas on how to implement in the QCD framework and interpret the proposed “dead-cone” effect and in general the mass dependence. In this manuscript, we will add information to this debate by experimentally using heavy-flavour quarks as a probe and then comparing our findings with model predictions.

The choice of heavy-quarks as QGP probe is motivated by several factors, due to their large masses, they witness the full evolution of the system and maintain their identities (thermal production is expected to be negligible [14]). In addition, the expected differences in the in-medium energy loss with respect to light quarks and gluons (mass dependence in the collisional and radiative energy loss), as well as their ability to be a clean self-generated probe make them ideal for testing the mechanism of in medium energy loss and the QGP diffusion coefficient.

1.2.2 Implementation of heavy-quark energy loss in models

Models implementing in-medium parton energy loss are categorized in two main groups: perturbative QCD (pQCD) based and transport based.

The pQCD models use perturbative QCD calculations to describe the in-medium energy loss and thus to describe the interaction between heavy quarks and the colored medium constituents. In the first step, the pQCD-based calculations describe the hard processes where heavy quarks are produced. The second step may vary for each model. As example, some models include the energy loss mechanisms in a medium that may or may not expand. Some models depend on the running coupling constant. Some of them are weakly coupled parton gas or strongly coupled fluid. The final step describes the hadronisation mechanisms of heavy quarks. The main pQCD based models in the field are Djordjevic [15], CUJET [16] and SCET [17] (Soft Collinear Effective Theory). The Djordjevic and CUJET models implement both energy loss processes, collisional and radiative, in order to describe the quark-medium interactions. As hadronisation mechanism, all the models consider hadronisation via fragmentation. In addition, all models also use a running coupling.

As aforementioned, the transport coefficient \hat{q} quantifies the strength of the interaction between the hard parton and the plasma medium and its energy density. Therefore, it is an important property of the QGP medium as probed by propagating energetic partons. Apart from the transport coefficient \hat{q} , other quantities which characterize the in-medium heavy quark interactions can be computed in thermal lattice QCD, i.e., the diffusion coefficient, and the heavy flavour susceptibilities. Even though those quantities are not directly considered experimental observables, they can be an important constraint for model calculations which provide a bridge to experimental

observables. Those features provide for a promising framework to determine the basic QCD force in the medium and the phenomena of heavy flavour transport in QCD matter.

The heavy-quark transport models start with the space-time evolution of heavy quarks in heavy-ion collisions. Different models can use different approaches, i.e. the TAMU [18] model use the Fokker-Plank equation which is implemented via Langevin dynamics [19], while the MC@sHQ+EPOS2 [20] and BAMPS [21] models use the Boltzmann equation to model the heavy quark evolution. Each model implements different mechanisms of heavy flavour transport through the QCD medium including perturbative and non-perturbative elastic (collisional) heavy quark interactions in the QGP, perturbative radiative energy loss of heavy quarks, heavy-meson scattering in the hadronic matter, transport through the quark-hadron transition and pre-equilibrium phases of heavy-ion collisions. The models such as BAMPS [21] and MC@sHQ+EPOS2 include both perturbative QCD collisional energy loss and radiative energy loss mechanisms. The heavy-quark transport models describe the hadronization mechanism via fragmentation and recombination, such as TAMU [18], MC@sHQ+EPOS2 [20], LBT [22], and PHSD [23] models.

1.3 Signatures of Quark-Gluon Plasma

The Quark-Gluon Plasma (QGP) cannot be observed directly since it has a very short lifetime of about $10^{-12} - 10^{-15}$ s [24] and then hadronises before reaching the detector. Therefore, as discussed in the previous sections, the investigation of the QGP proceeds by means of probes. The general idea is that quarks interact with the hot and dense medium losing energy in the process and/or acquiring collective features. Afterward, once the temperature goes below a certain threshold, they dress to form hadrons. By investigating the properties of those hadrons, it is possible to infer information on QGP properties and evolution.

Among the many possible observables, in this thesis we will discuss mainly the nuclear modification factor (R_{AA}) and, to a lesser extent (for model discussion purposes), the elliptic flow (v_2).

1.3.1 Nuclear modification factor

In the early stage of heavy-ion collisions, heavy quarks (i.e. charm and beauty) are scattered in the hot and dense medium. They are produced early in hard parton scattering processes before the QGP is formed. Their production time is about 0.1 fm/c for charm quarks and 0.02 fm/c for beauty [25], which is shorter than the one of the QGP of about 0.3–1.5 fm/c at Large Hadron Collider (LHC) energies [26]. Therefore, heavy quarks have the ability to traverse the medium and experience interactions with its constituents, forming an effective self-generated probe for medium tomography.

One way to investigate the QGP properties is to compare the yield of particle produced in nucleus-nucleus collisions to a reference evaluated in proton-proton (pp) collisions. Proton-proton collisions are usually considered a baseline because the energy density is expected to be not large enough to produce the plasma. In recent years the possibility of a creation of a QGP like matter even in high multiplicity pp collisions was proposed. However, there is a consensus that even in such a case, the system size would be small enough to not produce sizeable effects of in-medium parton energy loss, as already seen in p-Pb collisions [27, 28]. If a heavy-ion collision is assumed to be a superposition of multiple pp collisions without any nuclear effects, scaling the pp yield by the number of nucleon-nucleon collisions (N_{coll}) should give the same result as a heavy-ion collision.

As mentioned above, heavy quarks interact with the constituents of the medium and lose their energy via collisional and radiative energy loss. Afterward, they form into hadrons (as example, in about 90% of the cases, a charm quark forms into a D meson) that can be experimentally detected in order to obtain R_{AA} . The R_{AA} is defined as the transverse momentum (p_{T}) differential production yields of hadrons in nucleus-nucleus collisions ($dN_{\text{AA}}/dp_{\text{T}}$) divided by the cross section in proton-proton collisions ($d\sigma_{\text{pp}}/dp_{\text{T}}$) scaled by the average nuclear overlap function $\langle T_{\text{AA}} \rangle$:

$$R_{\text{AA}} = \frac{1}{\langle T_{\text{AA}} \rangle} \cdot \frac{dN_{\text{AA}}/dp_{\text{T}}}{d\sigma_{\text{pp}}/dp_{\text{T}}}, \quad (1.6)$$

where $\langle T_{\text{AA}} \rangle$ is the average number of nucleon-nucleon collisions $\langle N_{\text{coll}} \rangle$, which can be estimated via Glauber calculations [29, 30, 31, 32], divided by the inelastic nucleon-nucleon cross section σ_{inel} . If there is no medium modification and no effects related to nuclear parton distribution functions (PDF), the R_{AA} is expected to be unity, while the presence of the medium effects will lower the R_{AA} values below unity at intermediate and high- p_{T} . The R_{AA} below unity also implies a suppression with respect to pp collisions and it is generally considered an indication of in-medium energy loss.

Effects related to nuclear PDF and in general cold-nuclear-matter effects can in principle mimic a QGP signature by producing an R_{AA} below unity. However, detailed studies [27, 28] proved that at LHC energies such effects are small, resulting in a negligible effect above $p_{\text{T}} \sim 1 \text{ GeV}/c$.

1.3.2 Azimuthal anisotropy

The second observable we will discuss in this thesis is collective flow of particle, which can give an indication of collective expansion in the medium, offering advanced insight into the properties of the QGP and in particular its transport properties.

The collective flow of the medium includes a common radial expansion component affecting the thermal spectra of outgoing particles and this is called radial flow. It also includes an anisotropic component, which influences the spatial orientation of particle momenta. This is called anisotropic flow or azimuthal anisotropy. The azimuthal distributions can be parametrized through a Fourier decomposition:

$$\frac{dN}{d\phi} = \frac{N_0}{2\pi} (1 + 2v_1 \cos(\phi - \Psi_{\text{RP}}) + 2v_2 \cos(2(\phi - \Psi_{\text{RP}})) + \dots), \quad (1.7)$$

where angle ϕ is the azimuthal angle about the beam in z -axis with respect to the reaction plane Ψ_{RP} , N_0 is the normalisation parameter and v_n is the flow parameter for each harmonic n .

The most important contribution to anisotropic flow is the elliptic flow v_2 , the 2nd harmonic. In figure 1.6 can be seen a sketch of semi-central collisions. The orange areas (almond-shaped) represent the collision region, and the blue areas represent the spectator (i.e. non-colliding) nucleons of each nucleus. The grey grid is the reaction plane and is defined by the beam direction z and the impact parameter. The v_2 can be used to quantize the inhomogeneous expansion rate of the medium and extract its transport properties. By measuring the v_2 , the thermalization of heavy quarks in the QGP at low transverse momentum and the path-length dependence of energy loss at high transverse momentum can be investigated.

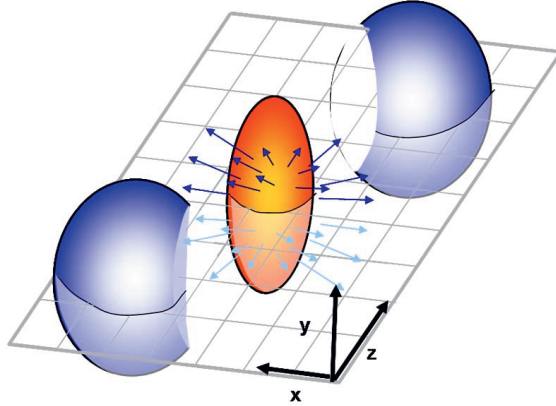


FIGURE 1.6: Sketch of a semi-central collision and pressure gradients arising from a geometrical anisotropy. The blue areas represent the spectator (i.e. non-colliding) nucleons of each nucleus, and the orange areas (almond-shaped) represent the collision region. The grey grid is the reaction plane, and is defined by the beam direction z and the impact parameter.

Chapter 2

The ALICE detector

There are seven experiments in total at the Large Hadron Collider (LHC). Each experiment has a different purpose and is characterised by its detectors. One of the four largest detectors at the LHC is A Large Ion Collider Experiment (ALICE). This experiment is run by a collaboration of scientists from institutes all over the world involving more than 1500 physicists, engineers and technicians, including around 350 graduate students, from 154 physics institutes in 37 countries. As mentioned, the ALICE detector is one of the four main experiments at the LHC together with CMS, ATLAS, and LHCb. These four detectors were built underground in huge caverns on the LHC ring, as shown in Fig. 2.1.

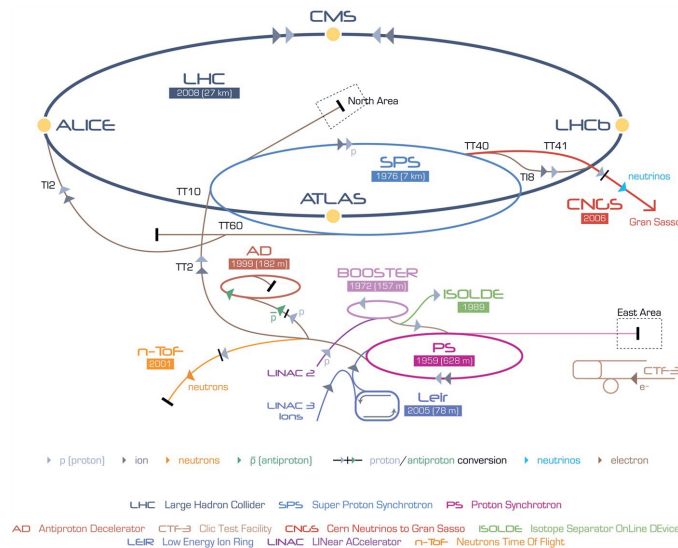


FIGURE 2.1: Large Hadron Collider. Figure is taken from [33].

ALICE is the only dedicated heavy-ion experiment at CERN which is built to exploit the physics of nucleus-nucleus collisions at the LHC energies. It is designed to study the physics of the strongly interacting matter at extremely high energy densities,

where a phase of matter with high energy density and temperature called Quark-Gluon Plasma is expected to be formed. Understanding of the underlying collision dynamics is required to evaluate the properties of the created matter. Besides running heavy-ion collisions in the energy regime accessible at the LHC, the ALICE detector also studies proton-proton and proton-nucleus collisions as a complement to separate the QCD-matter from the cold-matter initial- and final-state effects.

The ALICE apparatus, which has overall dimensions of $16 \times 16 \times 26 \text{ m}^3$, was designed to cope with the particle densities expected in central Pb–Pb collisions at the LHC. It has a high detector granularity, a low transverse momentum threshold $p_T^{\min} \approx 100 \text{ MeV}/c$, and good particle identification capabilities up to $20 \text{ GeV}/c$. The ALICE setup consists of two parts, the central-barrel detectors which are set inside the L3 solenoid magnet which has a magnetic field $B = 0.5 \text{ T}$ and the forward detectors, as shown in figure 2.2.

THE ALICE DETECTOR

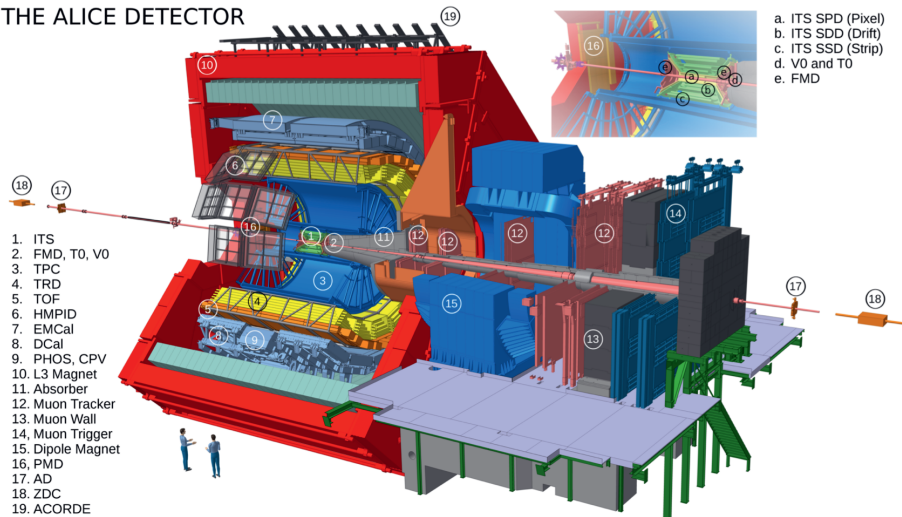


FIGURE 2.2: ALICE detector schematic for Run 2.

The central-barrel detectors consist of the Inner Tracking System (ITS), the Time Projection Chamber (TPC), the Transition Radiation Detector (TRD), the Time Of Flight (TOF), the Photon Spectrometer (PHOS), the Electromagnetic Calorimeter (EMCal), and the High Momentum Particle Identification Detector (HMPID).

The ITS is composed of six layers, two Silicon Pixel Detector (SPD), two Silicon Drift Detector (SDD), and two Silicon Strip Detector (SSD) and it is used for tracking and secondary vertexing. The TPC, the main ALICE tracking device with up to 160 space-points, is filled with Ne-CO₂ gas which has a 90 m^3 drift volume. The TPC

provides charged-particle identification via the specific ionization energy loss measurement dE/dx . The TRD detector provides charged-particle tracking and electron identification via transition radiation as well as dE/dx . The TOF, the HMPID, the PHOS, and the EMCal are electromagnetic calorimeters. They are used for photon and electron measurement and identification.

The ALICE forward detectors include the Photon Multiplicity Detector (PMD), the Forward Multiplicity Detector (FMD), the T0 and the V0 which are used for the event characterisation and triggering. The PMD and the FMD provide the measurement of photons and charged particles. The information of the time and longitudinal position of the interaction are delivered by the T0 detector. The V0, which consists of two scintillator arrays, measures charged particles at $-3.7 < \eta < -1.7$ and $2.8 < \eta < 5.1$, and is used for triggering and for the determination of centrality and the event plane angle in Pb–Pb collisions.

The forward muon arm consists of a hadron absorber, a dipole magnet, and five tracking stations with two pad chambers each (Muon Chambers). At about ± 112.5 m from the nominal interaction point there are the Zero Degree Calorimeters (ZDC) for further event characterisation and on top of the solenoid magnet there is a cosmic-ray trigger detector (ACORDE) to take data with cosmic ray triggers.

The main detectors that are used in the analysis of this thesis are the ITS, the TPC, the TOF, and the V0 detector will be discussed in the following sections.

2.1 Inner Tracking System

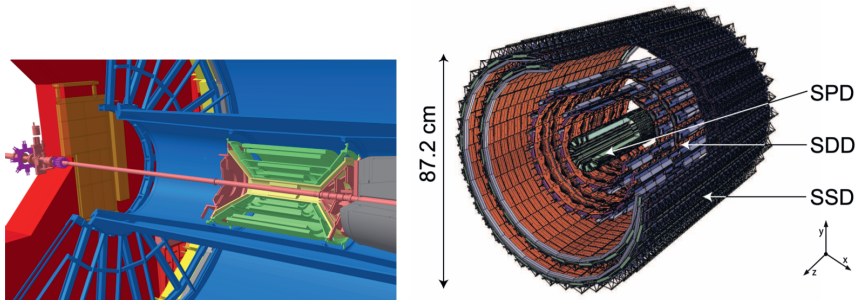


FIGURE 2.3: Layout of the Inner Tracking System detector [34]. Six layers of silicon detectors are composed of the two inner layers form the Silicon Pixel Detector (SPD), the two middle layers form the Silicon Drift Detector (SDD) and the two outer layers form the Silicon Strip Detector (SSD).

The Inner Tracking System (ITS), which is one of the central barrel detectors, consists of six concentric cylindrical layers of silicon which are located at radial distances r of about 4–43 cm from the beam direction (which is defined as the z -axis). The ITS was designed to provide an efficient track finding, primary and secondary vertex

reconstruction as well as particle identification (PID). It covers the pseudorapidity range $|\eta| < 0.9$ and the full azimuth. Figure 2.3 shows the layout of the six layers of the ITS.

The two innermost layers form the Silicon Pixel Detector (SPD). The SPD innermost layer covers the pseudorapidity range $|\eta| < 1.95$ for particles produced at $z_{\text{vtx}} = 0$. The two SPD layers have key importance in the secondary vertex determination. The two middle layers form the Silicon Drift Detector (SDD) and the two outermost layers form the Silicon Strip Detector (SSD). The four outer layers of the ITS are able to perform PID via the measurement of the ionization energy loss of particles dE/dx . This is useful for tracking low momenta charged particles (e.g. $p_T \sim 80$ MeV/ c for pions), where the ITS is used for standalone tracking. It means that ITS is able to operate independently of other detectors. Figure 2.4 shows an example distribution of the measured energy loss values dE/dx as a function of momentum in the ITS in Pb–Pb collisions at $\sqrt{s_{\text{NN}}} = 2.76$ TeV [35]. It shows that the separation between kaon and pion for $p_T \lesssim 0.7$ GeV/ c is about one standard deviation.

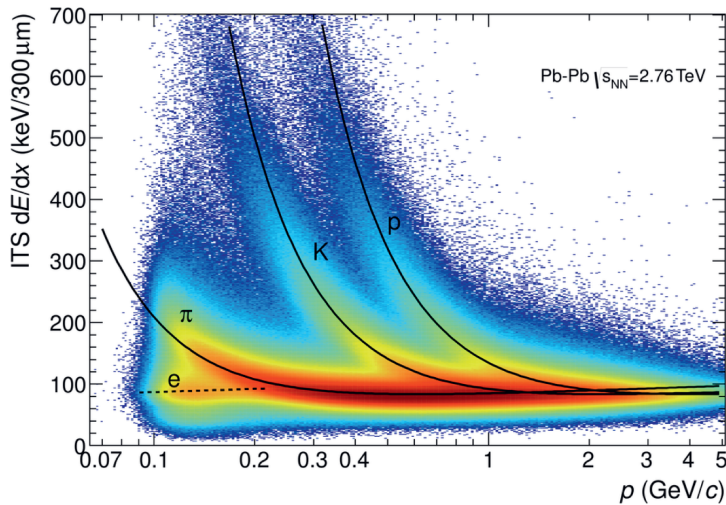


FIGURE 2.4: Distribution of the energy-loss dE/dx in the ITS as a function of momentum in Pb–Pb collisions at $\sqrt{s_{\text{NN}}} = 2.76$ TeV. Both energy loss and momentum were measured by the ITS alone [35].

2.2 Time Projection Chamber

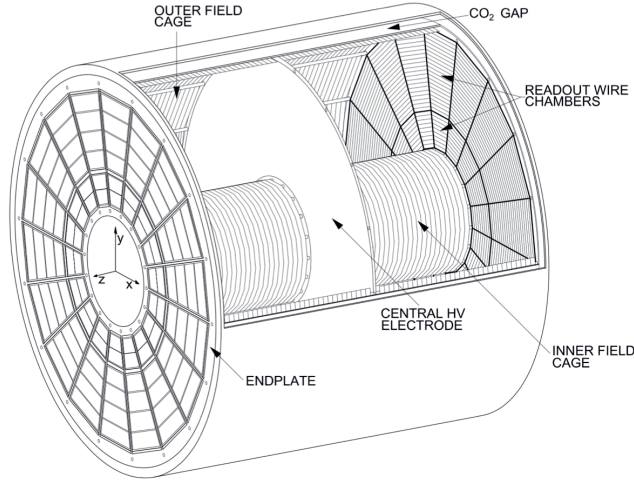


FIGURE 2.5: A sketch of the Time Projection Chamber (TPC). The volume is (filled with Ne-CO₂ gas) divided into two parts by the central cathode, creating two opposite electric fields [36].

The Time Projection Chamber (TPC) is a gas detector which is divided into two halves by a cathode, creating two opposite electric fields as shown in Fig. 2.5 [36]. It operates as the main ALICE tracking device. It is designed to be able to provide good tracking performance and particle identification (PID). The TPC has a cylindrical shape with inner radius of about 85 and outer radius of about 250 cm, as well as an overall length in the beam direction of 500 cm. It contains with 85.7% of Ne, 9.5% of CO₂ and 4.8% of N₂ gas mixture. The TPC inner radius was defined by the maximum acceptable hit density while the outer radius was defined by the minimum length required for a dE/dx resolution better than 10%. The TPC enables tracking performance with up to 160 three-dimensional space points with a position resolution in the $r\phi$ plane of 1100 to 800 μm and in the z -direction of 1250 to 1100 μm .

The TPC has an acceptance of $|\eta| < 0.9$. Charged particles in the TPC form an ionization trace that will move at constant velocity towards one of the two end-plates when traversing the gas volume. The ionization density depends on the velocity and mass of the particle. The readout chambers allow to amplify and register the signals of particle tracks once an ionization reaches the end-plates. The end-plates with 18 trapezoidal sectors are equipped with multi-wire proportional chambers covering an overall active area of 32.5 m².

The TPC PID performance covers a wide momentum range. It is done by simultaneously measuring the charge, the momentum as well as the specific energy loss dE/dx of the particles traveling through the detector. The specific energy loss dE/dx is

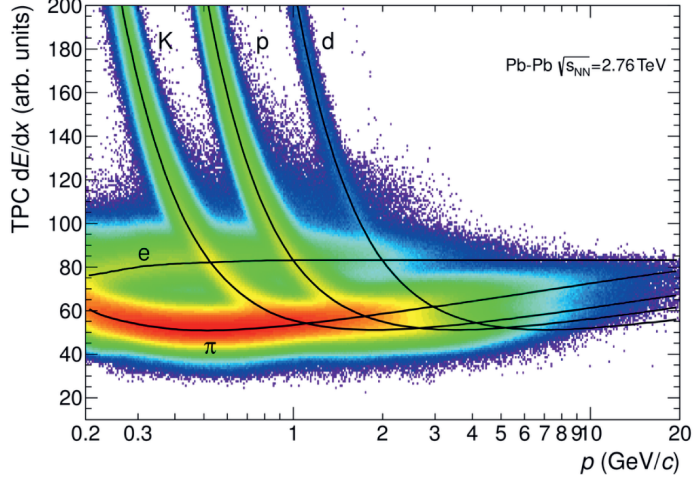


FIGURE 2.6: Distribution of the energy-loss signal in the TPC as a function of momentum in Pb–Pb collisions at $\sqrt{s_{\text{NN}}} = 2.76$ TeV. The lines show the parametrizations of the expected mean energy loss [35].

described by the Bethe-Bloch formula which is parametrized by a function originally proposed by the ALEPH Collaboration [37]

$$f(\beta_\gamma) = \frac{P_1}{\beta^{P_4}} \left(P_2 - \beta^{P_4} - \ln \left(P_3 + \frac{1}{(\beta_\gamma)^{P_5}} \right) \right), \quad (2.1)$$

where β is the velocity of the particle, γ is the Lorentz factor, and P_{1-5} are fit parameters. The measured dE/dx as a function of the track momentum in the TPC in Pb–Pb collisions at $\sqrt{s_{\text{NN}}} = 2.76$ TeV is shown in Fig. 2.6. The separation among the different particle species is observed clearly for $p_T \lesssim 1$ GeV/c, which allows a PID on a track-by-track basis. The separation is still feasible on a statistical basis at high p_T via multi-Gaussian fits. The PID resolution differs depending on the collision system, i.e. it is about 5.2% in pp collisions and 6.5% in the 5% most central Pb–Pb collisions.

2.3 Time-Of-Flight

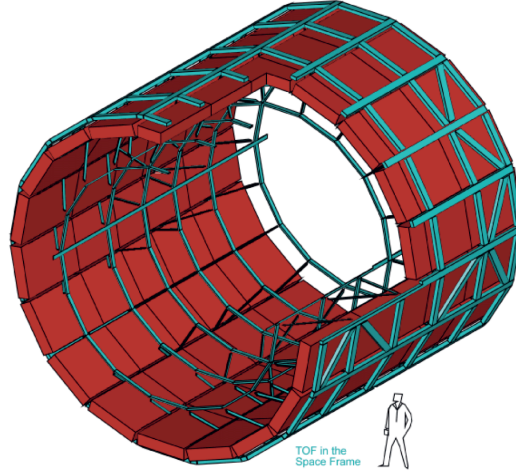


FIGURE 2.7: A view of the ALICE Time-Of-Flight detector.

The Time Of Flight detector (TOF) which is based on Multigap Resistive Plate Chamber (MRPC) technology, is used for particle identification at intermediate momenta. It has a cylindrical shape and is positioned at a radius of 370 to 399 cm from the beamline. The TOF covers the full azimuthal range and has the pseudorapidity range of $|\eta| < 0.9$. Figure 2.7 shows the TOF detector which has a modular structure with 18 sectors in φ . Each of those sectors is divided into 5 modules along the z direction (the beamline). This detector is fully dedicated to PID.

The TOF operates in conjunction with the T0 detector, which consists of two arrays of the Cherenkov counters, T0A and T0C, and which are located at the opposite sides of the interaction point at $-3.28 < \eta < -2.97$ and $4.61 < \eta < 4.92$. The TOF PID performance is based on the difference between the expected time-of-flight of the particle and its measured value, where the T0 detector is used for the start time determination. The expected value depends on the particle's mass hypothesis and is computed from the track length and the momentum of the particles. When there is no signal from the T0, the time-of-flight is obtained using the arrival times of the particle at the TOF. The TOF has a time resolution of 80 ps for pions with $p_T \approx 1$ GeV/ c in 0–70% Pb–Pb collisions, while for the T0 detector the resolution is 20–25 ps in Pb–Pb collisions. This value of the TOF already considers the detector resolution, the contribution from the electronics and calibration as well as the uncertainty on the start time of the event. The TOF which provides PID at the intermediate momenta allows the separation of pions and kaons at 3 standard deviation up to $p_T \approx 2.5$ GeV/ c and the separation of kaons and protons up to $p_T \approx 4$ GeV/ c . The distribution of the measured velocity β as a function of momentum by the TOF detector in Pb–Pb

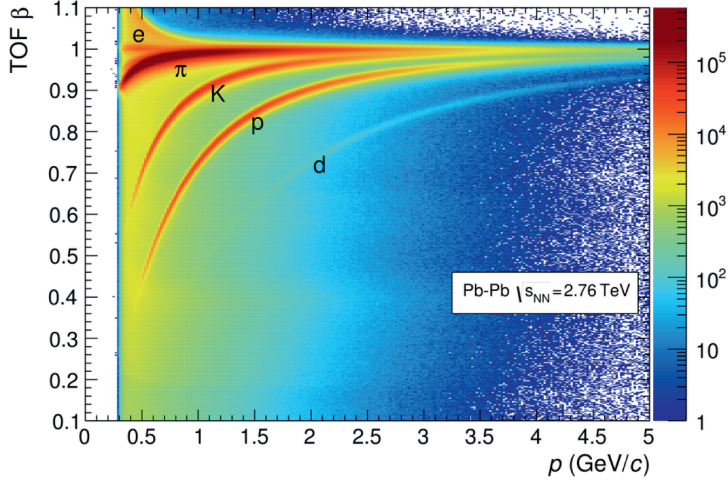


FIGURE 2.8: Distribution of β velocity measured by the TOF detector as a function of momentum for particles reaching the TOF in Pb-Pb interactions [35].

collisions at $\sqrt{s_{NN}} = 2.76$ TeV is shown in figure 2.8 [35].

2.4 V0

The V0 detector is mainly used for triggering and for the determination of centrality classes. The V0 detector is made of two arrays of scintillators, V0A and V0C, which are positioned on both sides of the interaction point. The V0A detector is located at 340 cm distance from the nominal interaction point position, along the beamline, on the side opposite to the muon spectrometer. The V0C is fixed to the front face of the hadronic absorber, and is located 90 cm from the nominal interaction point. They cover the pseudorapidity ranges $2.8 < \eta < 5.1$ for V0A and $-3.7 < \eta < -1.7$ for V0C and are segmented into 32 individual counters each distributed in four radial rings and 8 azimuthal sectors, as shown in figure 2.9. Besides triggering and centrality determination, the V0 detector is able to separate beam-beam interactions from background events such as beam-gas interactions, either on the trigger level or in off-line analysis.

During the V0 detector operation at the LHC, it can be affected by machine-induced background, which scales with the beam intensity. The sources of this background can be:

1. beam-gas interactions which are caused by nucleons in the beams which interact with residual gas in the beam pipe;
2. interactions between the beam halo and mechanical structures in the machine;

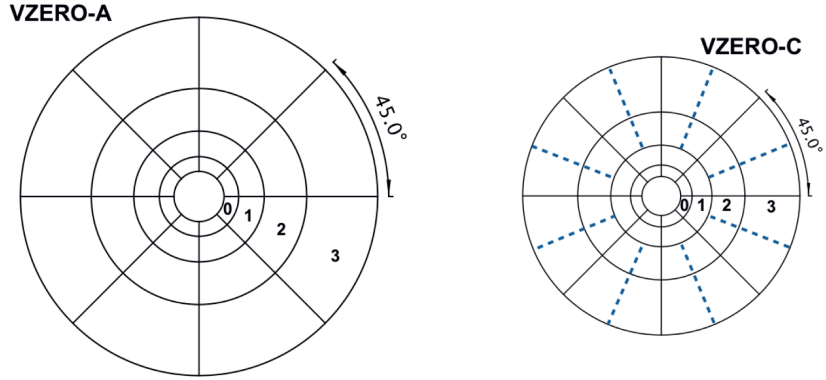


FIGURE 2.9: Sketches of V0A and V0C arrays showing their segmentation [38].

3. collisions of bunches in the main radio-frequency buckets with satellite bunches which are located at a short distance from the main bunches.

The background mentioned from sources 1. and 2. can be rejected by exploiting the arrival time of the signal in the two V0 detectors. The background that is caused by one of the LHC beams produces in fact an early signal on one of the two V0 detectors (it depends on the side from where the beam arrives) compared to the time of the collision at the nominal interaction point. The difference of the expected beam with the background signals is about 22.6 ns in the V0A and 6 ns in the V0C [35].

Chapter 3

Pb–Pb data samples at $\sqrt{s_{\text{NN}}} = 5.02 \text{ TeV}$

The Pb–Pb collision data samples at $\sqrt{s_{\text{NN}}} = 5.02 \text{ TeV}$ collected in 2015 and in the end of 2018 by the ALICE collaboration are used for this analysis. In the 2015 data-taking period, the Pb–Pb data sample was recorded with a minimum-bias trigger while for the 2018 data-taking period the events were recorded using specific centrality triggers, central and semi-central triggers, in addition to the minimum-bias interaction trigger configuration. The data samples that were used in the analysis are those provided by the Data Preparation Group after having rigorous quality assurance checks as will be partially discussed in the following section. The Monte Carlo (MC) samples used for the corrections are anchored to the data reported in the next section and generated with the same detector configuration as the data productions. The simulation used in this manuscript corresponds to central (0–10%) and semi-central (30–50%) collisions.

3.1 Triggering

In Pb–Pb collisions, event triggering was performed using the V0 detector which is configured to obtain high efficiency for hadronic interactions. The V0 detector consists of two scintillator arrays covering the full azimuth in the pseudorapidity η intervals $2.8 < \eta < 5.1$ for V0A and $-3.7 < \eta < -1.7$ for V0C [38]. It delivered three different triggers:

- the coincidence of V0A and V0C asking for at least one cell in each array (called minimum-bias trigger),
- a signal selecting the collisions corresponding to a centrality of 30–50% (called semi-central trigger),
- a signal selecting the 0–10% most central collisions (called central trigger).

As mentioned earlier, the 2015 data sample was recorded with a minimum-bias interaction trigger, while the 2018 sample was recorded with central and semi-central

trigger together with the minimum-bias configuration. In addition, the 2018 trigger consists of two stages, online and offline.

The online trigger is based on a coincidence of at least one beam-beam hit in V0A and V0C cells in each array out of 32 in total. In the online trigger, coincidence windows of 8 ns in length are placed around the beam-beam timing in order to select the beam-beam events and reject most of the beam-induced background events. The offline trigger consists of an average time measurement on V0A and V0C arrays, by calculating a weighted average time of flight over the channels. The weighted average time resolutions for V0A and V0C arrays are about 0.45 ns and 0.35 ns, respectively.

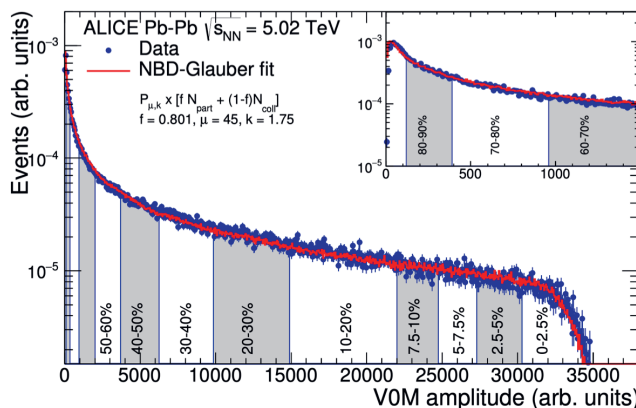


FIGURE 3.1: Distribution of the sum of amplitudes in the two V0 arrays (black histogram) in Pb–Pb collisions at $\sqrt{s_{\text{NN}}} = 5.02$ TeV [39]. The distribution is fitted with a Glauber model (red line) [29]. The shaded areas define the different centrality classes of hadronic collisions. The inset shows the low amplitude part of the distribution.

The collision geometry can be categorised with respect to its centrality. The centrality is defined as the percentile of the total hadronic Pb–Pb cross section and was determined from the sum of the signal amplitudes in the V0 scintillators. The distribution of the V0 summed amplitudes was fitted with a function based on the Glauber model [29, 30, 31, 32] combined with a two-component model for particle production [40], which decomposes particle production in nucleus-nucleus collisions into the contributions due to soft and hard interactions. Figure 3.1 represents a typical distribution of the sum of amplitudes in the two V0 arrays. The fit has been applied to a centrality range where the trigger reaches 100% efficiency for hadronic interactions and contributions from electromagnetic interactions were negligible. From the aforementioned fit, as shown in figure 3.1, the centrality of the collision can be determined and it represents an indirect evaluation of the impact parameter between the two nuclei.

3.2 Quality assurance

The data quality assurance (QA) is performed in order to guarantee the quality of the events recorded and, therefore, to ensure that the sample matches the minimal requirements for further physics analysis. Our data undergo several QA steps starting with the moment of the data-taking and then at the physics object reconstruction level to finish with the analysis level QA. This last check is done both to guarantee the quality of the collected data specifically for heavy-flavour analyses and to make sure that a sample that had been labeled for special purposes (as detector calibration) is not accidentally used for physics analysis. In this section, some of the performed quality assurance checks of the MC sample will be shown. These checks are similar for each D meson (D^0 , D^+ , D^{*+} and D_s^+) analysis since all mesons utilize a similar secondary vertex strategy and the same approach based on the reconstruction of the topology of the decay.

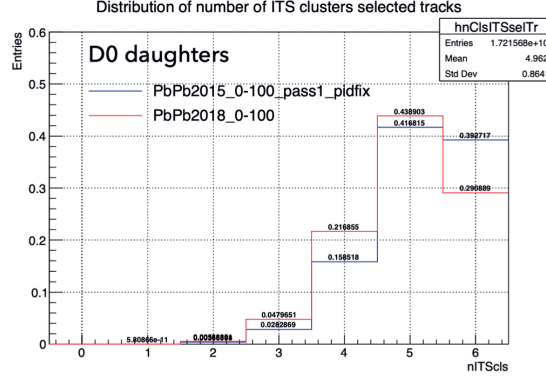


FIGURE 3.2: Comparison distributions of the number of ITS clusters of selected tracks in Pb-Pb data period 2015 and 2018 for D^0 daughters, normalized with respect to the total amount of selected tracks.

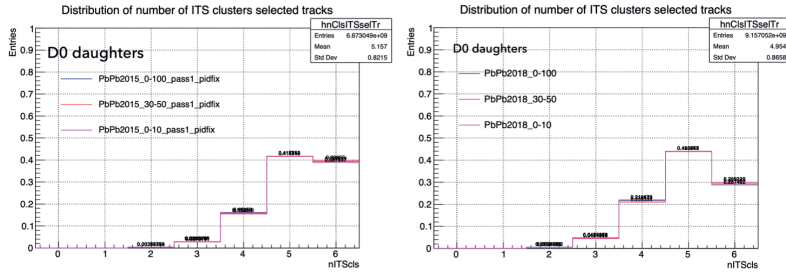


FIGURE 3.3: Distribution of the number of ITS clusters of selected tracks in Pb-Pb data period 2015 (left) and 2018 (right) for D^0 daughters, normalized with respect to the total amount of selected tracks.

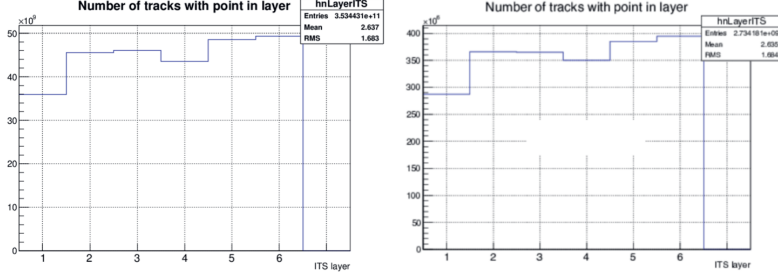


FIGURE 3.4: Amount of tracks with a point in a certain layer in data (left) and Monte Carlo simulations (right), normalized with respect to the total amount of tracks.

The distributions of hits in the Inner Tracking System (ITS) from the sample of heavy-flavour candidate tracks are shown in figures 3.2 and 3.3. In addition, the distribution of the tracks with a point in a specific layer is checked as shown in figure 3.4 in data and MC. The difference between 2015 and 2018 depicted in Fig. 3.2 originates from different detector conditions (detector aging and interventions on thresholds) while figures 3.3 and 3.4 are extremely useful, once compared with Monte Carlo simulations in order to investigate if the data suffer from in-bunch pileup. In the latter case, the occupancy of the layers in data would differ significantly from the one in simulation.

Figure 3.5, 3.6, 3.7, and 3.8 show examples of the particle identification (PID) quality assurance, for the specific energy loss in TPC and the time-of-flight in TOF. The average, is expected to be zero, is drawn in black, where the standard deviation, is drawn in red, is expected to be at unity. The scatter points represent the reduced χ^2/ndf in the TPC and TOF. Deviations from the expected values happen in regions with contamination, where other particle bands come close or even overlap each other.

All the data samples corresponding to data and MC simulations that were used in the analysis are reported in section 3.2.1 and 3.2.2.

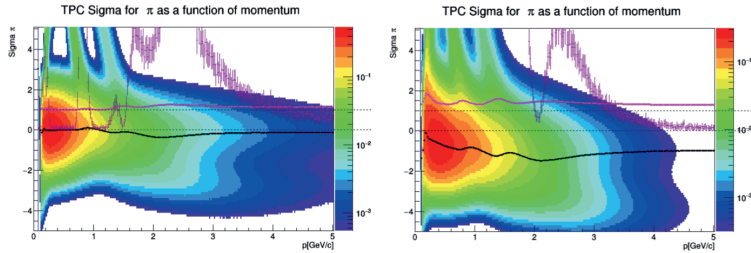


FIGURE 3.5: TPC PID estimator as a function of momentum for pions in data (left) and MC simulations (right) for Pb–Pb collisions 2018.

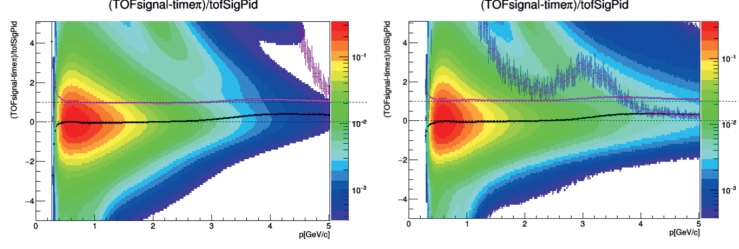


FIGURE 3.6: TOF PID estimator as a function of momentum for pions in data (left) and MC simulations (right) for Pb-Pb collisions 2018.

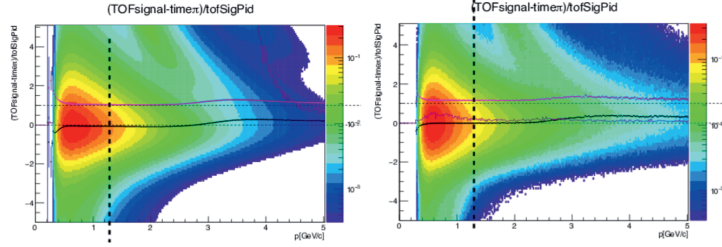


FIGURE 3.7: TOF PID estimator as a function of momentum for pions in data (left) and MC simulations (right) for Pb-Pb collisions 2015.

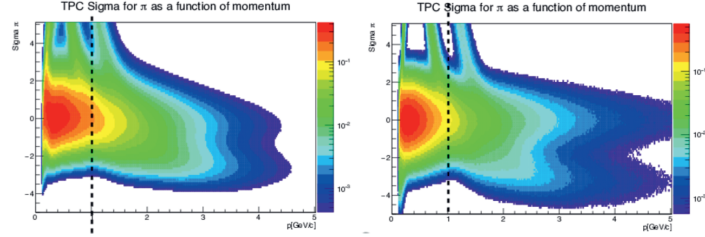


FIGURE 3.8: TPC PID estimator as a function of momentum for pions in data (left) and MC simulations (right) for Pb-Pb collisions 2015.

3.2.1 2015 data sample

In 2015, the ALICE Collaboration collected four weeks of Pb-Pb data into one period called in ALICE jargon LHC15o. The Pb-Pb collisions data sample has a total number of events of 167×10^6 and corresponds to an integrated luminosity of $13 \mu\text{b}^{-1}$. The collected data are subdivided in run number, as reported below.

246994, 246991, 246989, 246984, 246982, 246948, 246945, 246928, 246851, 246847, 246846, 246845, 246844, 246810, 246809, 246808, 246807, 246805, 246804, 246766, 246765, 246763, 246760, 246759, 246758, 246757, 246751, 246750, 246495, 246493, 246488, 246487, 246434, 246431, 246424, 246276, 246275, 246272, 246271, 246225, 246222, 246217, 246185, 246182, 246181, 246180, 246178, 246153, 246152, 246151, 246148, 246115, 246113, 246089, 246087, 246053, 246052, 246049, 246048, 246042, 246037, 246036, 246012, 246003, 246001, 245954, 245952, 245949, 245923, 245833,

245831, 245829, 245705, 245702, 245692, 245683, 245145, 245146, 245148, 245151, 245152, 245231, 245232, 245233, 245259, 245343, 245345, 245346, 245347, 245349, 245353, 245396, 245397, 245401, 245407, 245409, 245410, 245411, 245439, 245441, 245446, 245450, 245452, 245453, 245454, 245496, 245497, 245501, 245504, 245505, 245507, 245535, 245540, 245542, 245543, 245544, 245545, 245554, 244918, 244975, 244980, 244982, 244983, 245061, 245064, 245066, 245068, 246390, 246391, 246392

3.2.2 2018 data sample

During the 4 weeks of the 2018 Pb–Pb data campaign, the ALICE Collaboration collected the following statistic: 160×10^6 events (integrated luminosity of $130 \mu\text{b}^{-1}$) for 0–10% central Pb–Pb collisions and 133×10^6 events (integrated luminosity of $56 \mu\text{b}^{-1}$) for 30–50% semi-central Pb–Pb collisions. Such a high statistic data sample assures roughly 8 times more events in 0–10% centrality region and 5 times more in 30–50% with respect to what is available in the 2015 sample. The run numbers used in this manuscript are reported below.

296623, 296622, 296621, 296619, 296618, 296616, 296615, 296594, 296553, 296552, 296551, 296550, 296549, 296548, 296547, 296516, 296512, 296511, 296510, 296509, 296472, 296433, 296424, 296423, 296420, 296419, 296415, 296414, 296383, 296381, 296380, 296379, 296378, 296377, 296376, 296375, 296312, 296309, 296304, 296303, 296280, 296279, 296273, 296270, 296269, 296247, 296246, 296244, 296243, 296242, 296241, 296240, 296198, 296197, 296196, 296195, 296194, 296192, 296191, 296143, 296142, 296135, 296134, 296133, 296132, 296123, 296074, 296066, 296065, 296063, 296062, 296060, 296016, 295942, 295941, 295937, 295936, 295913, 295910, 295909, 295861, 295860, 295859, 295856, 295855, 295854, 295853, 295831, 295829, 295826, 295825, 295822, 295819, 295818, 295816, 295791, 295788, 295786, 295763, 295762, 295759, 295758, 295755, 295754, 295725, 295723, 295721, 295719, 295718, 295717, 295714, 295712, 295676, 295675, 295673, 295668, 295667, 295666, 295615, 295612, 295611, 295610, 295589, 295588, 295586, 295585, 297595, 297590, 297588, 297558, 297544, 297542, 297541, 297540, 297537, 297512, 297483, 297481, 297479, 297452, 297451, 297450, 297446, 297442, 297441, 297415, 297414, 297413, 297406, 297405, 297380, 297379, 297372, 297367, 297366, 297363, 297336, 297335, 297333, 297332, 297317, 297311, 297310, 297278, 297222, 297221, 297218, 297196, 297195, 297193, 297133, 297132, 297129, 297128, 297124, 297123, 297119, 297118, 297117, 297085, 297035, 297031, 296966, 296941, 296938, 296935, 296934, 296932, 296931, 296930, 296903, 296900, 296899, 296894, 296852, 296851, 296850, 296848, 296839, 296838, 296836, 296835, 296799, 296794, 296793, 296790, 296787, 296786, 296785, 296784, 296781, 296752, 296694, 296693, 296691, 296690

Chapter 4

D^{*+} analysis

4.1 D^{*+} reconstruction

The D^{*+} mesons and their antiparticles are reconstructed via their hadronic decay channel $D^{*+}(2010) \rightarrow D^0 \pi^+$ with branching ratio $(67.7 \pm 0.5)\%$, while the D^0 mesons decay into K^- and π^+ with branching ratio $(3.93 \pm 0.04)\%$ [3]. Being a strong decay, the D^{*+} decay vertex cannot be resolved from the primary vertex and, therefore, topological selections were applied on the secondary vertex of the daughter D^0 in order to reduce the combinatorial background. The reconstruction of the D^0 -meson will be discussed in detail in the next section.

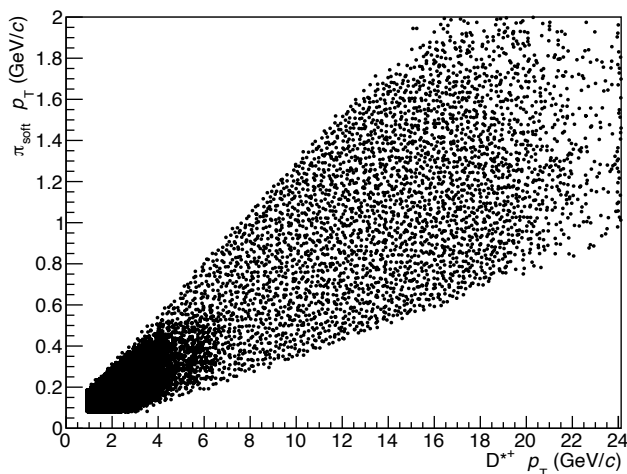


FIGURE 4.1: Correlation between transverse momentum of D^{*+} -meson versus transverse momentum of soft pion π_{soft} .

The D^{*+} candidates were formed by combining the D^0 candidates with pion tracks. The pions produced in the D^{*+} decays have a low momentum (see Fig. 4.1) and are called soft pions π_{soft} . The mass of the D^0 is about $1864.8 \text{ MeV}/c^2$ and the mass of the D^{*+} is about $2010 \text{ MeV}/c^2$. Since the mass of the D^0 is close to the mass of the

D^{*+} and the pion is very soft, it is more advantageous calculating the invariant-mass difference $\Delta M = M_{K\pi\pi} - M_{K\pi}$ instead of $M_{D^{*+}}$. This strategy removes the resolution effects of the D^0 and, consequently, the signal is seen as a sharp peak around the mass of the π^+ , near the edge of the combinatorial background phase space. Indeed, the invariant-mass difference $\Delta M = M_{K\pi\pi} - M_{K\pi}$ shows a peak at about $145.4 \text{ MeV}/c^2$, which is slightly higher than the π^+ mass ($\pi^+ = 139.5 \text{ MeV}/c^2$). The p_T -integrated invariant-mass difference ΔM is shown in Fig. 4.2 in the centrality classes 0–10% and 30–50%.

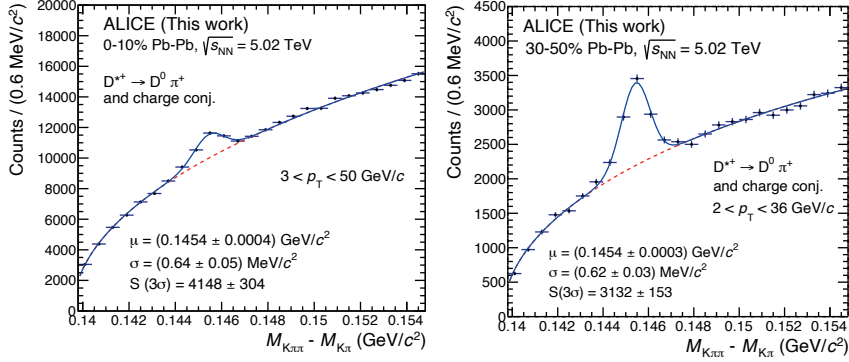


FIGURE 4.2: The p_T -integrated invariant-mass difference ΔM of the D^{*+} mesons candidate in the 0–10% and 30–50% centrality classes in Pb–Pb collisions at $\sqrt{s_{NN}} = 5.02 \text{ TeV}$.

4.2 D^0 reconstruction

D^0 mesons were reconstructed via the golden hadronic decay channel $D^0 \rightarrow K^- \pi^+$ with branching ratio of $(3.93 \pm 0.04)\%$ [3] and its charge conjugates. The D^0 candidates were formed by pairing the pion and kaon tracks with the correct charge-sign combination. The D^0 mesons have mean proper decay length $c\tau$ of about $123 \mu\text{m}$ and mean life time of about 10^{-15}s . Figure 4.3 shows a sketch of the D^0 decay topology which can be used to impose topological selections.

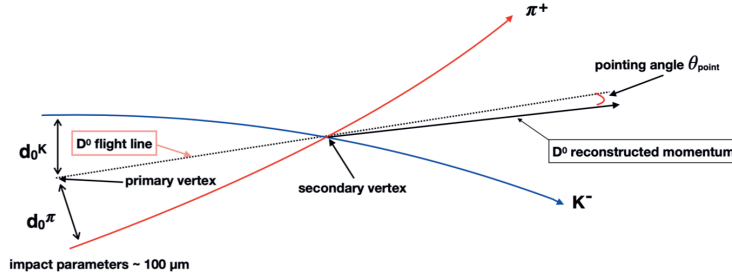


FIGURE 4.3: The D^0 -meson decay topology.

The primary vertex defines the position of the primary interaction inside the beam pipe of the collider and it contains the region where the charm quark is produced during the collision. Within detector resolution this is also assumed to be the position where the D^0 mesons were produced since the D^{*+} decay proceed via strong force and therefore it happens within few nm from the creation point. The primary vertex is essential for the event characterization and it can be used to determine various parameters of the decay. The decay point vertex of the D^0 -meson into a kaon and a pion is referred to as the secondary vertex, as can be seen in the sketch Fig 4.3.

4.3 Selection criteria

Several selection criteria are applied in order to maximize the signal while rejecting combinatorial background. The background rejection is carried out in steps by applying event selection, track selection, particle identification (PID) and topological selection. During the event selection step, only events that meet certain criteria are accepted for further analysis, such as trigger condition and centrality of the collision. The selection on the track properties is applied to the daughter particles that are used to reconstruct the D^{*+} candidates, while the PID is applied to the D^0 daughters by using the response of the TPC and the TOF detectors. The final steps are the topological selections which exploit the decay topology of the D^0 meson. For a more detailed discussion, see the next sections.

4.3.1 Event selection

The event selection begins at detector level with the trigger. The trigger is based on hits in the V0 or SPD detectors. In 2015 data taking, the minimum-bias trigger (MBand) was used in Pb–Pb collisions. It required coincident signals in both V0A and V0C scintillator arrays. In Pb–Pb collisions 2018 data taking, dedicated central and semi-central trigger were used. The central and semi-central trigger were based on the V0 detector. For central trigger, the signal amplitude thresholds were chosen in such a way that the trigger efficiency was 100% for events belonging to the 0–10% centrality percentile, dropping rapidly for higher centrality events, while for the semi-central trigger, the trigger efficiency was 100% for events belonging to the 30–50% centrality percentile.

The timing information of the V0 scintillator arrays was used together with the one from the ZDC detector for offline rejection of events produced by the interaction of the beams with residual gas in the vacuum pipe. Only events with a reconstructed interaction point (primary vertex) within $z = \pm 10$ cm from the centre of the ITS detector along the beam line were used in the analysis. For the data sample considered in this analysis, the probability of in-bunch collision pileup (i.e. collisions with two or more simultaneous interactions per bunch crossing) was negligible. In particular at peak luminosity, the probability of in-bunch collision pileup is less than one per mill. Finally, events without primary vertex and/or magnetic field information were rejected.

4.3.2 Track selection

In order to reduce the combinatorial background of D^{*+} -meson candidates, selections criteria were applied to the daughter tracks. An important step was the request for the tracks to pass the so-called kITSrefit and TPCrefit conditions. The refit procedure was performed with the Kalman filter algorithm. D^{*+} candidates were formed by combining D^0 candidates with soft pion tracks having $|\eta| < 0.8$ and $p_T > 0.1$ GeV/ c . Moreover, all the tracks required a minimum number of 70 (out of 159) associated space points in the TPC and at least three (out of 6) associated hits in the ITS layers, with at least one hit in the SPD layers.

The aforementioned track selection with $|\eta| < 0.8$ limits the D-meson acceptance in rapidity. The acceptance varies depending on p_T , from $|y| < 0.6$ for $p_T = 1$ GeV/ c to $|y| < 0.8$ for $p_T > 5$ GeV/ c . Therefore, a p_T -dependent fiducial acceptance cut was applied to the D-meson rapidity. The fiducial acceptance value $y_{\text{fid}}(p_T)$ increases from 0.6 to 0.8 in the transverse momentum range 1–5 GeV/ c . For $p_T > 5$ GeV/ c , it has a constant value of 0.8.

For the soft pion, the only selection applied was the ITSrefit condition. It required a minimum of three associated hits in the ITS layers, of which at least one associated

hit in either of the two pixel layers. Low momentum soft pion tracks are reconstructed using the ITS standalone method.

4.3.3 Particle identification

Further background rejection was achieved by applying particle identification (PID) to the D^0 meson candidate decay daughters. The detectors used at this step are the TPC in the low momentum region, that assures PID via specific energy loss dE/dx , and the TOF detector that assures PID information up to higher p_T via the measurement of the time-of-flight. In order to assign the kaon or pion mass to the decay tracks, selections are applied to the difference in the measured and expected signals. The selections were based on the width σ distributions of dE/dx in the TPC and time-of-flight in the TOF. When tracks were without TOF signal, the TPC only was used for particle identification. Tracks with contradicting PID were considered to be non-identified and maintained for further analysis. Figure 4.4 shows the TPC dE/dx distribution as a function of momentum (left panel) and time-of-flight β as a function of momentum (right panel) in Pb-Pb collisions at $\sqrt{s_{NN}} = 5.02$ TeV.

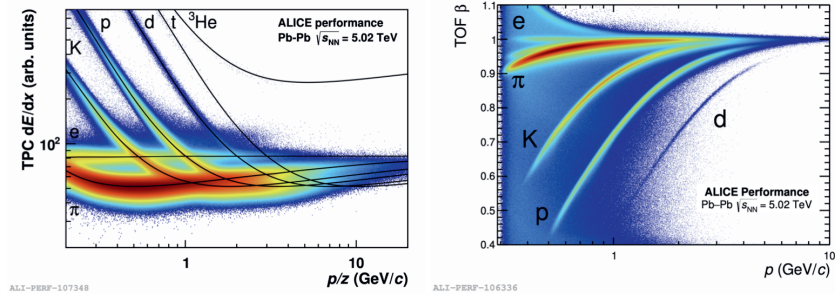


FIGURE 4.4: Left: TPC dE/dx as a function of momentum with superimposed Bethe-Bloch lines for various particle species. Right: TOF β versus momentum in Pb-Pb collisions at $\sqrt{s_{NN}} = 5.02$ TeV.

4.3.4 Topological selection

The D^0 -meson decay topology was exploited in order to further reduce the combinatorial background. The selections on the decay topology are p_T dependent. While a total of sixteen topological variables were used, the one reported below accounts for over 90% of the total background rejection power

- the impact parameter of kaon d_0^K and pion d_0^π : the impact parameters of the two daughter tracks measured in the transverse plane to the beam direction,
- cosine pointing angle or $\cos\theta_{\text{point}}$: the cosine of the angle between the reconstructed D^0 momentum and its flight line (see figure 4.3),

- normalised decay length: the projection of the decay length onto the transverse plane normalised by its resolution,
- $d_0^K \times d_0^\pi$: the product of impact parameters of a pion and a kaon,
- $\cos \theta^*$: the cosine of the angle between the kaon flight line in the D^0 rest frame and the boost direction,
- the distance of closest approach (DCA): the distance of closest approach between the two daughter tracks around the secondary vertex.

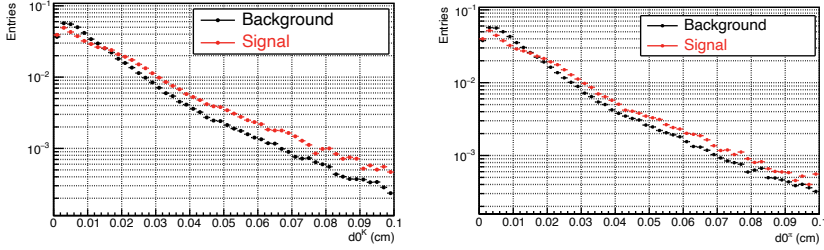


FIGURE 4.5: Impact parameter distribution of kaon (left) and pion (right) for signal and background for $2 < D_{pT}^0 < 2.5$ GeV/c.

The D^0 -meson within detector resolution is produced at the primary vertex, and then it flies about $100 \mu\text{m}$ before decaying at the secondary vertex into a pion and a kaon. The decay tracks can be prolonged back towards the primary interaction point. Their displacement from the interaction vertex is referred as the impact parameter d_0 . The impact parameter of kaons and pions are denoted by d_0^K and d_0^π , respectively. Figure 4.5 shows the impact parameter of kaons and pions for signal (in red) and background (in black). At a value of about 0.02 cm, data and background of kaons and pions start to show a different distribution. This difference gives us an idea to define a cut value to reduce the background and enhance the signal.

From figure 4.3, one can reconstruct the flight line of the D^0 from the primary and secondary vertex. Due to momentum conservation, the total D^0 momentum can be reconstructed by combining the p_T^K and p_T^π . Since the D^0 momentum reconstruction and the flight line are independent, these two vectors have a different orientation. The angle between the reconstructed momentum and the flight line of the D^0 connecting between the primary and secondary vertices is denoted as pointing angle or θ_{point} . If the candidate under scrutiny is a real D^0 meson, its reconstructed momentum should point to the flight line.

The distance between the two vertices, the primary and secondary vertex, is denoted as decay length. The decay length divided by its uncertainty is defined as the normalized decay length. The normalised decay length distribution is shown in Fig. 4.6 for signal and background. The signal distribution is higher than the background at a value above 5. The cut value for background rejection can be applied below this value.

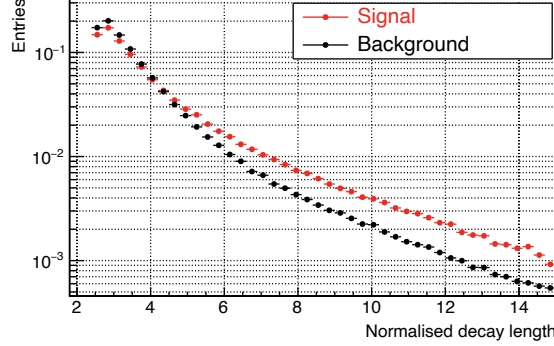


FIGURE 4.6: Normalised decay length distribution for signal and background at $2 < D_{pT}^0 < 2.5 \text{ GeV}/c$.

Another parameter that reduces the combinatorial background is the product of impact parameters of the pion and of the kaon, $d_0^K \times d_0^\pi$. This parameter is correlated with the D^0 decay length. The distance of the secondary and primary vertex is very small, and the secondary vertex resolution is limited. Therefore, it is more advantageous to work with the product of impact parameters. The product of impact parameters distribution for signal and background is shown in figure 4.7. The signal and background distribution can be distinguished at a value below $-0.25 \times 10^{-3} \text{ cm}^2$. This comparison gives us an indication of how to enhance the signal and reduce the background.

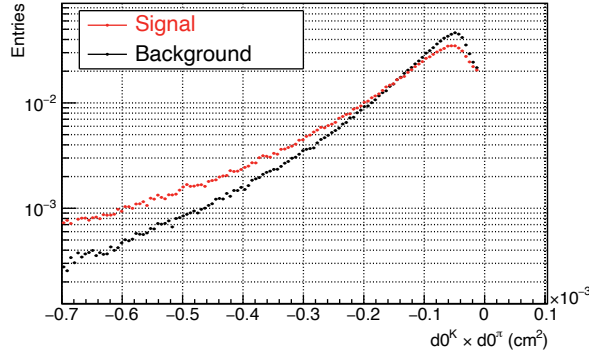


FIGURE 4.7: Product of impact parameter distribution $d_0^K \times d_0^\pi$ for signal and background at $2 < D_{pT}^0 < 2.5 \text{ GeV}/c$.

The decay angle parameter of a kaon and a pion is produced back-to-back in the rest frame of the D^0 decay. The cosine of the angle between kaon and the D^0 flight line in the D^0 rest frame is given by $\cos \theta^*$. The last parameter is the distance of the closest approach (DCA), which is defined as the shortest distance to which the D^0 candidate daughter tracks approach each other. Since D^0 daughter tracks are expected to come

from the same secondary vertex, their DCA is expected to be smaller than random combinations of background tracks.

4.4 D^{*+} yield extraction

4.4.1 Invariant mass analysis

The D^0 candidates are formed by pairing two oppositely charge particles, pion and kaon, passing the selection criteria discussed earlier in this manuscript. After the D^0 decay parameters are determined, the algorithm calculates the invariant mass distributions of the daughter particles:

$$M_{K\pi} = \sqrt{(E_K + E_\pi)^2 - (\vec{P}_K + \vec{P}_\pi)^2}. \quad (4.1)$$

Only candidate pairs within an invariant mass region of 3σ around the nominal mass peak of the D^0 are considered for further analysis. The width of the invariant-mass peak of the D^0 mesons, investigated in data and MC, is p_T dependent and ranges from 9 MeV/ c^2 at low p_T up to 40 MeV/ c^2 at high p_T .

After the D^0 candidates were successfully reconstructed, the algorithm loops over the new selection of positive charge pion to calculate the invariant mass of the D^{*+} candidates that consist of triplet charged particles,

$$M_{K\pi\pi} = \sqrt{(E_K + E_\pi + E_{\pi \text{ soft}})^2 - (\vec{P}_K + \vec{P}_\pi + \vec{P}_{\pi \text{ soft}})^2}. \quad (4.2)$$

4.4.2 Signal extraction

The D^{*+} -meson yield extraction is performed by separating the signal and background in the invariant mass spectra. A Gaussian fit function is used to describe the signal and an exponential term convoluted with a power law is used to account for the combinatorial background. The empirical background fit function is given by:

$$f(\Delta M) = a\sqrt{\Delta M - m_\pi} \cdot e^{b(\Delta M - m_\pi)}, \quad (4.3)$$

where m_π is the charged pion mass, a and b are free parameters.

4.5 Corrections

The transverse momentum dependent production of prompt D^{*+} mesons was calculated by correcting the measured inclusive raw yields according to the formula

$$\left. \frac{dN^{D^{*+}}}{dp_T} \right|_{|y| < 0.5} = \frac{f_{\text{prompt}}(p_T) \cdot \frac{1}{2} N^{D^{*+} \text{ raw}}(p_T) \Big|_{|y| < y_{\text{fid}}(p_T)}}{\Delta y(p_T) \cdot \Delta p_T \cdot (\text{Acc} \times \epsilon)_{\text{prompt}}(p_T) \cdot \text{BR} \cdot N_{\text{events}}}, \quad (4.4)$$

where the raw yield, $N^{D^{*+} \text{ raw}}$, was divided by a factor of two to take into account that we measure particle and antiparticle. The contribution of feed-down from beauty-hadron decays (D mesons that come from the decay of a beauty quark hadrons) was accounted for by multiplying the raw yields with the fraction of promptly produced D mesons, f_{prompt} . The D^{*+} raw yields also depend on the detector acceptance (Acc) and reconstruction efficiency ϵ of prompt D^{*+} -meson. Moreover, normalization factors to account for the branching ratio (BR) of the D^{*+} decay channel, the transverse momentum interval width Δp_T and the number of analysed events N_{events} are included.

The correction for acceptance and efficiency $(\text{Acc} \times \epsilon)_{\text{prompt}}$ includes the tracking efficiency, the acceptance of pions and kaons, and the kinematical and topological selection efficiency. The D^{*+} -meson yields were measured in a rapidity range varying from $|y| < 0.5$ at low p_T to $|y| < 0.8$ at high p_T . The rapidity acceptance correction factor $\Delta y = 2y_{\text{fid}}$ assumes a flat rapidity distribution for D^{*+} mesons in the measured rapidity y range. This assumption was verified to the 1% level with the PYTHIA v6.421 [41] pp simulations with the Perugia-2011 tune.

The acceptance-times-efficiency $(\text{Acc} \times \epsilon)$ were obtained using Monte Carlo simulations. The underlying Pb–Pb events at $\sqrt{s_{\text{NN}}} = 5.02$ TeV were produced with the HIJING v1.383 event generator [42]. Prompt and feed-down D^{*+} -meson signals were added using pp events from the PYTHIA v6.421 event generator [41] with the Perugia-2011 tune. All simulated pp events were required to contain a $c\bar{c}$ or $b\bar{b}$ pair, and D mesons were forced to decay in the hadronic decay channels of interest for the analysis. Only particles coming from the heavy quark hadronization and decays were injected in the HIJING event generator. The number of pp events added to each Pb–Pb event was adjusted according to the Pb–Pb collisions centrality class ranging from 60 in central 0–10% events to 5 in 50–60% events. The simulations used the GEANT3 transport package [43] together with a detailed description of the apparatus geometry and of the detector response. The simulation was configured to reproduce the conditions of the luminous region and of all the ALICE subsystems, in terms of active electronic channels, calibration level, and their time evolution within the Pb–Pb data taking period.

The fraction of prompt D^{*+} mesons coming from c quarks hadronization, f_{prompt} , was evaluated using the beauty-hadron production cross section from the FONLL

calculations [44]. It was folded with the $B \rightarrow D+X$ decay kinematics using the EvtGen package [45]. The computed cross section for the feed-down component of D^{*+} -meson was used, together with the Monte Carlo acceptance-times-efficiency $(\text{Acc} \times \varepsilon)_{\text{feed-down}}$ for D^{*+} mesons from B decays, to compute the expected feed-down contribution in the measured raw yields:

$$f_{\text{prompt}} = 1 - \frac{N_{\text{raw}}^{D^{*+} \text{ feed-down}}}{N_{\text{raw}}^{D^{*+}}} \quad (4.5)$$

with:

$$N_{\text{raw}}^{D^{*+} \text{ feed-down}} \Big|_{|y| < y_{\text{fid}}} = 2 \frac{d\sigma_{\text{FONLL}}^{D^{*+} \text{ feed-down}}}{dp_T} \Big|_{|y| < 0.5} \cdot \Delta y \cdot \Delta p_T \cdot (\text{Acc} \times \varepsilon)_{\text{feed-down}} \cdot \text{BR} \cdot L_{\text{int}} \quad (4.6)$$

where $N_{\text{raw}}^{D^{*+} \text{ feed-down}}$ is the estimated raw yield of D^{*+} mesons from beauty-hadron decays and L_{int} is the integrated luminosity.

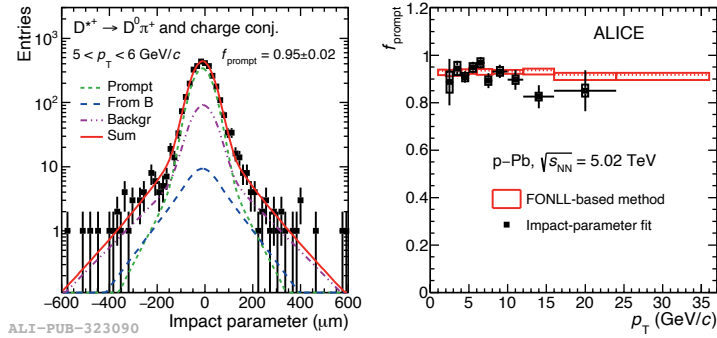


FIGURE 4.8: Left: Example of fits to D^{*+} impact-parameter distribution. The curves show the fit functions describing the prompt, feed-down and background contributions, as well as their sum. Right: fraction of prompt D^{*+} raw yield as a function of p_T [27] compared to the values obtained with FONLL-based approach.

The fraction of D mesons coming from c quarks that were estimated with the FONLL-based method [44], can also be estimated with the data-driven method that exploits the different shapes of the distributions of the transverse-plane impact parameter to the primary vertex of prompt and feed-down D mesons. The f_{prompt} fraction with this method was estimated via an unbinned likelihood fit of the impact parameter distribution of D^{*+} -meson candidates with a mass difference $\Delta M < 2.5\sigma$, where σ is the standard deviation of the Gaussian function of the invariant-mass signal. The fit

function which was used is discussed in ref [27]. The fraction of prompt D^{*+} with a data-driven method is shown in Fig. 4.8. These results, on one side, give us confidence our FONLL-based method match the result of the data-driven method and therefore it is solid and safe to use for the analysis and on the other side prove we cannot yet use the data-driven method in the analysis due to the limited p_T coverage and large uncertainties.

Chapter 5

D^{*+} analysis using Pb–Pb 2015 data sample

5.1 Introduction

The analysis described in this chapter will focus on the measurement of p_T -differential yields and the nuclear modification factor (R_{AA}) of prompt D^{*+} mesons (and their antiparticles) in Pb–Pb collisions at $\sqrt{s_{NN}} = 5.02$ TeV collected by ALICE in 2015. The measurement was performed in the 0–10% (central) and 30–50% (semi-central) centrality classes. Previous, low precision, measurements at $\sqrt{s_{NN}} = 2.76$ TeV indicate a strong suppression of non-strange D mesons (D⁰, D⁺, and D^{*+}) of a factor 5–6 for transverse momenta of about 10 GeV/ c in the 0–10% centrality class and of a factor 3 for transverse momenta of about 10 GeV/ c in the 30–50% centrality class [46, 47, 48, 49].

Single track and topological selection criteria were applied to maximize the significance of D^{*+} signal in the various transverse momentum bins. The single track selections criteria are summarized in Table 5.1. The topological and kinematic selections criteria used to select the D^{*+}-meson signals in the 0–10% and 30–50% centrality classes using 2015 Pb–Pb collisions are reported in Tables 5.2 and 5.3.

TABLE 5.1: Topological and kinematic selections applied for the D^{*+} analysis in the 0–10% centrality class.

Track selection	threshold value
D ⁰ daughter track	ITSrefit and TPCrefit
Soft pion track (π_s^+)	ITSrefit
Cluster in ITS	≥ 4 , for which ≥ 1 in SPD
Cluster in TPC	≥ 70 (out of 159)
TPC, TOF particle identification	$2\sigma, 3\sigma$ for 0–10% ; $3\sigma, 3\sigma$ for 30–50%

TABLE 5.2: Topological and kinematic selections applied for the D^{*+} analysis in the 0–10% centrality class.

p_T (GeV/c)/variable	[3,4]	[4,5]	[5,6]	[6,7]	[7,8]	[8,10]	[10,12]	[12,16]	[16,24]	[24,36]	[36,50]
ΔM_{D^0} (GeV)	0.024	0.03	0.03	0.034	0.036	0.055	0.055	0.074	0.074	0.094	0.09
DCA (cm)	0.022	0.021	0.02	0.02	0.02	0.02	0.02	0.02	0.02	0.02	0.02
$\cos(\theta^*)$	1.0	1.0	1.0	1.0	1.0	1.0	1.0	1.0	1.0	1.0	1.0
$p_T(\pi)$ (GeV/c)	0.9	0.9	0.9	0.9	0.9	0.9	0.9	0.7	0.5	0.5	0.5
$p_T(K)$ (GeV/c)	1.0	1.0	1.0	1.0	1.0	0.9	0.9	0.7	0.5	0.5	0.5
$d_{0,K}$ (cm)	0.1	0.1	0.1	0.12	0.12	0.12	0.15	0.15	0.15	0.2	0.2
$d_{0,\pi}$ (cm)	0.1	0.1	0.1	0.12	0.12	0.12	0.15	0.15	0.15	0.2	0.2
$d_{0,K} \times d_{0,\pi} (\times 10^{-3})$ (cm ²)	-4.5	< -3.5	-2.3	-1.0	-1.0	-7.5×10^{-2}	-7.5×10^{-2}	-7.5×10^{-2}	-5×10^{-2}	4.0	4.0
$\cos(\theta_{point})$	0.99	0.98	0.93	0.93	0.93	0.93	0.93	0.93	0.92	0.85	0.8
$\cos(\theta_{point})XY$	0.998	0.998	0.998	0.998	0.998	0.998	0.998	0.99	0.99	0.9	0.9
NDL _{XY}	8	6.5	6	6.5	6	5	5	3.7	2	0	0

TABLE 5.3: Topological and kinematic selections applied for the D^{*+} analysis in the 30–50% centrality class.

p_T (GeV/c)/variable	[2,3]	[3,4]	[4,5]	[5,6]	[6,7]	[7,8]	[8,10]	[10,12]	[12,16]	[16,24]	[24,36]
ΔM_{D^0} (GeV)	0.024	0.032	0.032	0.040	0.043	0.045	0.055	0.06	0.074	0.074	0.094
DCA (cm)	0.025	0.022	0.022	0.022	0.021	0.021	0.02	0.02	0.02	0.02	0.02
$\cos(\theta^*)$	0.8	0.8	0.8	1.0	1.0	1.0	1.0	1.0	1.0	1.0	1.0
$p_T(\pi)$ (GeV/c)	1.0	1.0	1.0	1.0	1.0	1.0	0.9	0.9	0.7	0.5	0.5
$p_T(K)$ (GeV/c)	1.0	1.0	1.0	1.0	1.0	1.0	0.9	0.9	0.7	0.5	0.5
$d_{0,K}$ (cm)	0.1	0.1	0.1	0.1	0.12	0.12	0.12	0.15	0.15	0.15	0.2
$d_{0,\pi}$ (cm)	0.1	0.1	0.1	0.1	0.12	0.12	0.12	0.15	0.15	0.15	0.2
$d_{0,K} \times d_{0,\pi} (\times 10^{-3})$ (cm ²)	-2.0	-3.0	-3.0	-2.3	-1.0	-1.0	-7.5×10^{-2}	-7.5×10^{-2}	-7.5×10^{-2}	-5×10^{-2}	4.0
$\cos(\theta_{point})$	0.93	0.93	0.93	0.93	0.93	0.93	0.93	0.93	0.93	0.92	0.85
$\cos(\theta_{point})XY$	0.998	0.998	0.998	0.998	0.998	0.998	0.998	0.998	0.99	0.99	0.9
NDL _{XY}	7	6.5	6.5	6.5	6.4	6.4	4.7	4.7	3.7	2	0

5.2 Raw yield extraction

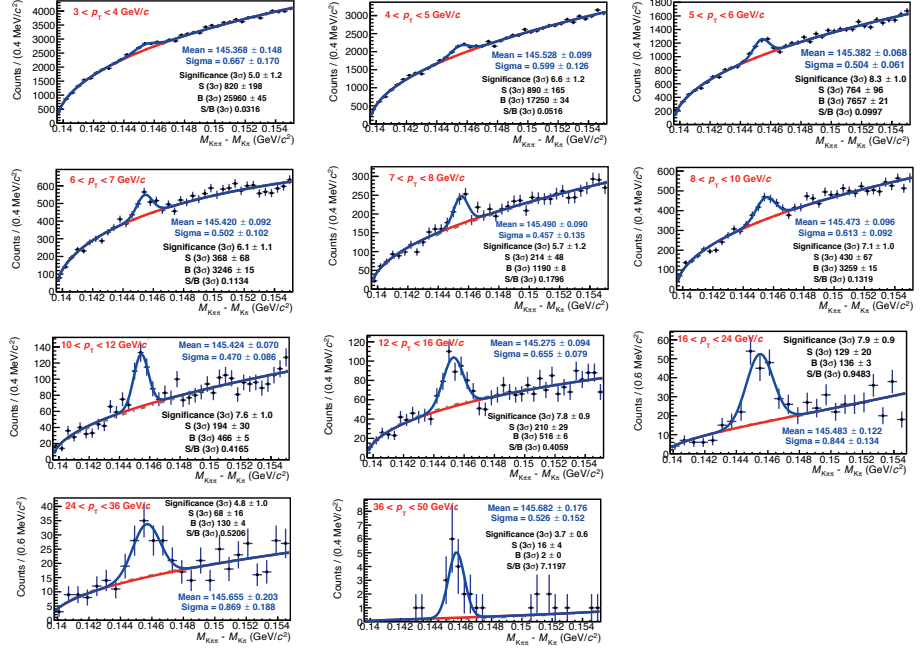


FIGURE 5.1: ΔM invariant-mass distributions of the D^{*+} candidates in the 0–10% centrality class in the transverse momentum range $3 < p_T < 50$ GeV/c. Fitted values for the mean and sigma are in GeV/c² unit.

The D^{*+} raw yields were extracted by performing a fit to the mass difference $\Delta M = M(K\pi\pi) - M(K\pi)$ distributions with a function composed of a Gaussian peak for the signal and an exponential term convoluted with a power law to account for the combinatorial background line shape:

$$f_{\text{bkg}} = a\sqrt{\Delta M - m_\pi} \cdot e^{b(\Delta M - m_\pi)} \quad (5.1)$$

where m_π is the pion mass (139.57 MeV/c²) and a and b are free parameters. Figure 5.1 and 5.2 show the invariant-mass distributions for the 0–10% centrality class in the transverse momentum range $3 < p_T < 50$ GeV/c and for the 30–50% centrality class in the transverse momentum range $2 < p_T < 36$ GeV/c. The goodness of the mass fit against the Monte Carlo (MC) expectation was checked for each p_T interval in terms of mass peak width (sigma) and mean. The comparison between data and MC is reported in figures 5.3 and 5.4 for central and semi-central collisions.

The results show a good agreement of data and Monte Carlo in all of the transverse momentum ranges under consideration. Some tension between data and MC was observed around 1 standard deviation, for example in the 0–10% centrality class, in the p_T range $12 < p_T < 16$ GeV/ c for the mass and above 16 GeV/ c for the width. As a consequence the aforementioned transverse momentum regions were examined with particular attention at the moment to assign a systematic from the yield extraction with the multi trial approach. The results are reported in the section 5.4, which gives us confidence that such fluctuations do not influence the final result.

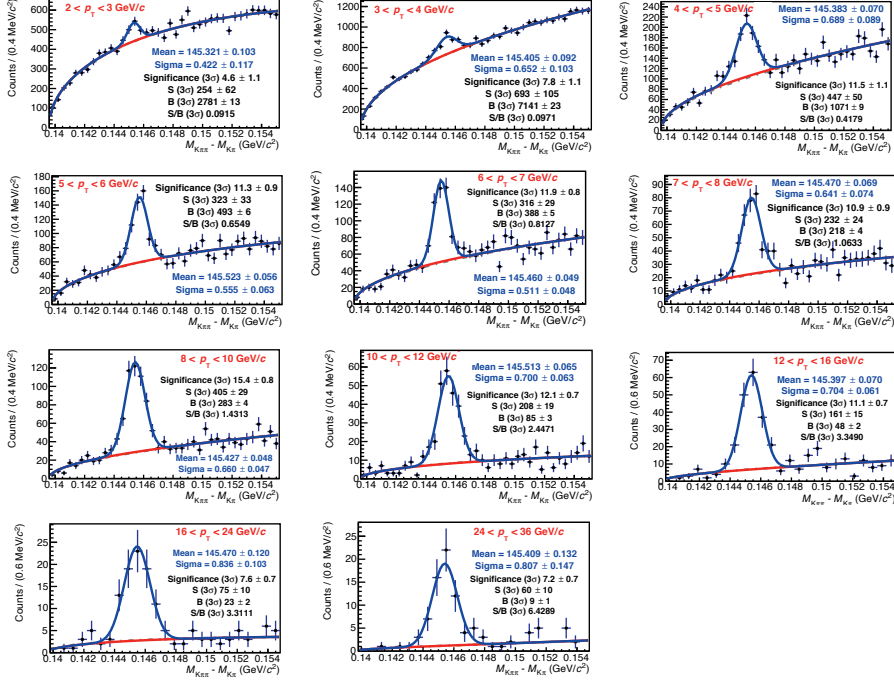


FIGURE 5.2: ΔM invariant-mass distributions of the D^{*+} candidates in the 30–50% centrality class in the transverse momentum range $2 < p_T < 36$ GeV/ c . Fitted values for the mean and sigma are in GeV/ c^2 unit.

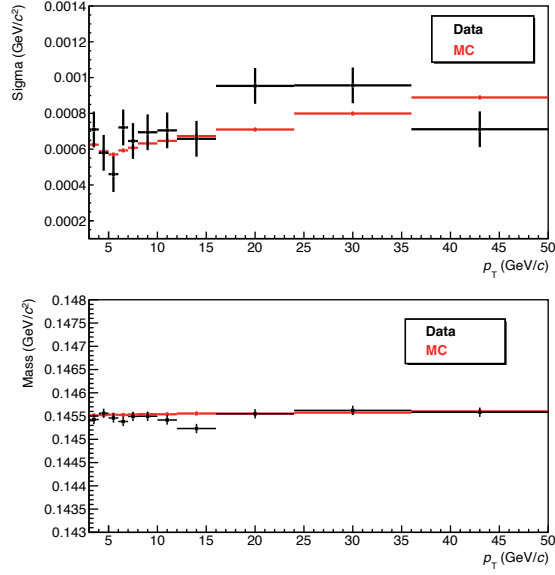


FIGURE 5.3: Comparison of Gaussian width (top) and mean (bottom) extracted from the invariant-mass fits of D^{*+} candidates in the 0–10% for data and MC simulation.

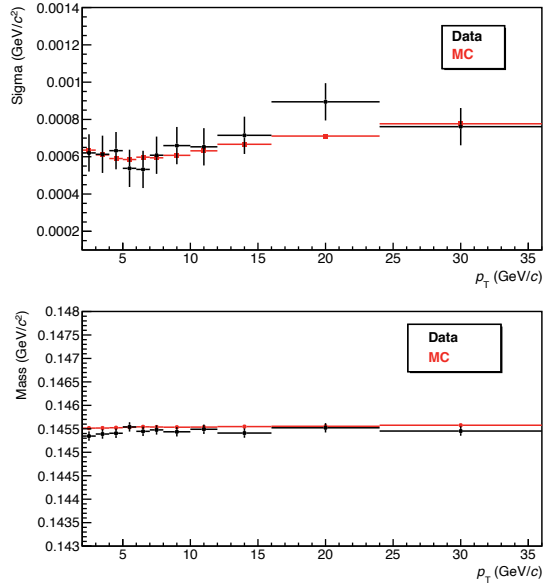


FIGURE 5.4: Comparison of Gaussian width (top) and mean (bottom) extracted from the invariant-mass fits of D^{*+} candidates in the 30–50% for data and MC simulation.

5.3 Efficiencies

The correction for acceptance and efficiency ($\text{Acc} \times \varepsilon$) was determined using Monte Carlo simulations with a detailed description of the detector geometry and its response, based on the GEANT3 transport package [43]. The HIJING v1.383 event generator [42] is used to simulate the underlying Pb–Pb events and D-meson signals were added using the PYTHIA v6.421 event generator [41] with Perugia-2011 tuning. The prompt yield of D mesons is obtained by subtracting from the inclusive yields the beauty-hadron decays estimated based on FONLL calculations [44, 50]. Figure 5.5 show the acceptance-times-efficiency correction ($\text{Acc} \times \varepsilon$) for prompt (red circles) and feed-down (blue squares) D^{*+} mesons with rapidity $|y| < y_{\text{fid}}(p_T)$ in the 0–10% and 30–50% centrality classes.

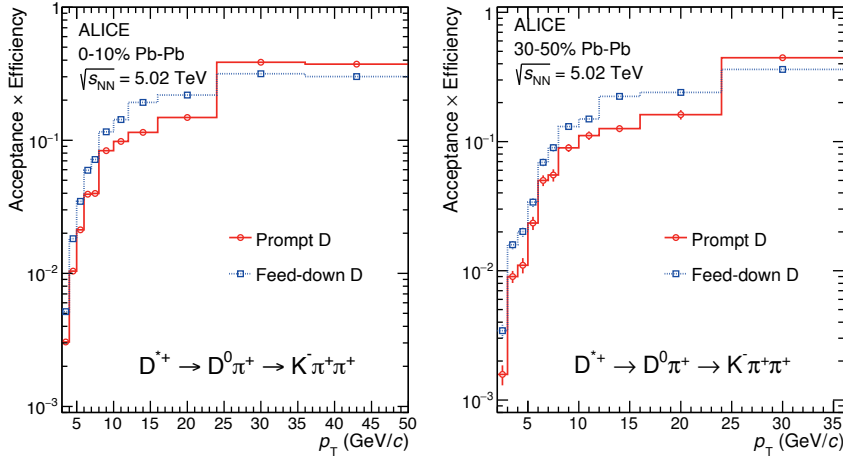


FIGURE 5.5: Production of acceptance and efficiency as a function of p_T for prompt (red circles) and feed-down (blue squares) D^{*+} mesons in Pb–Pb collisions for the 0–10% centrality class (left panel) and for the 30–50% centrality class (right panel) obtained from MC simulations [51].

Figure 5.6 shows the study of the efficiency in the 30–50% centrality class versus the various analysis steps due to:

- Monte Carlo acceptance (step 2): not all D^{*+} mesons produced in the collision end up in the detector, some of them fly away in the beamline direction. All candidates with a pseudorapidity of $|\eta| > 0.8$ are rejected.
- vertex reconstruction (step 3): the reconstruction of the primary and secondary vertices occurs in this step. A certain number of associated hits in the ITS and TPC is required for vertex reconstruction (see previous chapter).
- ITS refit (step 4): in this step, the track is refitted with the Kalman filter algorithm from the outwards toward the beamline (see chapter 4).

- reconstructed (step 5): after the primary and secondary vertex reconstruction and the refitting has been done, then the next step is the candidate reconstruction.
- reconstructed within acceptance (step 6): in this step, it is checked that the pseudorapidity η of the daughter tracks satisfy the acceptance requirements $|\eta| < 0.8$.
- required number of ITS cluster (step 7): the daughter tracks within detector acceptance have to have a certain number of associated hits in the ITS, at least three associated hits in the ITS layers with at least one hit in the SPD layers (see subsection 4.3.2).
- topological selection (step 8): selections on the topology of the D^0 candidates are applied.
- particle identification (step 9): after events pass the topological selection, particle identification is used to identify the D^0 daughter tracks (see subsection 4.3.3).

The plot shows a decreasing trend due to the selection of D^{*+} -meson candidates for each step obtained from Monte Carlo simulation.

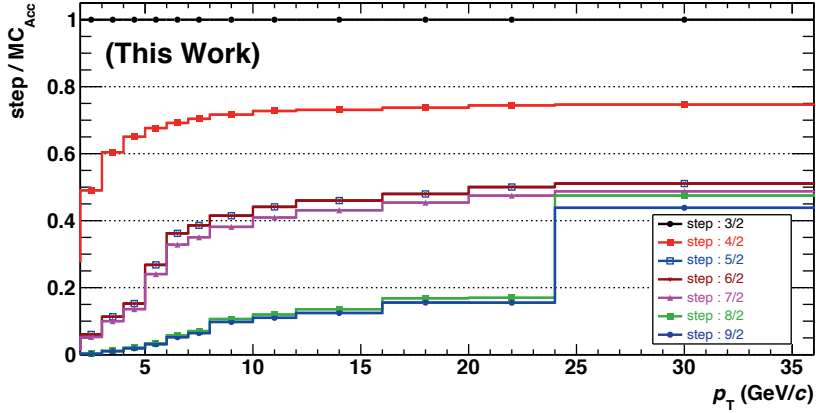


FIGURE 5.6: Efficiency study for each step in the 30–50% centrality class.

The reconstruction efficiency is evaluated with several steps that have described above, starting with D^{*+} mesons produced in a limited acceptance region, $|\eta| < 0.5$, until the D^{*+} mesons passing the particle identification and topological selections. Each step relates to passing a certain selection, and it is possible to calculate the efficiency for each step as shown in Fig. 5.6.

5.4 Systematic uncertainties

The systematic uncertainties of the D^{*+} -meson analysis were determined from the following sources:

- the raw yield extraction from the invariant-mass distribution,
- topological selection efficiency,
- particle identification efficiency,
- track reconstruction efficiency,
- generated Monte Carlo p_T shape of the D mesons,
- feed-down subtraction from beauty-hadron decays.

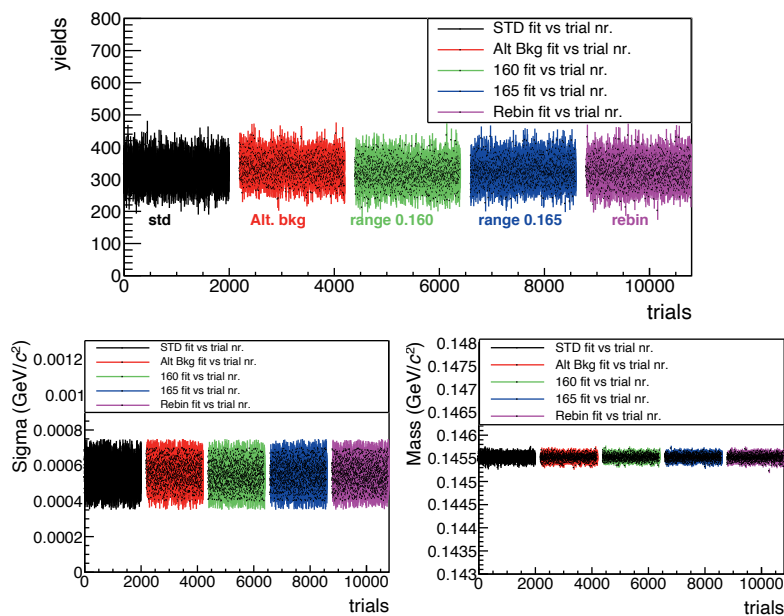


FIGURE 5.7: Top: Yield distributions versus trials for p_T 5–6 GeV/ c in the 30–50%. Bottom: Sigma and mass distribution versus trials at the same p_T interval and centrality class.

In addition, the uncertainties from the branching ratios [3] were also considered. The systematic uncertainties on the raw yield extraction were evaluated using a multi trial approach. Each bin of the invariant-mass distributions is smeared according to a Poissonian distribution based on the statistical error of the bin itself. The smearing procedure is repeated 10000 times each time fitting the resulting invariant mass distribution. Each 2000 times the following quantity is varied:

- background fit function (a power law $a(x - m_\pi)^b$ and exponential with power law),

- the fit range ($0.160 \text{ GeV}/c^2$ and $0.165 \text{ GeV}/c^2$ with respect to 5.1 and 5.2),
- the invariant-mass bin width,
- and the bin counting method instead of yield from fit method.

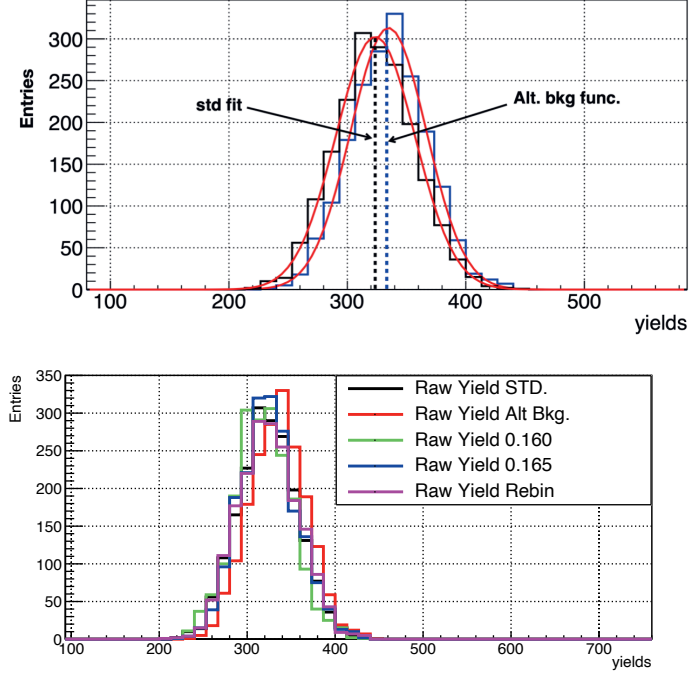


FIGURE 5.8: Top: Comparison of yield distributions with standard background fit function and alternative background fit function for p_T 5–6 GeV/c in the 30–50%. Bottom: Yield distributions for all variations in the same p_T interval.

In addition, all the fits were repeated with the sigma of the Gaussian function fixed to the values obtained from the Monte Carlo simulation and the mean of the Gaussian function to the particle data group value of the D^{*+} mass in order to check the possible effect of the statistical fluctuations one sees in Fig. 5.3 and 5.4. The fits which did not converge or had $\chi^2/ndf > 2.0$ were rejected and not considered in the evaluation of the systematic. The yield distributions from the multi trial are shown in Fig. 5.7, top panel, while the bottom panel of the same figure shows the sigma and the mass distributions for each variation. Figure 5.8, on top, shows the comparison between the distribution of the yield using the standard background fit function for D^{*+} and alternative background fit function after performed the multi trial. As clear from the plot, the yields with alternative background fit function are shifted with respect to the standard background function. Figure 5.8 (on the bottom) shows all yields distributions compared to the standard fit function. The systematic uncertainty was assigned by calculating the root mean square (RMS) of the yield ratios for all variations

with respect to the standard fit. The summary of the systematic uncertainty of the yield extraction is shown in Fig. 5.9.

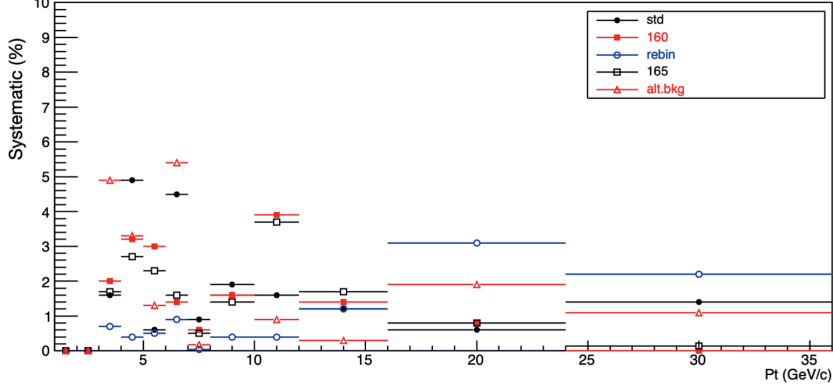


FIGURE 5.9: Systematic uncertainty summary of the raw yield extraction in the 30–50% centrality class.

The systematic uncertainty on the topological selection efficiency of the D^{*+} -meson represents a possible non-exact description of the D^{*+} -meson kinematic properties and of the detector resolution and alignment in simulation. This effect was evaluated by repeating the analysis by varying the selection criteria values, looser, and tighter ($\pm 5\%$, $\pm 10\%$, $\pm 15\%$, and $\pm 20\%$), with respect to the standard selection. These variations were significantly modifying the efficiencies, raw yields, and background values. The modification of the yields of 5% looser and tighter selection criteria with respect to the standard one, i.e. for p_T 12–16 GeV/c in the 30–50% centrality class, is shown in Fig. 5.10. The modification of the efficiency for looser and tighter ($\pm 5\%$ and $\pm 10\%$) selection values is shown in Fig. 5.11, on top, i.e. for 0–10% centrality class. At high p_T , the efficiency does not change so much because the selection values are already open to gain more signals where less background is expected. The systematic uncertainty was assigned by comparing the corrected yields of the standard selection criteria with respect to the one obtained with the different variations of the selection as shown in Fig. 5.11.

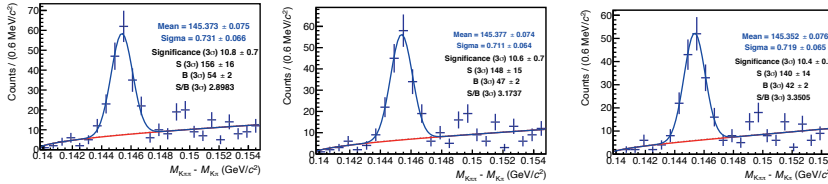


FIGURE 5.10: Difference selection criteria for p_T 12–16 GeV/c in the 30–50%. From left to right: loose, central and tigh selection applied.

An additional source of systematic uncertainty derives from the applied particle identification strategy. The systematic effect due to the PID selections was studied by

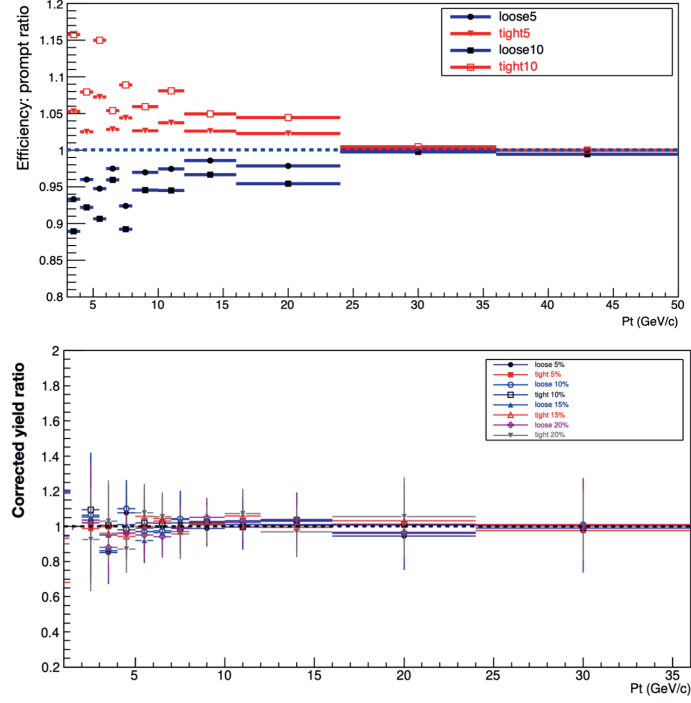


FIGURE 5.11: Top: Efficiency of prompt ratio in the 0–10% centrality class for looser and tighter ($\pm 5\%$ and $\pm 10\%$) selection values. Bottom: Corrected yield ratios for looser and tighter selection values with respect to the standard selection criteria values in the 30–50% centrality class.

repeating the analysis without PID selection. The uncertainty was evaluated by comparing the corrected yield ratio obtained with and without PID, which is shown in Fig. 5.12 for the 30–50% centrality class. All the points are compatible with unity, most of them at better than 1σ level. Therefore, no systematic uncertainty was assigned to PID efficiency.

The systematic uncertainty related to the tracking efficiency includes the effects arising from track propagation from the TPC to the ITS in data and Monte Carlo simulation, and track-quality selection criteria. The systematic uncertainty was estimated by varying the track-quality selection criteria and by comparing the probability to match the TPC tracks to the ITS hits in data and simulation. The comparison of the matching efficiency in data and simulations were made after weighing the relative abundances of primary and secondary particles in the simulations to match those observed in data, which were estimated via fits to the inclusive track impact parameter distributions. The matching efficiency in data and Monte Carlo simulation as a function of transverse momentum is shown in Fig. 5.13. Figure 5.14 shows the D^{*+} -meson daughter distributions versus D^{*+} -meson p_T on the left, and on the right shows the

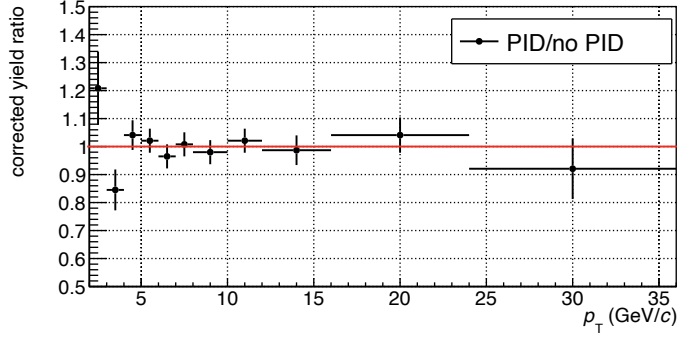


FIGURE 5.12: Particle identification systematic: comparison the corrected yield with and without PID in the 30–50% centrality class.

summary of the tracking efficiency systematic for D^{*+} mesons (3-prong) as a function of p_T .

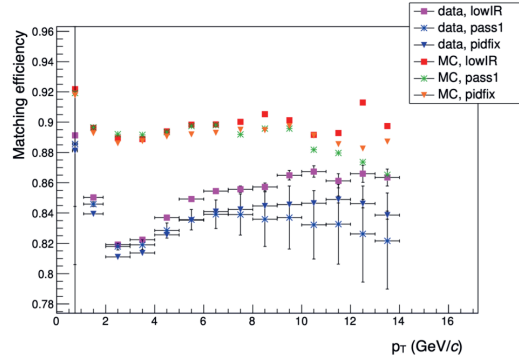


FIGURE 5.13: Matching efficiency, both in data and MC, for the three sample analysed as a function of p_T .

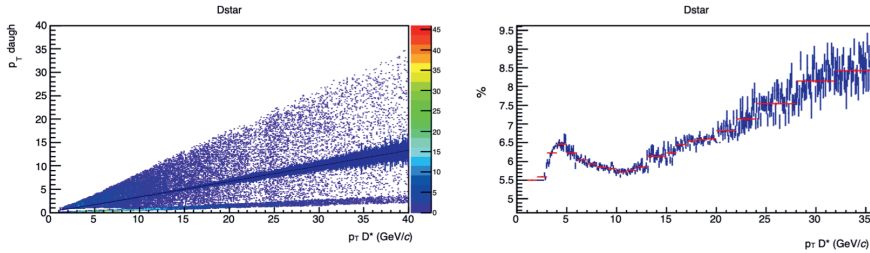


FIGURE 5.14: Scatter plot of daughter's p_T as a function of D^{*+} -meson p_T on the left and tracking systematic uncertainty for D^{*+} kinematic tracks in percentage as a function of p_T .

The systematic uncertainty due to a possible difference between the real and simulated D-meson transverse momentum distributions was investigated. The uncertainty

was estimated by weighting the assumed PYTHIA6 D^{*+} p_T distribution in simulation with alternative p_T shapes. In particular, the p_T distribution from FONLL calculations with and without hot-medium effects parameterized based on the R_{AA} from BAMPS [21], and LBT [22] models were used in central and semi-central collisions. The systematic uncertainty was assigned considering the variation of the efficiency obtained by applying the FONLL p_T distribution with respect to the result obtained by applying the FONLL and LBT p_T distribution in central collisions, which is shown in Fig. 5.15. The same procedure was done for semi-central collisions by comparing the FONLL p_T distribution and the FONLL and BAMPS p_T distribution to estimate the systematic uncertainty.

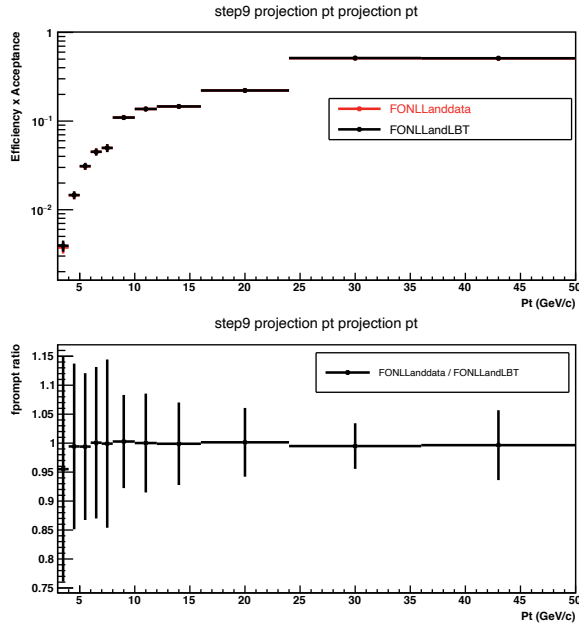


FIGURE 5.15: Relative change in efficiencies by using FONLL and FONLLandLBT weights in the 0–10% centrality class.

The systematic uncertainty on the subtraction of feed-down from beauty-hadron decays (i.e. the calculation of the f_{prompt} fraction) was estimated by varying:

- the p_T -differential feed-down D^{*+} -meson cross section from the FONLL calculations within the theoretical uncertainties,
- the ratio of the feed-down and prompt D^{*+} -meson R_{AA} hypothesis.

Figure 5.16 shows the prompt D^{*+} -meson fraction and the variation of R_{AA}^{prompt} as a function of the feed-down and prompt R_{AA} ratio hypothesis. The resulting uncertainty ranges between 4% and 12% depending on the centrality classes and p_T interval. The summary for all systematics is shown in Fig. 5.17. In addition, the systematic

uncertainties for the 0–10% and 30–50% centrality classes are reported in Table 5.4 and 5.5.

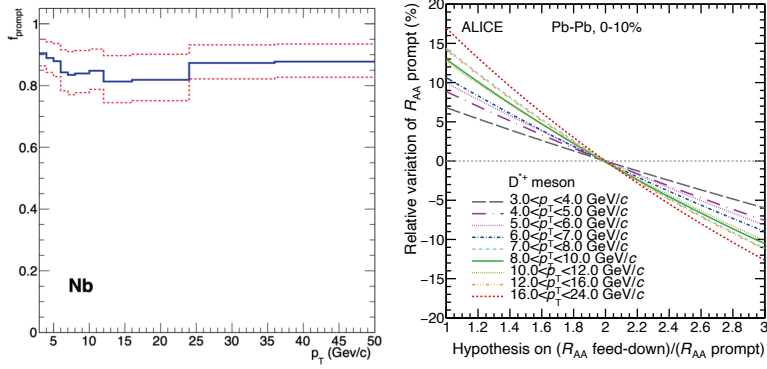


FIGURE 5.16: Fraction of prompt D^{*+} mesons on the left and systematic uncertainty from feed-down hypothesis as a function of p_T on the right in the 0–10% centrality class.

TABLE 5.4: Systematic uncertainties for the 0–10% centrality class.

p_T interval (GeV/c)	[3,4]	[4,5]	[5,6]	[6,7]	[7,8]	[8,10]	[10,12]	[12,16]	[16,24]	[24,36]	[36,50]
Yield extraction	11%	7%	7%	7%	7%	6%	6%	6%	5%	5%	5%
Tracking efficiency	10%	10%	10%	10%	10%	9%	8.5%	8%	7.5%	7.5%	7.5%
Particle identification efficiency	0	0	0	0	0	0	0	0	0	0	0
Cut efficiency	13%	13%	10%	10%	10%	10%	10%	10%	10%	10%	10%
MC p_T shape	4%	0	0	0	0	0	0	0	0	0	0
Feed-down subtraction	+6% -7%	+7% -9%	+7% -9%	+8% -10%	+11% -12%	+9% -11%	+8% -10%	+9% -11%	+10% -12%	+4% -5%	+4% -4%

TABLE 5.5: Systematic uncertainties for the 30–50% centrality class.

p_T interval (GeV/c)	[2,3]	[3,4]	[4,5]	[5,6]	[6,7]	[7,8]	[8,10]	[10,12]	[12,16]	[16,24]	[24,36]
Yield extraction	10%	6%	5%	5%	4%	4%	3%	3%	3%	3%	3%
Tracking efficiency	6%	6%	6%	6%	6%	6%	6%	6%	6%	7%	7%
Particle identification efficiency	0	0	0	0	0	0	0	0	0	0	0
Cut efficiency	10%	10%	5%	5%	5%	5%	5%	5%	5%	5%	0
MC p_T shape	5%	1%	0	0	0	0	0	0	0	0	0
Feed-down subtraction	+5% -6%	+6% -8%	+6% -8%	+6% -8%	+7% -10%	+9% -12%	+9% -12%	+8% -10%	+9% -11%	+10% -11%	+4% -4%

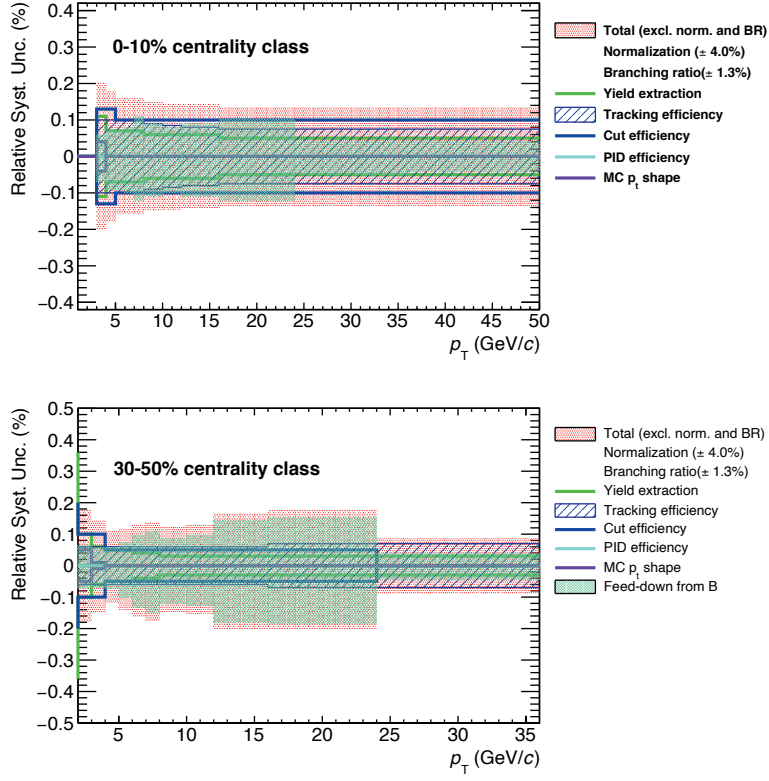


FIGURE 5.17: Summary of systematic uncertainties for the 0–10% and 30–50% centrality classes.

5.5 D^{*+} corrected transverse momentum distributions

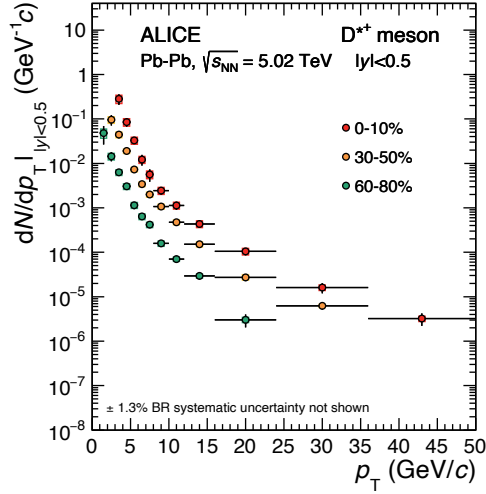


FIGURE 5.18: Transverse momentum distributions dN/dp_T of prompt D^{*+} meson as a function of p_T in the 0–10%, 30–50%, and 60–80% centrality classes in Pb–Pb collisions at $\sqrt{s_{NN}} = 5.02$ TeV [51].

The differential corrected p_T spectra of prompt D^{*+} mesons, dN/dp_T , as a function of the transverse momentum in Pb–Pb collisions at $\sqrt{s_{NN}} = 5.02$ TeV for the 0–10%, 30–50% and 60–80% centrality classes [51], are shown in Fig. 5.18. The vertical bars represent the statistical uncertainties and the empty boxes the systematic uncertainties. The uncertainty on the branching ratios is quoted separately.

Figure 5.19 shows the transverse momentum dependent ratios of meson yields, D^+/D^0 , D^{*+}/D^0 and D_s^+/D^0 in Pb–Pb collisions at $\sqrt{s_{NN}} = 5.02$ TeV, compared to the values measured in pp collisions at $\sqrt{s} = 7$ TeV [52]. They are found to be compatible in Pb–Pb and pp collisions within uncertainties, indicating no significant modification of their relative abundances as a function of p_T and in centrality classes at the LHC energies. The D_s^+/D^0 ratio in Pb–Pb collisions at $\sqrt{s_{NN}} = 5.02$ TeV is measured with a better precision by a factor about two with respect to one measured in 2.76 TeV [48]. The values of these ratios in Pb–Pb are larger than in pp collisions, in the 0–10%, 30–50% and 60–80% centrality classes, however the measurements in the two systems are compatible within about one standard deviation of the combined uncertainties.

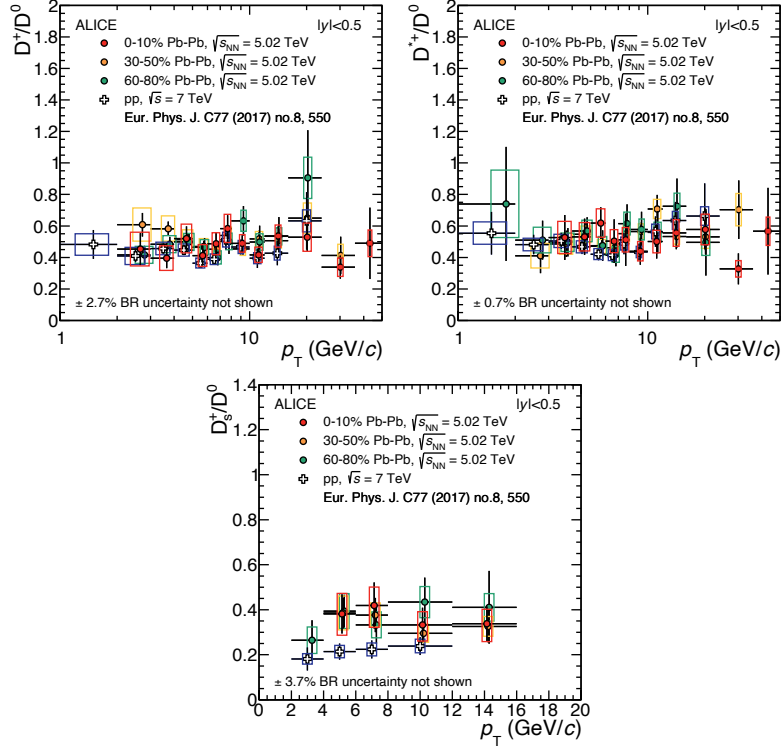


FIGURE 5.19: Ratio of D^+/D^0 , D^{*+}/D^0 and D_s^+/D^0 as a function of p_T in Pb-Pb collisions at $\sqrt{s_{NN}} = 5.02$ TeV and pp collisions at $\sqrt{s} = 7$ TeV [51].

5.6 Proton-proton reference

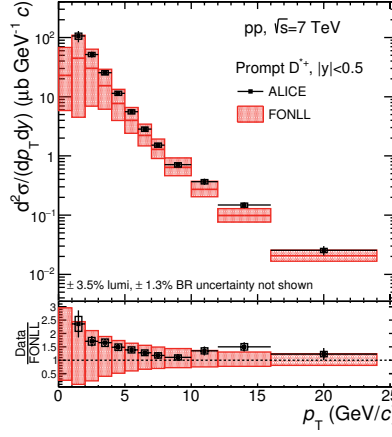


FIGURE 5.20: D^{*+} mesons p_T -differential cross section in pp collisions at $\sqrt{s} = 7$ TeV [52] compared to FONLL model calculations. In the data-to-theory ratios the 3.5% normalisation uncertainty due to the luminosity determination is not included in the systematic uncertainty on the data points.

To calculate the nuclear modification factor, the proton-proton cross sections were needed as reference. Figure 5.20 shows the prompt D^{*+} -meson cross sections measured in pp collisions at $\sqrt{s} = 7$ TeV compared with the FONLL calculations. The measured cross sections of prompt D^{*+} mesons are described well by the FONLL calculations within uncertainties. The data lie systematically on the upper edge of the uncertainty band of the theory prediction.

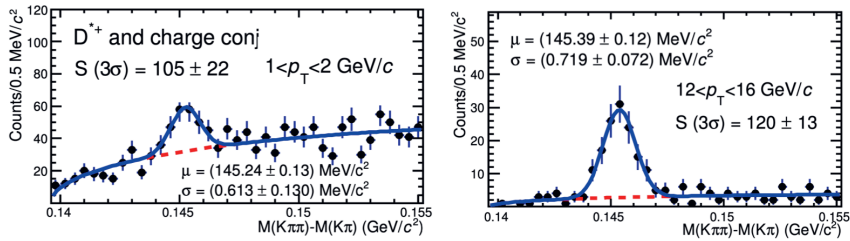


FIGURE 5.21: ΔM invariant-mass of the D^{*+} in pp collisions at $\sqrt{s} = 7$ TeV [52].

In the 2015 data analysis, the proton-proton reference at $\sqrt{s} = 5.02$ TeV was obtained by scaling the measurements of prompt D^{*+} mesons cross section at $\sqrt{s} = 7$ TeV [52] to $\sqrt{s} = 5.02$ TeV using the FONLL calculations [53]. The D^{*+} -meson cross section at $\sqrt{s} = 7$ TeV was used a reference due to the measurement precision in terms of larger statistic and smaller uncertainty with respect to pp collisions at $\sqrt{s} = 5.02$ TeV. Figure 5.21 shows ΔM of the D^{*+} candidates in pp collisions at $\sqrt{s} = 7$ TeV. The scaling

factor was evaluated from the ratio of the theoretical cross sections at these energies and the uncertainties were determined by the envelope of the scaling factors obtained by varying the calculation parameters (factorisation and renormalisation scales, and charm-quark mass). These scaling measurements reach up to $p_T = 24 \text{ GeV}/c$.

At high p_T where the measured pp cross sections are not available, the FONLL calculation at $\sqrt{s} = 5.02 \text{ TeV}$ [53] was used as a reference by scaling the values to match the central value of the scaled data at lower transverse momentum. The procedure consists in the evaluation of the ratio data-to-theory considering the measurement statistical uncertainties. The systematic uncertainty of the extrapolated cross section was assigned by varying the FONLL parameters and shifting up and down the data points of an amount equal to their systematic uncertainty. At this point the ratio is fitted with a constant and the next value extrapolated.

5.7 D^{*+} meson nuclear modification factor

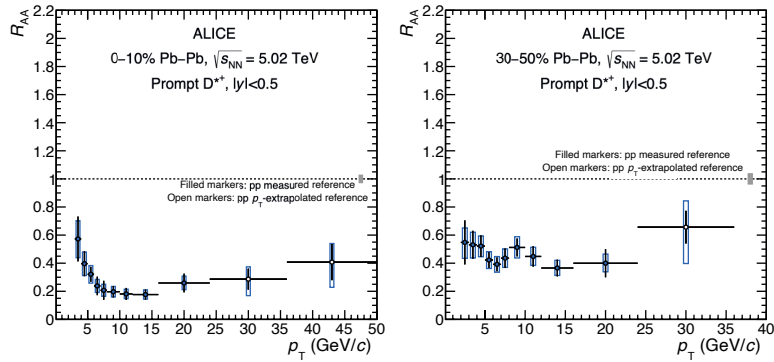


FIGURE 5.22: R_{AA} of prompt D^{*+} mesons in the 0–10% and 30–50% centrality classes in Pb–Pb collisions at $\sqrt{s_{NN}} = 5.02 \text{ TeV}$.

The D^{*+} nuclear modification factor (R_{AA}) can be computed from the ratio between the transverse momentum production yields in Pb–Pb collisions (dN_{AA}/dp_T) and the cross section in proton-proton collisions ($d\sigma_{pp}/dp_T$) scaled by the number of binary nucleon-nucleon collisions. The p_T -differential cross section of prompt D^{*+} mesons in pp collisions at $\sqrt{s} = 5.02 \text{ TeV}$, used as reference for the R_{AA} , were obtained by scaling the measurements at $\sqrt{s} = 7 \text{ TeV}$ to $\sqrt{s} = 5.02 \text{ TeV}$ with FONLL calculations [53]. The procedure is discussed in detail in [52]. Figure 5.22 shows the R_{AA} of D^{*+} mesons as a function of transverse momentum in central (left) and semi-central (right) collisions.

The nuclear modification factor of the D^{*+} is compatible within uncertainties with the other D-meson species (D^0 and D^+) in both centrality classes, as shown in Fig. 5.23. The uncertainties are obtained by propagating those on the Pb–Pb yields and those

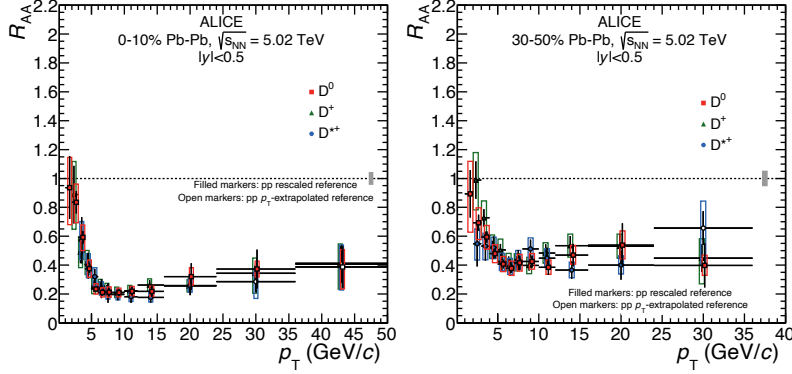


FIGURE 5.23: R_{AA} of prompt D^0 , D^+ and D^{*+} (in blue) mesons for the 0–10% and 30–50% centrality classes in Pb–Pb collisions at $\sqrt{s_{NN}} = 5.02$ TeV [51]. Statistical (bars), systematic (empty boxes), and normalisation (shaded box around unity) uncertainties are shown. Filled markers are obtained with the pp rescaled reference, empty markers with the p_T -extrapolated reference.

of the pp reference. The suppression of the D meson R_{AA} increases from semi-central to central collisions. The R_{AA} of the D^{*+} -meson shows minimum values of about 0.2 in the centrality class 0–10% and 0.4 in the centrality class 30–50%.

5.8 Average nuclear modification factor (D^0 , D^+ and D^{*+})

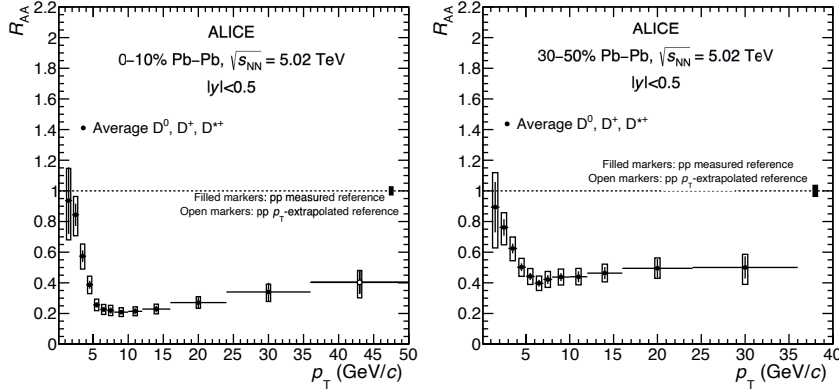


FIGURE 5.24: Average R_{AA} of the non-strange D-meson (D^0 , D^+ and D^{*+}) for the 0–10% and 30–50% centrality classes in Pb–Pb collisions at $\sqrt{s_{NN}} = 5.02$ TeV [51]. Statistical (bars), systematic (empty boxes), and normalisation (shaded box around unity) uncertainties are shown. Filled markers are obtained with the pp rescaled reference, empty markers with the p_T -extrapolated reference.

The nuclear modification factors of all D-meson species are consistent within the experimental uncertainties. The average was calculated in order to reduce the statistical

uncertainty and have a better comparison with models. The average nuclear modification factor of non-strange D mesons (D^0 , D^+ and D^{*+}) was computed using the inverse of the quadratic sum of the relative statistical and uncorrelated systematic uncertainties as weights, in the p_T interval where more than one D-meson species is available. The systematic errors were calculated by propagating the uncertainties through the weighted average, where the contribution from the tracking efficiency, the beauty hadron feed-down correction and the FONLL-based method scaling of $\sqrt{s} = 7$ TeV to $\sqrt{s_{NN}} = 5.02$ TeV were taken as a fully correlated among the three D-meson species.

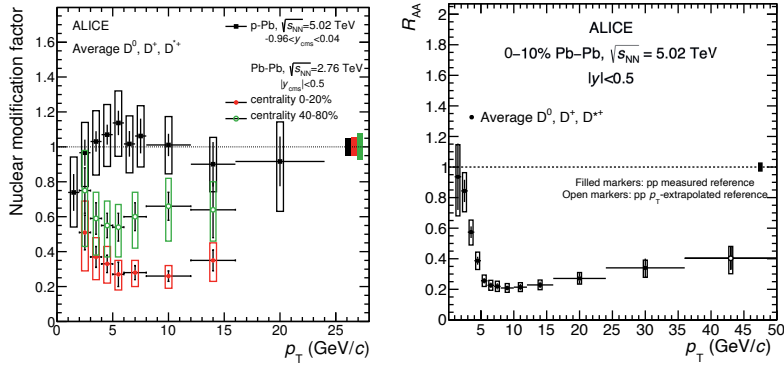


FIGURE 5.25: Left: average R_{pPb} of the non-strange D-meson in p-Pb collisions at $\sqrt{s_{NN}} = 5.02$ TeV compared to non-strange D-meson R_{AA} in the 0-20% and 40-80% centrality classes in Pb-Pb collisions at $\sqrt{s_{NN}} = 2.76$ TeV [54]. Right: average R_{AA} of the non-strange D-meson for the 0-10% centrality class in Pb-Pb collisions measured at the same energy.

The average R_{AA} of prompt D^0 , D^+ and D^{*+} mesons in Pb-Pb collisions for the 0-10% and 30-50% centrality classes are shown in Fig. 5.24. The two measurements show a suppression that is maximal at transverse momentum 6-10 GeV/c. The suppression gets smaller with decreasing p_T for $p_T < 6$ GeV/c, and R_{AA} is compatible with unity for the p_T interval 1-3 GeV/c. The average R_{AA} shows minimum values of 0.2 and 0.4 in the 0-10% and 30-50% centrality classes at p_T of 6-10 GeV/c, respectively. On the left panel of figure 5.25 is reported the average R_{pPb} of non-strange D mesons measured in p-Pb collisions at $\sqrt{s_{NN}} = 5.02$ TeV, compared with the non-strange D-meson R_{AA} measured in the 0-20% and 40-80% centrality classes in Pb-Pb collisions at $\sqrt{s_{NN}} = 2.76$ TeV [54] while the right panel of the same figure shows the average R_{AA} of non-strange D mesons measured in Pb-Pb collisions at $\sqrt{s_{NN}} = 5.02$ TeV. Since no significant modification of the D-meson production is observed in p-Pb collisions, the strong suppression observed in Pb-Pb collisions, i.e. for $p_T > 3$ GeV/c, cannot be explained by the cold-nuclear-matter effects and, therefore, can be attributed to final-state effects and in particular parton in-medium energy loss.

5.9 D mesons nuclear modification factor vs models

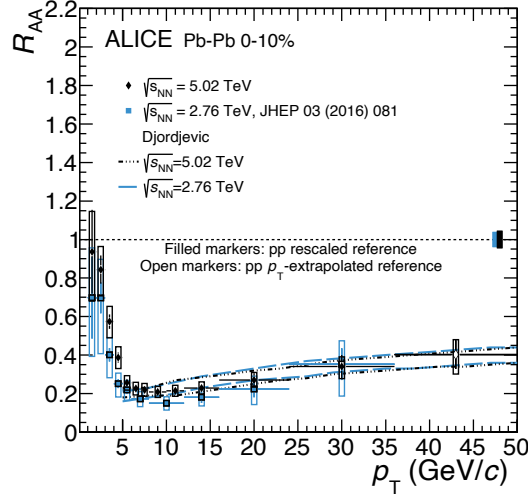


FIGURE 5.26: Average R_{AA} of non-strange D mesons compared with the Djordjevic model [15] in the 0–10% centrality class at two collisions energies. Statistical (bars), systematic (empty boxes), and normalisation (shaded box) uncertainties are shown.

Figure 5.26 shows the comparison of the nuclear modification factor of non-strange D mesons in Pb–Pb collisions at $\sqrt{s_{NN}} = 5.02$ TeV with the one calculated at $\sqrt{s_{NN}} = 2.76$ TeV at the same centrality class 0–10% [47]. The measurements with Run 2 data have better precision in terms of uncertainties (total uncertainties reduced by a factor of about two) and extended p_T coverage from 36–50 GeV/c. The suppression between the two measurements is compatible within uncertainties. The average R_{AA} measurements at the two energies are well reproduced by the Djordjevic model [15]. It results from the combination of a higher medium temperature at Run 2 energies (estimated to be about 7% higher than at Run 1 energies), which would decrease the R_{AA} by about 10%, with a harder p_T distribution of charm quarks at Run 2 energies, which would increase the R_{AA} by about 5% if the medium temperature were the same between the two center of mass energies.

The interactions of heavy quarks with the medium constituents in the Djordjevic [15], BAMPS [21], CUJET3.0 [16], MC@sHQ+EPOS2 [20], and LBT [22] models, is computed considering radiative and collisional processes in the calculations. Only collisional processes are taken into account in the model calculations POWLANG [55], TAMU [18], and PHSD [23]. The BAMPS model considers two different options: including only collisional interactions in a static medium which is called BAMPS el., or including both collisional and radiative energy loss which is called BAMPS el.+rad. The SCET [17] model is an effective field theory describing the dynamics of soft and collinear quarks and gluons in the presence of hard interactions. It includes

the interactions with the medium that are mediated by Glauber gluon exchange and heavy quark masses. Glauber gluons are soft gluons with the transverse momenta much larger than their momentum components along the directions of initial hadrons [56].

The medium is described using an underlying hydrodynamical model in CUJET3.0, LBT, MC@sHQ+EPOS2, BAMPS, POWLANG, TAMU and PHSD, while Djordjevic uses a Glauber model nuclear overlap without radial expansion. The initial heavy-quark p_T distributions are based on next-to-leading order (NLO) or FONLL perturbative QCD calculations in all model calculations, except for LBT model which uses the PYTHIA event generator. The EPS09 NLO parametrisation of the nuclear parton distribution functions is included by POWLANG, MC@sHQ+EPOS2, TAMU, PHSD and LBT.

All model calculations use in-vacuum fragmentation of heavy quarks for the high transverse momentum region. At low p_T region this is supplemented by hadronisation via recombination in the MC@sHQ+EPOS2, POWLANG, LBT and PHSD models.

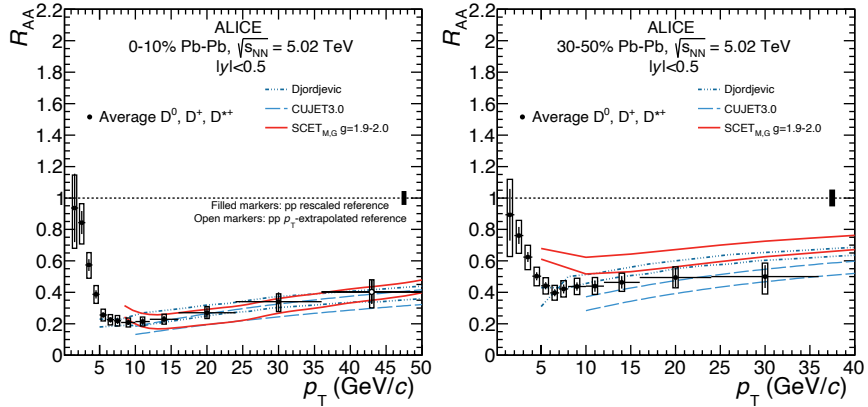


FIGURE 5.27: Average p_T -differential R_{AA} of prompt D mesons in the 0–10% and 30–50% centrality classes compared to pQCD models [15, 16, 17].

The average R_{AA} of non-strange D mesons are compared with perturbative QCD models in Fig. 5.27. In 0–10% centrality class (Fig. 5.27 on the left panel), the Djordjevic [15], CUJET3.0 [16] and SCET [17] models provide a fair description of the R_{AA} for $p_T > 10$ GeV/c. The Djordjevic and CUJET3.0 models include energy loss processes (radiative and collisional) in their calculations, while SCET model includes finite quark masses and Glauber gluons that describe the interaction of collinear partons with the medium constituents. In addition, the SCET and Djordjevic models also consider a nuclear modification of the parton distribution functions in their calculations. In the 30–50% centrality class, the Djordjevic and CUJET3.0 models reproduce well the R_{AA} above 10 GeV/c, while SCET model overestimates its magnitude. For $p_T > 10$ GeV/c, both CUJET3.0 and Djordjevic models provide a fair

description of the R_{AA} in central and semi-central collisions, where radiative energy loss is expected to be the dominant interaction mechanism.

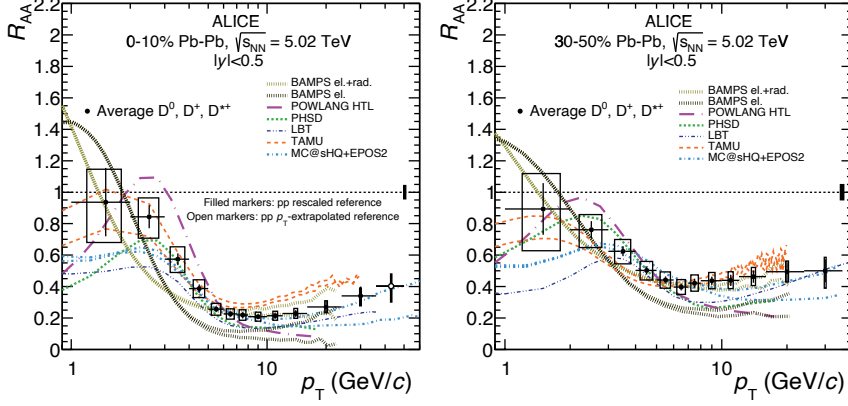


FIGURE 5.28: Average p_T -differential R_{AA} of prompt D mesons in the 0–10% and 30–50% centrality classes compared to transport model predictions [18, 20, 21, 22, 23, 55].

In figure 5.28, the non-strange D-meson R_{AA} are compared with the transport models. Transport models, BAMPs el. [21], POWLANG [55] and TAMU [18] include collisional energy loss processes to describe the interactions of heavy quarks with the medium, while BAMPs el.+rad. [21], LBT [22], MC@sHQ+EPOS2 [20] and PHSD [23] include collisional energy loss processes and medium-induced gluon radiations. Most of the models provide a fair description of the R_{AA} in the 0–10% centrality class for $p_T < 10$ GeV/c, while BAMPs el., and POWLANG show some tension with respect to the data. For $p_T > 10$ GeV/c, the BAMPs el.+rad., and MC@sHQ+EPOS2 models can describe well the data in the central collisions, while the BAMPs el., POWLANG and PHSD models underestimate its magnitude and TAMU model overestimates the R_{AA} . The POWLANG, TAMU, LBT, MC@sHQ and PHSD models include a nuclear modification of the parton distribution functions. Moreover, they also include a contribution of hadronization via quark recombination, in addition to the independent fragmentation.

In the 30–50% centrality class for $p_T < 10$ GeV/c, most of the models provide a fair description of the data, while BAMPs el. which does not include the radiative term, tend to overshoot the data. At p_T larger than 10 GeV/c in semi-central collisions, the TAMU, BAMPs el.+rad. and MC@sHQ+EPOS2 models reproduce well the R_{AA} . As clear from the discussion above, the R_{AA} measurement raises interesting questions once compared with models. However, due to the relatively large statistical uncertainties, it does not allow yet clear discrimination among the different models, and therefore it does not allow to extract quantitative information. The results with high statistics will be discussed in the next chapter.

Chapter 6

High precision measurements using Pb–Pb 2018 data sample

6.1 Introduction

The high statistic data sample collected by the ALICE apparatus in 2018, about a factor of 10 larger than what collected in 2015 data acquisition campaign, allows for a precision measurement of the D mesons nuclear modification factor and, therefore, for a comparison of the non-strange D mesons (D^0 , D^+ and D^{*+}) with D_s^+ and the light flavour sector in order to investigate the expected mass effect on the in-medium energy loss and the possible in-medium hadronization via recombination. Finally, the larger precision enables a more quantitative comparison with theoretical models.

The events were collected using specific centrality triggers, a dedicated central and semi-central trigger configuration (see chapter 4, subsection 4.3.1). The run lists were used in the analysis are those provided by the Data Preparation Group (for a detailed discussion, see chapter 3). The number of events analyzed was 88×10^6 for the 0–10% centrality class (integrated luminosity of $130 \mu\text{b}^{-1}$) and 76×10^6 for the 30–50% centrality class (integrated luminosity of $56 \mu\text{b}^{-1}$).

The signal extraction is based on topological selections of displaced secondary vertices. Single track and topological selection criteria were applied to maximize the significance of the D^{*+} signal in the various transverse momentum bins. The single track selection criteria are given in Table 6.1. The topological and kinematic cuts used to select the

TABLE 6.1: Topological and kinematic selections applied for the D^{*+} analysis in the 0–10% centrality class.

Track selection	threshold value
D^0 daughter track	ITSrefit and TPCrefit
Soft pion track (π_s^+)	ITSrefit
Cluster in ITS	≥ 4 , for which ≥ 1 in SPD
Cluster in TPC	≥ 70 (out of 159)
TPC, TOF particle identification	2σ , 3σ for 0–10% ; 3σ , 3σ for 30–50%

D^{*+} meson signal in 0–10% and 30–50% centrality class from 2018 data sample Pb–Pb collisions are reported in Tables 6.2 and 6.3.

TABLE 6.2: Topological and kinematic selections applied for the D^{*+} analysis in the 0–10% centrality class.

p_T (GeV/ c) interval	[3,3.5]	[3.5,4]	[4,4.5]	[4.5,5]	[5,5.5]	[5.5,6]	[6,6.5]	[6.5,7]	[7,7.5]	[7.5,8]
ΔM_{D^0} (GeV)	0.024	0.024	0.03	0.03	0.032	0.032	0.034	0.034	0.036	0.036
DCA (cm)	0.021	0.021	0.021	0.021	0.021	0.021	0.021	0.021	0.021	0.021
$\cos(\theta^*)$	0.8	0.8	0.9	0.9	0.9	0.9	1.0	1.0	1.0	1.0
$p_T(\pi)$ (GeV/ c)	0.9	0.9	0.9	0.9	0.9	0.9	0.9	0.9	0.9	0.9
$p_T(K)$ (GeV/ c)	1.0	1.0	0.9	0.9	0.9	0.9	0.9	0.9	0.9	0.9
$d_{0,K}$ (cm)	0.1	0.1	0.1	0.1	0.1	0.1	0.1	0.1	0.1	0.1
$d_{0,\pi}$ (cm)	0.1	0.1	0.1	0.1	0.1	0.1	0.1	0.1	0.1	0.1
$d_{0,K} \times d_{0,\pi}$ (10^{-3}) (cm ²)	-4.5	-4.5	-3.5	-3.5	-3.0	-3.0	-2.0	-2.0	-1.27	-1.27
$\cos(\theta_{point})$	0.98	0.98	0.98	0.98	0.95	0.95	0.93	0.93	0.93	0.93
$\cos(\theta_{point})XY$	0.998	0.998	0.998	0.998	0.998	0.998	0.998	0.998	0.998	0.998
NDL _{XY}	7.5	7.5	7	7	6.5	6.5	6.5	6.5	6	6

p_T (GeV/ c) interval	[8,9]	[9,10]	[10,12]	[12,16]	[16,24]	[24,36]	[36,50]
ΔM_{D^0} (GeV)	0.055	0.055	0.055	0.074	0.074	0.084	0.094
DCA (cm)	0.021	0.021	0.021	0.021	0.021	0.02	0.02
$\cos(\theta^*)$	1.0	1.0	1.0	1.0	1.0	1.0	1.0
$p_T(\pi)$ (GeV/ c)	0.9	0.9	0.9	0.7	0.5	0.5	0.5
$p_T(K)$ (GeV/ c)	0.9	0.9	0.9	0.7	0.5	0.5	0.5
$d_{0,K}$ (cm)	0.15	0.15	0.15	0.15	0.15	0.2	0.2
$d_{0,\pi}$ (cm)	0.15	0.15	0.15	0.15	0.15	0.2	0.2
$d_{0,K} \times d_{0,\pi}$ (10^{-3}) (cm ²)	-7.5×10^{-2}	-7.5×10^{-2}	-7.5×10^{-2}	-7.5×10^{-2}	-5×10^{-2}	4	4
$\cos(\theta_{point})$	0.93	0.93	0.93	0.93	0.92	0.87	0.8
$\cos(\theta_{point})XY$	0.998	0.998	0.99	0.99	0.99	0.9	0.9
NDL _{XY}	5	5	5	3.7	1	0.5	0

TABLE 6.3: Topological and kinematic selections applied for the D^{*+} analysis in the 30–50% centrality class.

p_T (GeV/c) interval	[2,2.5]	[2.5,3]	[3,3.5]	[3.5,4]	[4,4.5]	[4.5,5]	[5,5.5]	[5.5,6]	[6,6.5]	[6.5,7]
ΔM_{D^0} (GeV)	0.025	0.025	0.032	0.032	0.032	0.032	0.04	0.04	0.043	0.043
DCA (cm)	0.023	0.023	0.022	0.022	0.022	0.022	0.021	0.021	0.021	0.021
$\cos(\theta^*)$	0.8	0.8	0.8	0.8	0.8	0.8	1.0	1.0	1.0	1.0
$p_T(\pi)$ (GeV/c)	1.0	1.0	1.0	1.0	1.0	1.0	1.0	1.0	1.0	1.0
$p_T(K)$ (GeV/c)	1.0	1.0	1.0	1.0	1.0	1.0	1.0	1.0	1.0	1.0
$d_{0,K}$ (cm)	0.1	0.1	0.1	0.1	0.1	0.1	0.1	0.1	0.12	0.12
$d_{0,\pi}$ (cm)	0.1	0.1	0.1	0.1	0.1	0.1	0.1	0.1	0.12	0.12
$d_{0,K} \times d_{0,\pi} (10^{-3})$ (cm ²)	-3.5	-3.5	-3.0	-3.0	-3.0	-3.0	-2.3	-2.3	-1.0	-1.0
$\cos(\theta_{point})$	0.94	0.94	0.93	0.93	0.93	0.93	0.93	0.93	0.93	0.93
$\cos(\theta_{point})_{XY}$	0.998	0.998	0.998	0.998	0.998	0.998	0.998	0.998	0.998	0.998
NDL _{XY}	7	7	6.7	6.7	6.5	6.5	6.5	6.5	6.4	6.4

p_T (GeV/c) interval	[7,7.5]	[7.5,8]	[8,9]	[9,10]	[10,12]	[12,16]	[16,24]	[24,36]
ΔM_{D^0} (GeV)	0.045	0.045	0.055	0.055	0.06	0.074	0.74	0.094
DCA (cm)	0.021	0.021	0.021	0.021	0.021	0.021	0.021	0.02
$\cos(\theta^*)$	1.0	1.0	1.0	1.0	1.0	1.0	1.0	1.0
$p_T(\pi)$ (GeV/c)	1.0	1.0	0.9	0.9	0.9	0.7	0.5	0.5
$p_T(K)$ (GeV/c)	1.0	1.0	0.9	0.9	0.9	0.7	0.5	0.5
$d_{0,K}$ (cm)	0.12	0.12	0.12	0.12	0.15	0.15	0.15	0.2
$d_{0,\pi}$ (cm)	0.12	0.12	0.12	0.12	0.15	0.15	0.15	0.2
$d_{0,K} \times d_{0,\pi} (10^{-3})$ (cm ²)	-1.0×10^{-2}	-1.0×10^{-2}	-7.5×10^{-2}	-7.5×10^{-2}	-7.5×10^{-2}	-7.5×10^{-2}	-5×10^{-2}	4
$\cos(\theta_{point})$	0.93	0.93	0.93	0.93	0.93	0.93	0.92	0.85
$\cos(\theta_{point})_{XY}$	0.998	0.998	0.998	0.998	0.998	0.99	0.99	0.9
NDL _{XY}	6.4	6.4	4.7	4.7	4.7	3.7	2	0

6.2 Raw yield extraction

The D^{*+} raw yields were extracted by performing a fit to the mass difference $\Delta M = M(K\pi\pi) - M(K\pi)$ distributions with a function composed of a Gaussian for the signal and the term describing the background shape is an exponential convoluted with a power law according to the equation 5.1.

Figure 6.1, 6.2 and 6.3 show the D^{*+} invariant-mass distributions in the 0–10% centrality class in the transverse momentum range 3–50 GeV/ c and in the 30–50% centrality class in the transverse momentum range 2–36 GeV/ c .

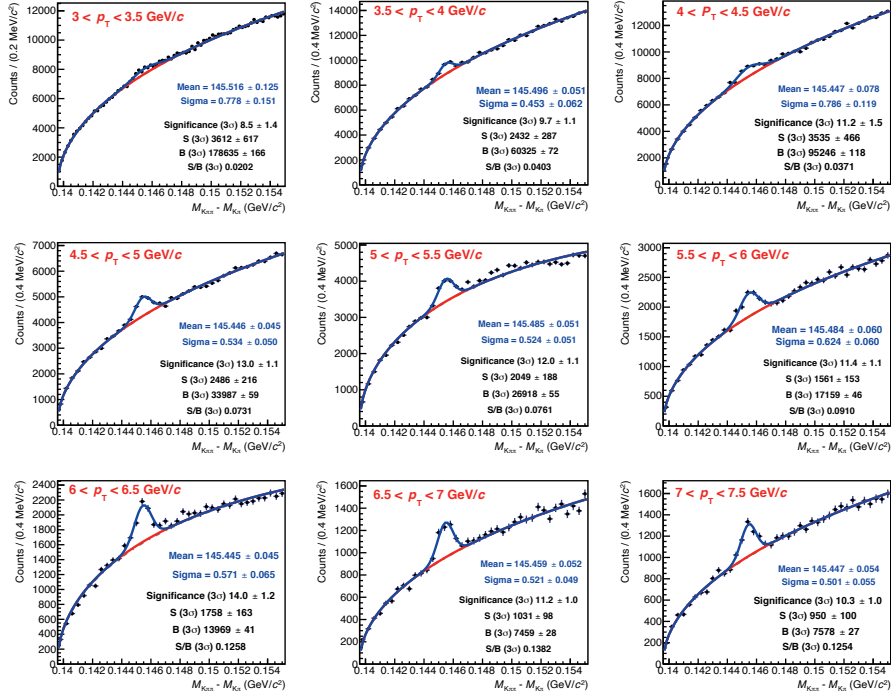


FIGURE 6.1: ΔM invariant-mass distributions of the D^{*+} candidates in the 0–10% centrality class in the range $3 < p_T < 7.5$ GeV/ c . Fitted values for the mean in MeV/ c^2 and sigma in GeV/ c^2 unit.

The goodness of the mass fit against the Monte Carlo (MC) expectation was checked for each p_T interval in terms of mass peak width and mean. The comparison between data and MC is reported in figures 6.4 and 6.5 for 0–10% and 30–50% centrality classes. The results show a good agreement of data and MC in terms of mass peak width and mean in most of the p_T ranges under consideration.

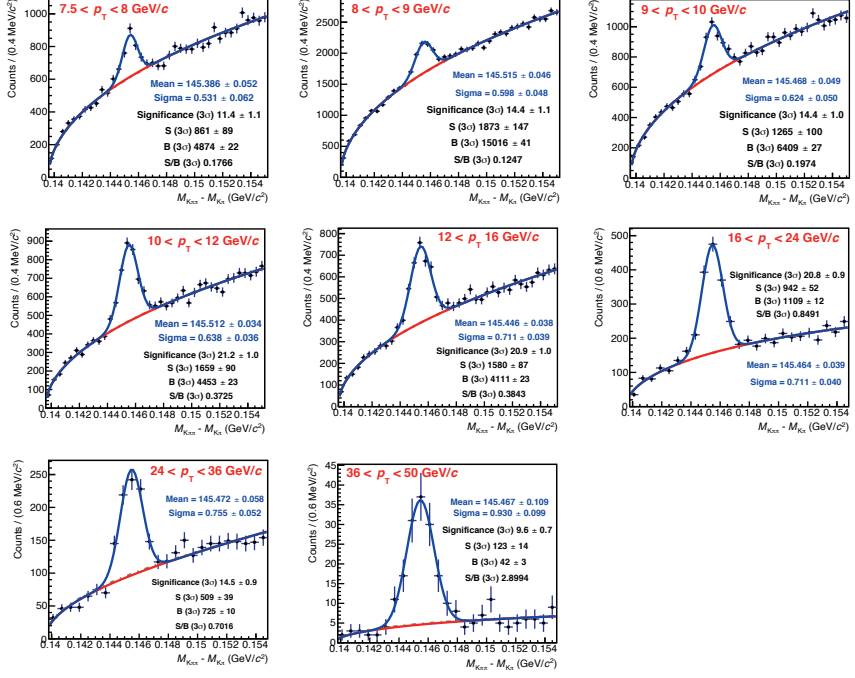


FIGURE 6.2: ΔM invariant-mass distributions of the D^{*+} candidates in the 0-10% centrality class in the range $7.5 < p_T < 50$ GeV/ c . Fitted values for the mean in MeV/ c^2 and sigma in GeV/ c^2 unit.

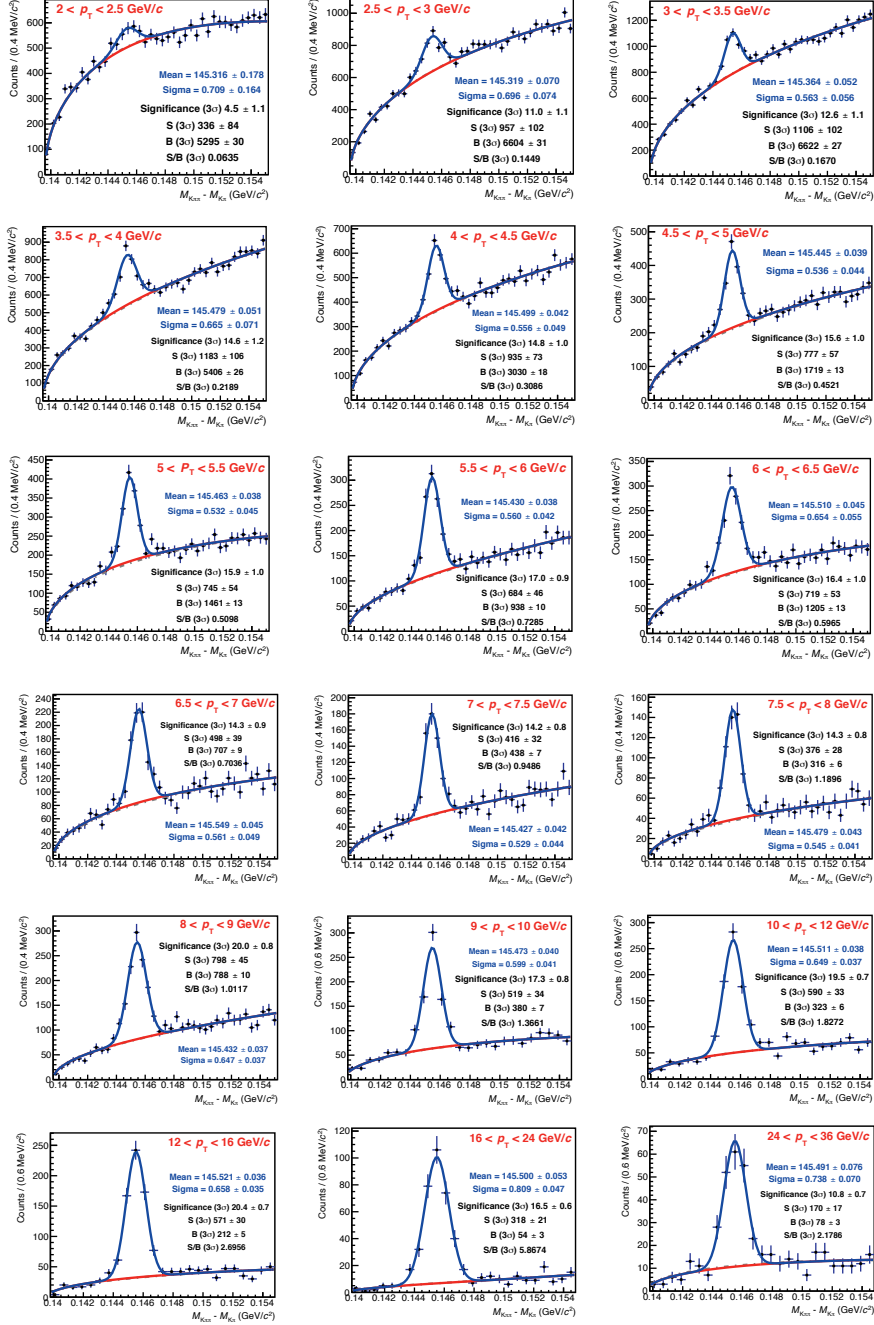


FIGURE 6.3: ΔM invariant-mass distributions of the D^{*+} candidates in the 30–50% centrality class in the range $2 < p_T < 36$ GeV/c. Fitted values for the mean in MeV/c² and sigma in GeV/c² unit.

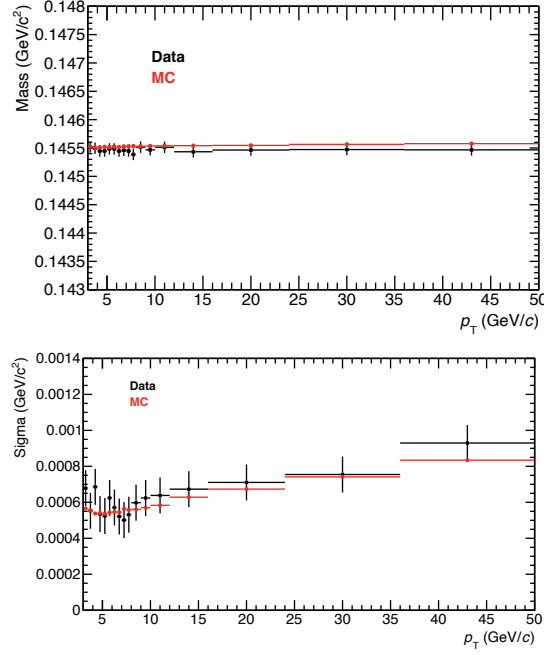


FIGURE 6.4: Comparison of Gaussian mean and width extracted from the invariant-mass fits of D^{*+} candidates in the 0–10% centrality class for the data (in black) and the MC simulation (in red).

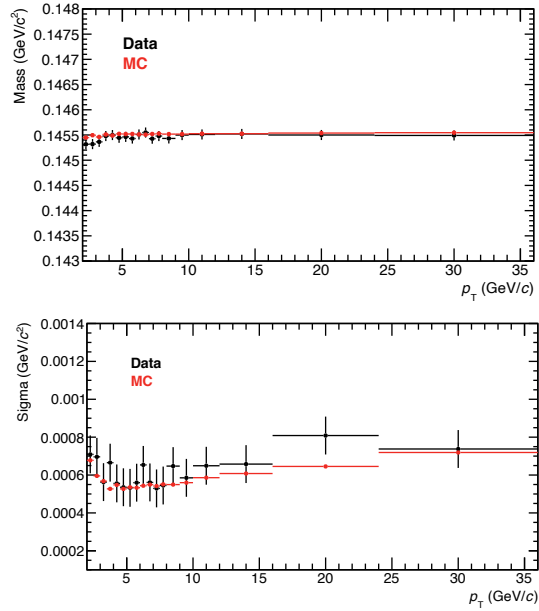


FIGURE 6.5: Comparison of Gaussian mean and width extracted from the invariant-mass fits of D^{*+} candidates in the 30–50% centrality class for the data (in black) and the MC simulation (in red).

6.3 Efficiencies

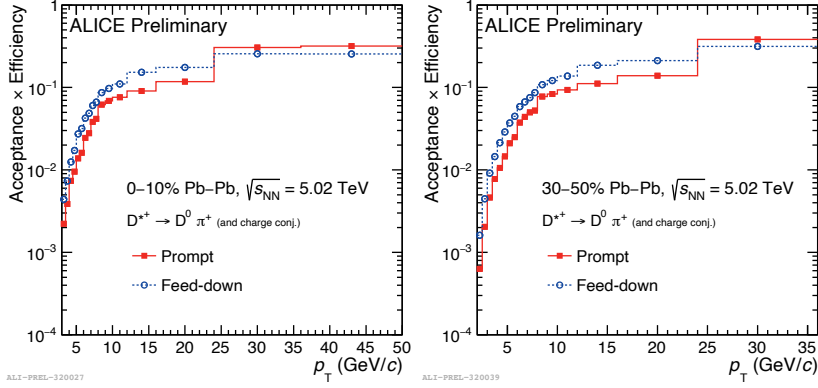


FIGURE 6.6: Production of acceptance and efficiency as a function of p_T for prompt (red squares) and feed-down (blue circles) D^{*+} meson in Pb–Pb collisions for the 0–10% centrality class (left panel) and for the 30–50% centrality class (right panel) obtained from MC simulations.

The correction for acceptance and efficiency ($\text{Acc} \times \varepsilon$) was determined using Monte Carlo simulations, including a transport package code [43] with a detailed description of the detector geometry and its response. The HIJING v1.383 event generator [42] is used to simulate the underlying Pb–Pb events and D-meson signals were added using the PYTHIA v6.421 event generator [41] with Perugia-2011 tune. The prompt yield of D mesons is obtained by subtracting from the inclusive yields the beauty-hadron decays estimated based on FONLL calculations [44, 50]. Figure 6.6 show the acceptance-times-efficiency correction ($\text{Acc} \times \varepsilon$) for prompt (red squares) and feed-down (blue circles) D^{*+} mesons with rapidity $|y| < y_{\text{fid}}(p_T)$ in the 0–10% and 30–50% centrality classes.

6.4 Systematic uncertainties

The sources of systematic uncertainties of the D^{*+} -meson analysis in Pb–Pb 2018 data sample are the same with the one in 2015 sample as already discussed in chapter 5, section 5.4. The same technique was used to determine the systematic on the yield extraction, topological selection, generated Monte Carlo p_T shape, and feed-down subtraction from beauty-hadron decays. For particle identification and track reconstruction efficiency, a different procedure was used to assign the systematic uncertainties. More details about the systematics of the 2018 data sample will be discussed in the following.

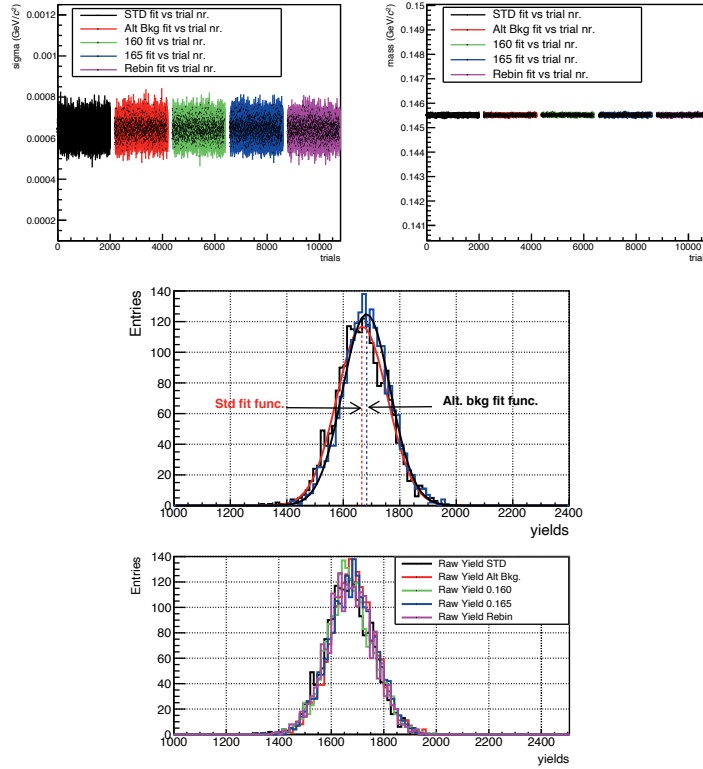


FIGURE 6.7: Multi trial results for $10 < p_T < 12$ GeV/c in the 0–10%. Top: Sigma and mass distributions versus trials at the same p_T interval and centrality class. Middle: Comparison of yield distributions with standard background fit function and alternative background fit function for p_T 5–6 GeV/c in the 30–50%. Bottom: Yield distributions for all variations in the same p_T interval and centrality class.

The comparison between the yield distributions using the standard background fit function and alternative background fit function after performing the multi trial is shown in Fig. 6.7 as well as the sigma and the mass distributions for each variation. The middle plot in figure 6.7 shows the yields with alternative background fit function

are shifted with respect to the standard background function due to the different background fit function. The same figure on the bottom shows all the yield distributions compared to the standard fit function. The systematic uncertainty was assigned by calculated the root mean square (RMS) of the yield difference of all variations with respect to the standard fit.

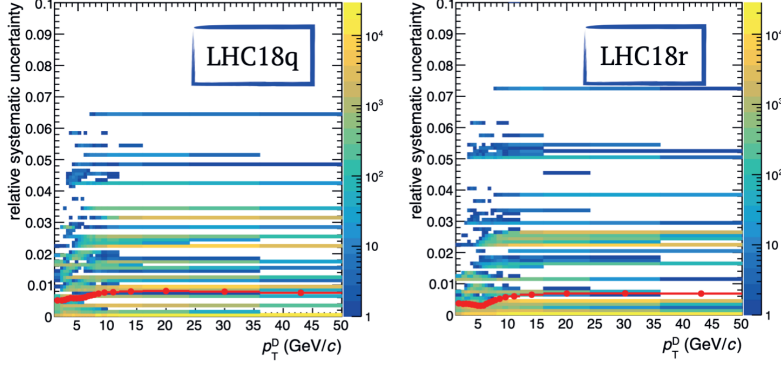


FIGURE 6.8: PID systematic in the 0–10% centrality class for Pb–Pb data sample 2018.

The systematic on the particle identification efficiency was evaluated with track-by-track study, using relatively pure samples of pions and kaons. However, in the Pb–Pb data sample 2018, a discrepancy between the TPC PID efficiency in data and Monte Carlo simulation up to 5% and 15% for 3σ and 2σ selection was observed. This was caused by an imperfect calibration of the expected dE/dx for the different hadron species in the data, which was reflected in a deviation of the number of σ distributions in the TPC from the Normal distribution. A data-driven approach was used to correct this discrepancy by fitting the pure samples of pions and kaons with Gaussian function to extract the mean and the width of the uncalibrated distributions of pions and kaons. The results are shown in Fig. 6.8 for the 0–10% centrality class. The same strategy was used for the 30–50% centrality class.

Another source of systematic is the topological selection criteria, which was evaluated by repeating the analysis by varying the selection criteria values, looser and tighter, with respect to the standard selection. These variations were significantly modifying the efficiencies, raw yields, and background values. The modification of the efficiencies, i.e. in the 0–10% centrality class, is shown in Fig. 6.9. The systematic uncertainty was assigned by comparing the corrected yields of the standard selection criteria with respect to the different variations of the selection.

The systematic uncertainty due to a possible difference between the real and simulated D-meson transverse momentum distributions was investigated. The uncertainty was estimated by using alternative p_T distributions. The systematic uncertainty was assigned considering the variation of the efficiency obtained by applying the FONLL

p_T distribution with respect to the result obtained by applying the FONLL and LBT p_T distribution in central collisions, which is shown in Fig. 6.10. The same procedure was done for semi-central collisions by comparing the FONLL p_T distribution and the FONLL and BAMPS p_T distribution to estimate the systematic uncertainty.

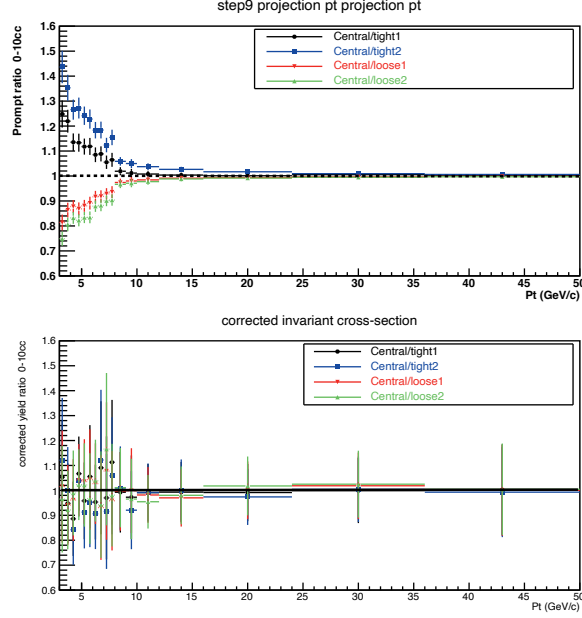


FIGURE 6.9: Topological selection systematic in the 0–10% centrality class.

The systematic uncertainty due to the track-reconstruction efficiency includes the contributions of the track-finding procedure in the TPC detector and prolongation in the ITS detector, and the track-quality selections. The same strategy with the Pb–Pb 2015 data sample analysis was used to evaluate the systematic by varying the track-quality selection criteria and by comparing the probability to match the TPC tracks to the ITS hits in data and simulation. The systematic uncertainty on tracking efficiency assigned for D^{*+} analysis is shown in Fig. 6.11 for Pb–Pb data sample 2018 in the 30–50% centrality class.

The systematic uncertainty on the subtraction of feed-down from beauty-hadron decays (i.e. the calculation of the f_{prompt} fraction) was estimated by varying:

- the p_T -differential feed-down D^{*+} -meson cross section from the FONLL calculations within the theoretical uncertainties,
- the ratio of the feed-down and prompt D^{*+} -meson R_{AA} hypothesis.

Figure 6.12 shows the D^{*+} R_{AA} after feed-down subtraction on the left, and the variation of R_{AA}^{prompt} as a function of the feed-down and prompt R_{AA} ratio hypothesis

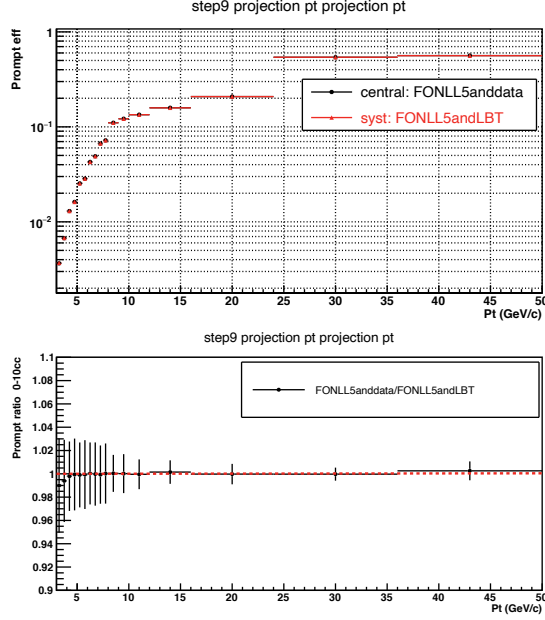


FIGURE 6.10: MC p_T shape distributions systematic in the 0–10% centrality class.

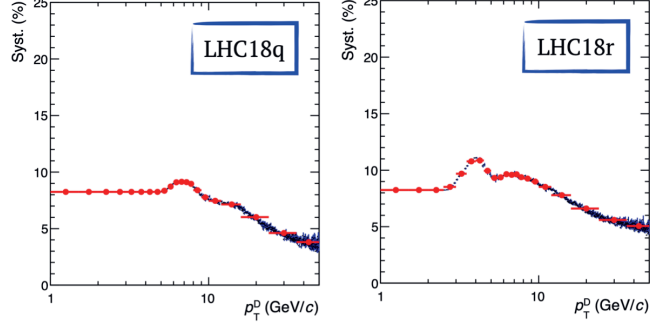


FIGURE 6.11: Systematic uncertainty on tracking efficiency in the 30–50% centrality class.

on the right. The resulting uncertainty ranges between 1% and 7% depending on the centrality classes and p_T interval. The summary of the systematic uncertainties is shown in Fig. 6.13 for both centrality classes. The systematic uncertainties for the 0–10% and 30–50% centrality classes are reported in Table 6.4 and 6.5.

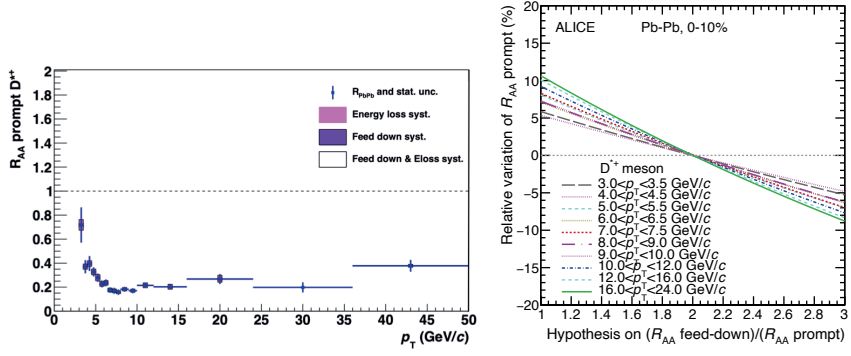


FIGURE 6.12: Systematic uncertainty from feed-down and R_{AA} hypothesis in the various p_T interval in the 0-10% centrality class.

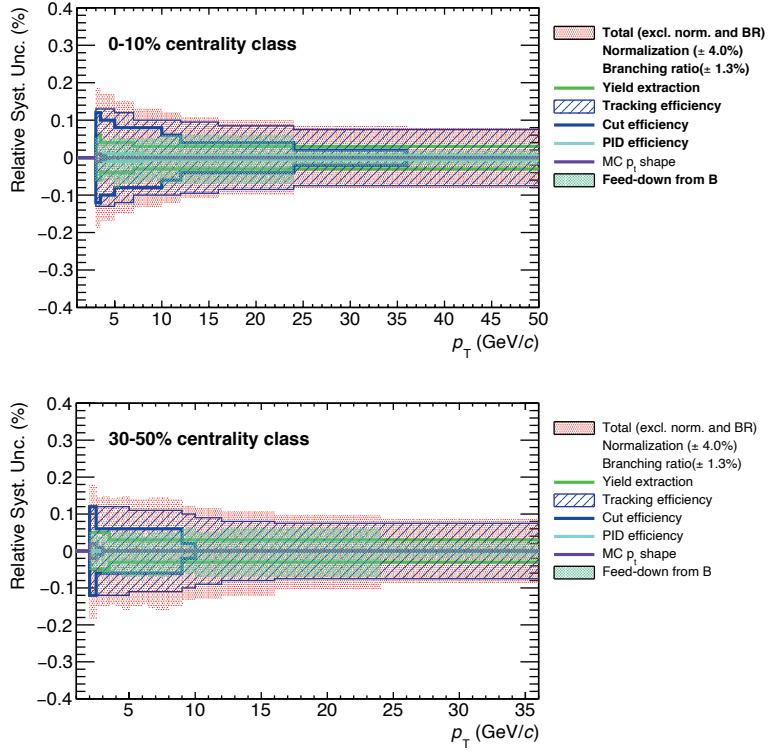


FIGURE 6.13: Summary of systematic uncertainties for the 0-10% and 30-50% centrality classes.

TABLE 6.4: Systematic uncertainties for the 0–10% centrality class.

p_T interval (GeV/ c)	[3,3.5]	[3.5,4]	[4,4.5]	[4.5,5]	[5,5.5]	[5.5,6]	[6,6.5]	[6.5,7]	[7,7.5]
Yield extraction	6%	4%	4%	4%	4%	4%	4%	4%	3%
Tracking efficiency	13.2%	13.2%	13.2%	13.2%	12.3%	12.3%	12.3%	12.3%	10.3%
PID efficiency	1%	1%	1%	1%	1%	1%	1%	1%	1%
Cut efficiency	12%	10%	10%	10%	8%	8%	8%	8%	8%
Monte Carlo p_T shape	1%	0.5%	0	0	0	0	0	0	0
Feed-down subtraction	+5% -6%	+5% -6%	+4% -5%	+5% -6%	+6% -8%	+5% -7%	+5% -7%	+5% -7%	+5% -7%

p_T interval (GeV/ c)	[7.5,8]	[8,9]	[9,10]	[10,12]	[12,16]	[16,24]	[24,36]	[36,50]
Yield extraction	3%	3%	3%	3%	3%	3%	3%	3%
Tracking efficiency	10.3%	10.3%	10.3%	10.3%	9.3%	8.4%	7.4%	7.4%
PID efficiency	1%	0.5%	0.5%	0.5%	0.5%	0.5%	0.5%	0.5%
Cut efficiency	8%	8%	8%	6%	4%	4%	2%	0
Monte Carlo p_T shape	0	0	0	0	0	0	0	0
Feed-down subtraction	+5% -6%	+5% -6%	+5% -6%	+6% -7%	+6% -7%	+6% -7%	+2% -2%	+2% -2%

TABLE 6.5: Systematic uncertainties for the 30–50% centrality class.

p_T interval (GeV/ c)	[2,2.5]	[2.5,3]	[3,3.5]	[3.5,4]	[4,4.5]	[4.5,5]	[5,5.5]	[5.5,6]	[6,6.5]
Yield extraction	5%	5%	5%	3%	3%	3%	3%	3%	3%
Tracking efficiency	12.2%	12.2%	12.2%	12.2%	12.2%	12.2%	11.2%	11.2%	11.2%
PID efficiency	0	0	0	0	0	0	0	0	0
Cut efficiency	12%	6%	6%	6%	6%	6%	6%	6%	6%
Monte Carlo p_T shape	2%	1%	0	0	0	0	0	0	0
Feed-down subtraction	+5% -5%	+4% -4%	+5% -6%	+4% -6%	+5% -6%	+5% -7%	+5% -7%	+5% -7%	+4% -6%

p_T interval (GeV/ c)	[6.5,7]	[7,7.5]	[7.5,8]	[8,9]	[9,10]	[10,12]	[12,16]	[16,24]	[24,36]
Yield extraction	3%	3%	3%	3%	3%	3%	3%	3%	3%
Tracking efficiency	11.2%	11.2%	11.2%	11.2%	10.2%	9.2%	8.2%	7.3%	7.3%
PID efficiency	0	0	0	0	0	0	0	0	0
Cut efficiency	6%	6%	6%	6%	2%	0	0	0	0
Monte Carlo p_T shape	0	0	0	0	0	0	0	0	0
Feed-down subtraction	+5% -7%	+5% -7%	+5% -7%	+5% -6%	+6% -6%	+5% -7%	+6% -7%	+6% -7%	+2% -2%

6.5 D^{*+} transverse momentum distributions

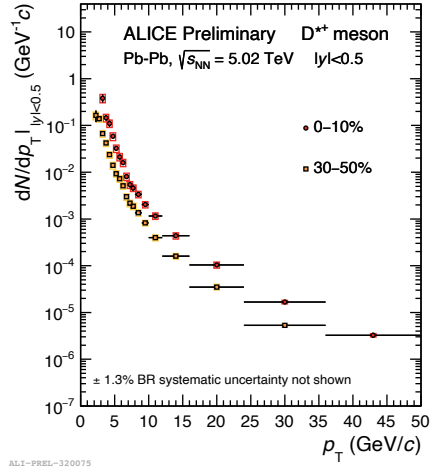


FIGURE 6.14: Transverse momentum distributions dN/dp_T of prompt D^{*+} meson in the 0–10% and 30–50% centrality classes in Pb–Pb collisions at $\sqrt{s_{NN}} = 5.02$ TeV.

The transverse momentum distributions dN/dp_T of prompt D^{*+} meson in Pb–Pb collisions at $\sqrt{s_{NN}} = 5.02$ TeV in the 0–10% and 30–50% centrality classes with 2018 data sample are shown in figure 6.14. The statistical uncertainties are presented by the vertical bars and the empty boxes are the systematic uncertainties. The branching ratios uncertainty is quoted separately. The corrected p_T spectra of the D^{*+} mesons are reported in finer p_T bins using 2018 data with respect to 2015 data, due to the large data sample collected in Pb–Pb collisions at $\sqrt{s_{NN}} = 5.02$ TeV in 2018. In addition, the p_T distributions dN/dp_T of D^{*+} mesons with the 2018 data sample have better statistical precision compared to Pb–Pb 2015 data in central and semi-central collisions, as shown in Fig. 6.15.

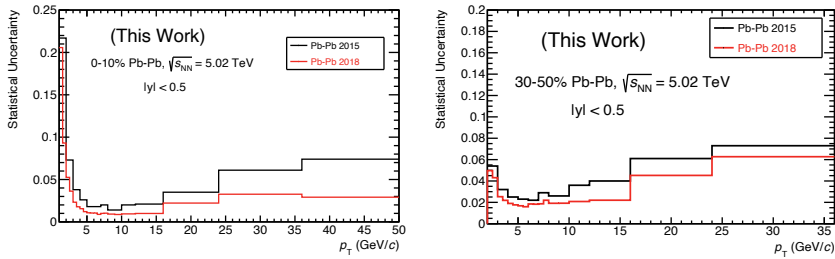


FIGURE 6.15: Statistical systematic uncertainty comparison between 2015 (in black) and 2018 (in red) Pb–Pb data sample at $\sqrt{s_{NN}} = 5.02$ TeV.

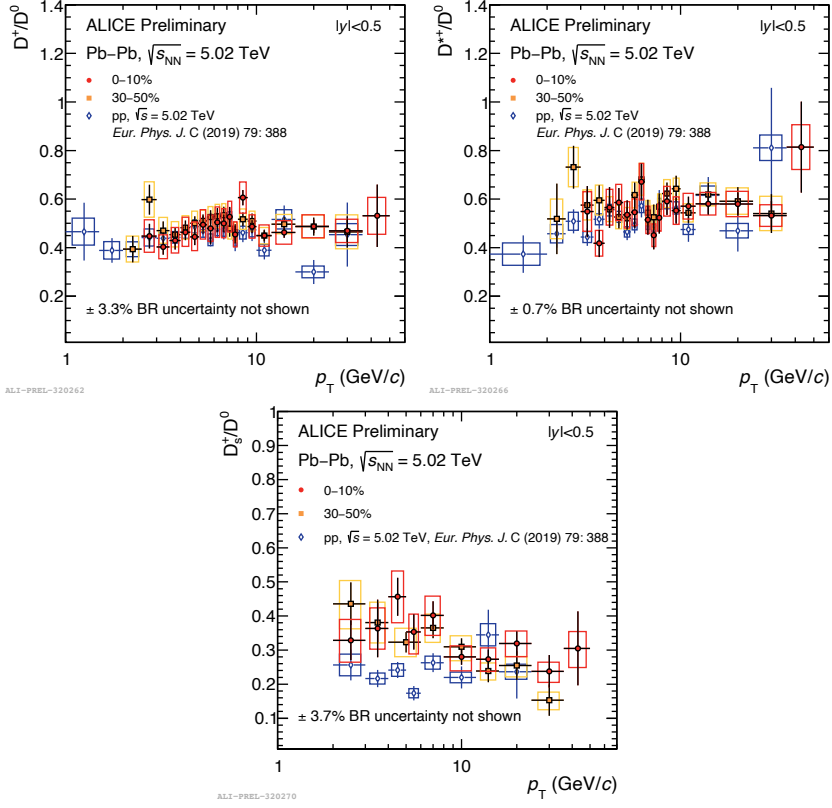


FIGURE 6.16: Ratios of prompt D^+/D^0 , D^{*+}/D^0 and D_s^+/D^0 as a function of p_T in pp and Pb–Pb collisions at the same energy.

The p_T dependent ratios of non-strange D-meson yields, D^+/D^0 , D^{*+}/D^0 and D_s^+/D^0 in Pb–Pb collisions at $\sqrt{s_{NN}} = 5.02$ TeV compared to the values measured in pp collisions at the same energy are shown in Fig. 6.16. The D^+/D^0 and D^{*+}/D^0 ratios in Pb–Pb collisions for both centrality classes are compatible within uncertainties with the ratios measured in pp collisions, indicating there is no significant modification of their relative abundances as a function of p_T and in centrality classes. The D_s^+/D^0 ratio in Pb–Pb collisions using the 2018 data sample is measured with a better precision with respect to 2015 Pb–Pb sample [51]. A hint of enhanced D_s^+/D^0 ratio in Pb–Pb compared to pp collisions is observed at transverse momentum range $8 < p_T < 10$ GeV/c, but the measurements in the two systems are compatible within uncertainties.

6.6 Proton-proton reference: with 2017 pp at $\sqrt{s_{\text{NN}}} = 5.02$ TeV data sample

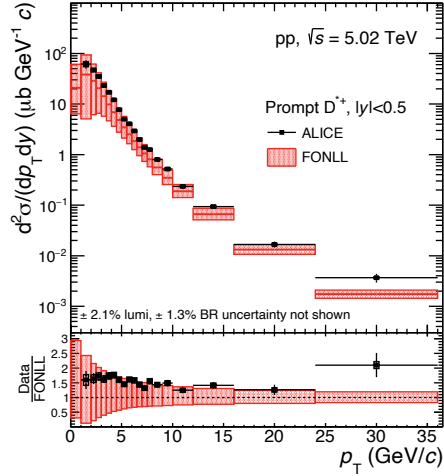


FIGURE 6.17: D^{*+} mesons p_T -differential cross section in pp collisions at $\sqrt{s} = 5.02$ TeV [57] compared to FONLL model calculations. The ratio of the data to the theoretical predictions are shown in the lower part of the figure.

The D^{*+} -meson pp production cross section is needed as reference to derive the nuclear modification factor. For 2018 Pb–Pb analysis, the new pp data sample collected in 2017 at $\sqrt{s_{\text{NN}}} = 5.02$ TeV was used as a reference for the R_{AA} calculation. The p_T -differential cross section of prompt D^{*+} -meson compared with the FONLL calculations is shown in Fig. 6.17. The cross section of the D^{*+} -meson is described by the FONLL calculations within uncertainties. The data lie systematically on the upper edge of the uncertainty band of the theoretical prediction. In the low and intermediate transverse momentum region, the data are a factor 10 more precise than the theory prediction and, therefore, set strong constraints on charm production. There is a discrepancy between the FONLL and the data within 2σ at the last p_T bin, $24 < p_T < 36$ GeV/ c . The pp reference discussed in this section has largely improved statistical and systematic uncertainties with respect to the one used for the R_{AA} obtained with 2015 Pb–Pb data sample. The comparison between the two references is shown in Fig. 6.18 with the same p_T bin.

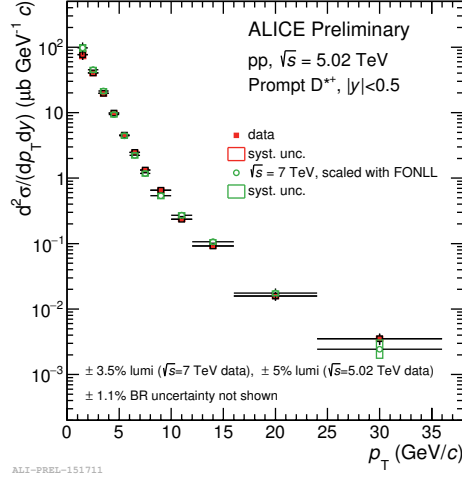


FIGURE 6.18: D^{*+} meson p_T -differential production cross section in pp collisions at $\sqrt{s} = 5.02$ TeV [57] compared to the energy scaling of the $\sqrt{s} = 7$ TeV [52] to $\sqrt{s} = 5.02$ TeV.

6.7 D meson nuclear modification factor

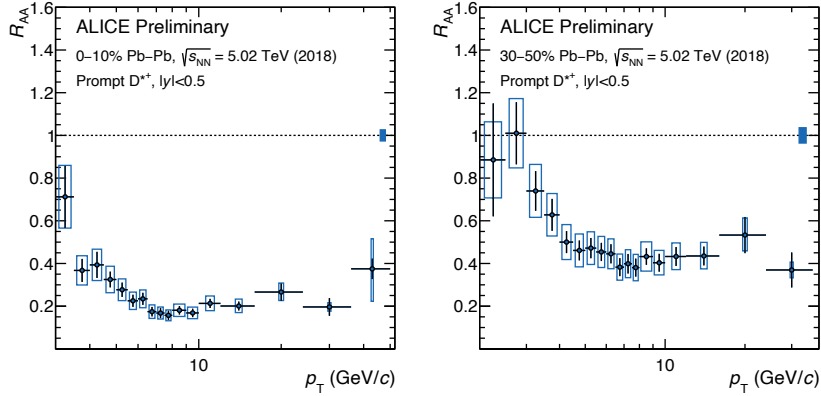


FIGURE 6.19: R_{AA} of prompt D^{*+} meson in the 0–10% and 30–50% centrality classes in Pb–Pb collisions at $\sqrt{s_{NN}} = 5.02$ TeV with data sample collected in 2018. R_{AA} in the 0–10% and 30–50% centrality classes are reported in the interval $3 < p_T < 50$ GeV/c and $2 < p_T < 36$ GeV/c.

The nuclear modification factor of prompt D^{*+} mesons as a function of transverse momentum measured in the 0–10% and 30–50% centrality classes is shown in Fig. 6.19. The figure on the left panel is the D^{*+} R_{AA} for the 0–10% centrality class in the p_T interval 3–50 GeV/c and on the right panel is for the 30–50% centrality class in the p_T interval 2–36 GeV/c.

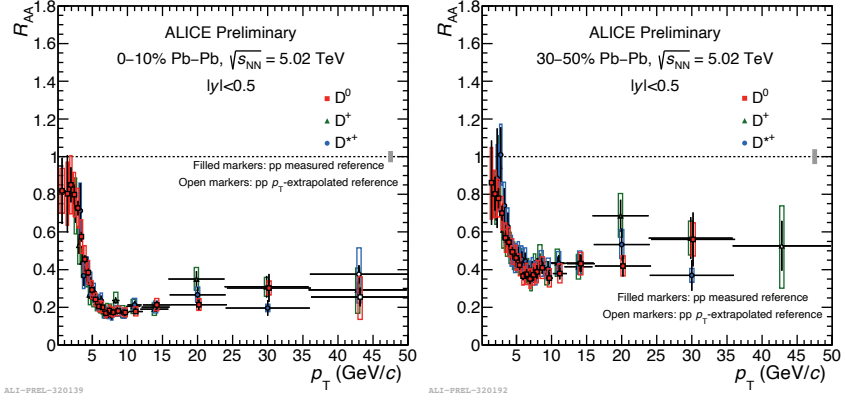


FIGURE 6.20: R_{AA} of prompt D^0 , D^+ and D^{*+} mesons in the 0–10% centrality class (left panel) and 30–50% centrality class (right panel) using 2018 Pb–Pb data sample at $\sqrt{s_{NN}} = 5.02$ TeV.

The p_T differential production cross section of prompt D^{*+} -meson in pp collisions at $\sqrt{s} = 5.02$ TeV discussed in the previous section [57] is used as reference. The large data sample collected in 2018 allows performing the R_{AA} measurement in finer p_T bins than the 2015 measurement for $p_T < 10$ GeV/ c . The two D^{*+} R_{AA} measurements are compatible within uncertainties with the other D-meson species, as is clear from figure 6.20. The observed suppression of the D mesons R_{AA} increases from semi-central to central collisions. The R_{AA} of D^{*+} -meson shows minimum values of about 0.15 in the 0–10% centrality class and about 0.35 in the 30–50% centrality class at $p_T = 6.5$ –8 GeV/ c .

6.8 Heavy vs light flavour sector

The nuclear modification factor is one of the observables that can allow understanding of the colour-charge and quark-mass dependence of the in-medium energy loss. The different energy loss processes can be tested by comparing the R_{AA} of prompt D mesons, charged π^\pm and charged particles in the same p_T interval, energy and centrality classes [58], as shown in Fig. 6.21. In central collisions, the difference between D mesons and charged π^\pm R_{AA} is above 5σ level at low transverse momentum below 4 GeV/ c . However at high p_T above 10 GeV/ c , it is compatible between D mesons, charged π^\pm and charged particles within uncertainties. In 30–50% centrality class the three R_{AA} measurements are compatible in the common p_T interval.

The interpretation of the difference between the D-meson and charged pion R_{AA} at p_T lower than 4 GeV/ c in central collisions is not straightforward, because several factors can play a role in defining the shape of the R_{AA} . In presence of a colour-charge and quark-mass dependent energy loss, the harder p_T distribution and the harder fragmentation function of charm quarks compared to those of light quarks

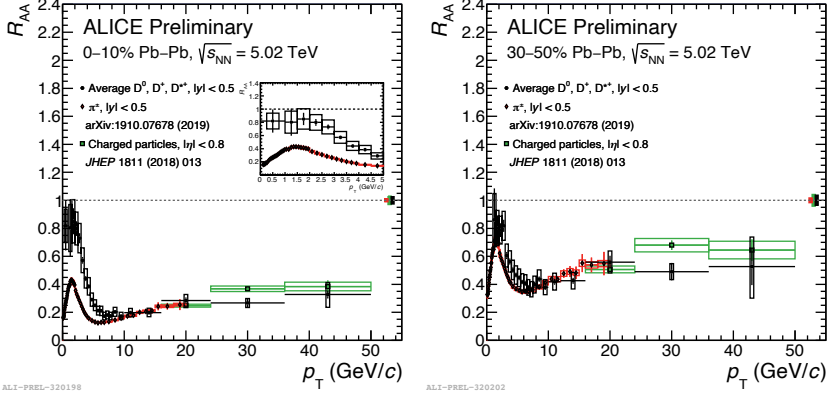


FIGURE 6.21: Average R_{AA} of D^0 , D^+ and D^{*+} mesons in the 0–10% and 30–50% centrality classes at $\sqrt{s_{NN}} = 5.02$ TeV compared with the charged π^\pm and charged particles R_{AA} in the same centrality classes and energy.

and gluons should lead to similar values of D-meson and pion nuclear modification factor, as discussed in Ref. [59]. The effects of radial flow and hadronisation via recombination, as well as initial-state effects, could also affect D-meson and light-hadron yields differently at a given p_T . Therefore, the theoretical predictions are needed to draw more firm conclusions for the comparison of the R_{AA} of prompt D mesons, charged π^\pm and charged particles.

6.9 Comparison with theory and investigation of hadronisation via recombination

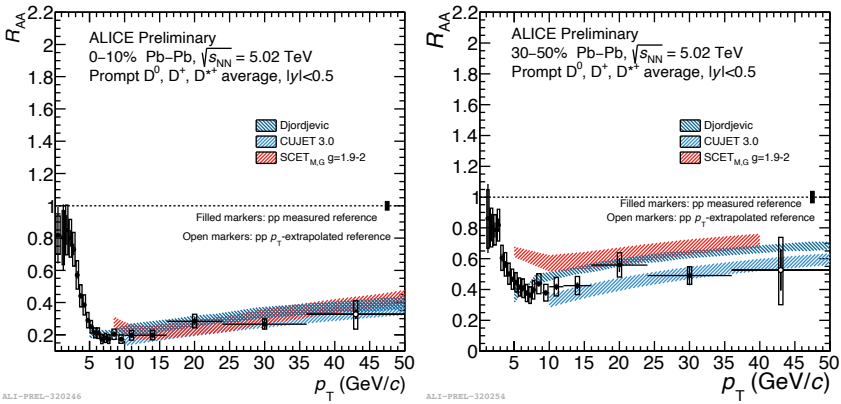


FIGURE 6.22: Average p_T -differential R_{AA} of prompt D^0 , D^+ and D^{*+} mesons in the 0–10% (left) and 30–50% (right) centrality classes compared to perturbative QCD model predictions [15, 16, 17].

One of the mechanism of hadron formation in heavy-ion collisions is via recombination.

Hadrons are produced by recombining the quarks which are collectively moving in the Quark-Gluon Plasma. In this section, the comparison between data and theoretical calculations will be discussed.

Figure 6.22 shows the average non-strange D-meson R_{AA} compared to perturbative QCD model predictions in both centrality classes, in the 0–10% and 30–50%, respectively. With the high precision measurements with 2018 data sample, the average R_{AA} is measured in finer p_T bins and down to zero p_T for the first time in central Pb–Pb collisions. The CUJET3.0 [16] and Djordjevic [15] models, which include both radiative and collisional energy loss processes, provide a fair description of the R_{AA} in both centrality classes for $p_T > 10$ GeV/ c , where radiative energy loss is expected to be the dominant interaction mechanism at high p_T . It gives us an indication that the dependence of radiative energy loss on the path length in the Quark-Gluon Plasma is well understood. The SCET [17] model reproduces well the R_{AA} for $p_T > 10$ GeV/ c in central collisions, while in semi-central collisions it overestimates the R_{AA} values. Instead of using radiative and collisional energy loss processes, the SCET contains finite quark masses as well as the interaction of collinear quarks and gluons with the medium in the calculations, where $g = 1.9 - 2$, as shown on the legend in Fig 6.22, is the coupling constant which describes how strongly the hard partons couple to the QCD medium in the model.

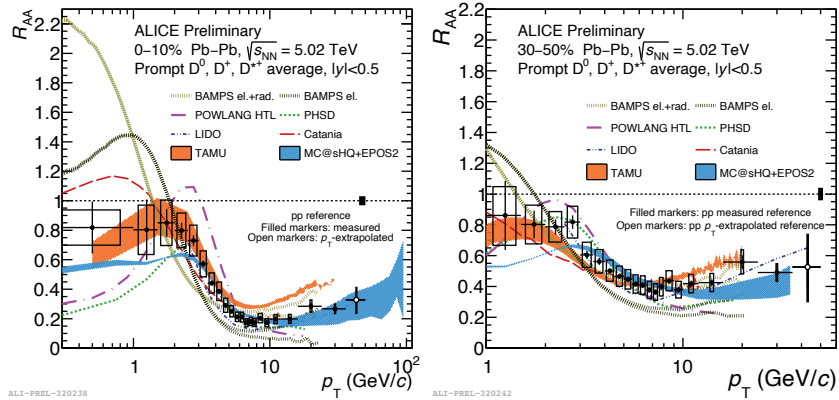


FIGURE 6.23: Average p_T -differential R_{AA} of prompt D^0 , D^+ and D^{*+} mesons in the 0–10% centrality class (left panel) and in the 30–50% centrality class (right panel) compared to transport models [18, 20, 21, 23, 55, 60, 61].

In figure 6.23, the average R_{AA} of non-strange D mesons is compared with the transport models. For $p_T < 10$ GeV/ c , the LIDO [60], Catania [61], MC@sHQ+EPOS2 [20], TAMU [18], and BAMPS el.+rad. [21] provide a fair description of the data in central collisions, while POWLANG [55] and BAMPS el. models show some tension with respect to the R_{AA} values. The POWLANG and BAMPS el. considered only collisional interactions in the model calculations while for the LIDO, Catania,

MC@sHQ+EPOS2, TAMU, and BAMPS el.+rad. include both collisional and radiative energy loss processes. At high transverse momentum above 10 GeV/ c in central collisions, only the MC@sHQ and BAMPS el.+rad. models provide an excellent description of the data. Both models, the MC@sHQ and BAMPS el.+rad., consider radiative and collisional processes in the calculations to describe the interactions of heavy quarks with the medium constituents. In addition, both model calculations use in-vacuum fragmentation of heavy quarks while the MC@sHQ is supplemented by hadronisation via recombination at low p_T region.

In semi-central collisions for $p_T < 10$ GeV/ c , most of the models provide a fair prediction of the R_{AA} values, while the BAMPS el., where radiative energy loss is missing, tends to overshoot the data at low p_T . Moreover, the MC@sHQ, BAMPS el.+rad., LBT and TAMU models describe well the data for $p_T > 10$ GeV/ c in semi-central collisions.

The comparison between the data and models shows that radiative and collisional energy loss are both needed to explain the non-strange D-meson nuclear modification factor. At high p_T , radiative processes are successful to describe the R_{AA} while at low p_T it is well reproduced by collisional processes. In addition at intermediate p_T around 5–8 GeV/ c , it seems the two processes exchange their importance.

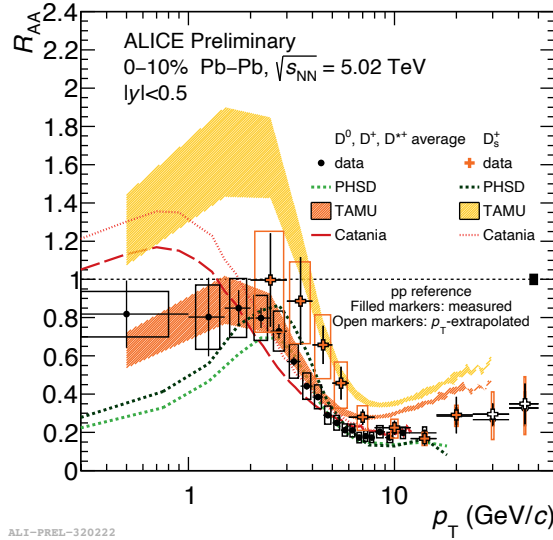


FIGURE 6.24: Average R_{AA} of prompt D^0 , D^+ and D^{*+} mesons and R_{AA} D_s^+ mesons in the 0–10% centrality class compared with PHSD [62], TAMU [63] and Catania [61] models.

The comparison between the average non-strange and strange D-meson (D_s^+) R_{AA} with the model predictions is shown in Fig. 6.24. The strange D-meson enhancement is qualitatively reproduced by models including charm-quark coalescence in a

strangeness-rich medium. The PHSD [62], TAMU [63] and Catania [61] models qualitatively predict the different effects of the strange D-meson R_{AA} . All models describe well the shape of the R_{AA} . The TAMU and PHSD models provide a fair description of the data, while the Catania model underestimates its magnitude. The TAMU and PHSD models include hadronisation mechanism via quark recombination. An enhancement of the strange D-meson yield relative to that of non-strange D mesons at low and intermediate momenta is expected in nucleus-nucleus collisions, if the dominant process of D-meson formation is in-medium hadronization of charm quarks via recombination with light quarks, due to the large abundance of strange quarks in the QGP. An enhanced production of D_s^+ mesons in heavy-ion collisions due to recombination entails a reduction of charm quarks available for hadronization into non-strange D-meson species.

From the comparison between the non-strange and strange D mesons with model predictions, the data suggest that hadronization mechanism of c -quark via recombination in the Quark-Gluon Plasma (QGP) takes place. It means that the hadrons are produced by recombining the quarks which are collectively moving in the QGP. The TAMU model reproduces well the data hinting a larger D_s^+ -meson R_{AA} with respect to that of average non-strange D-meson for $p_T < 10$ GeV/ c , which is expected in case of hadronization via coalescence due to the enhanced production of strange quarks in the QGP.

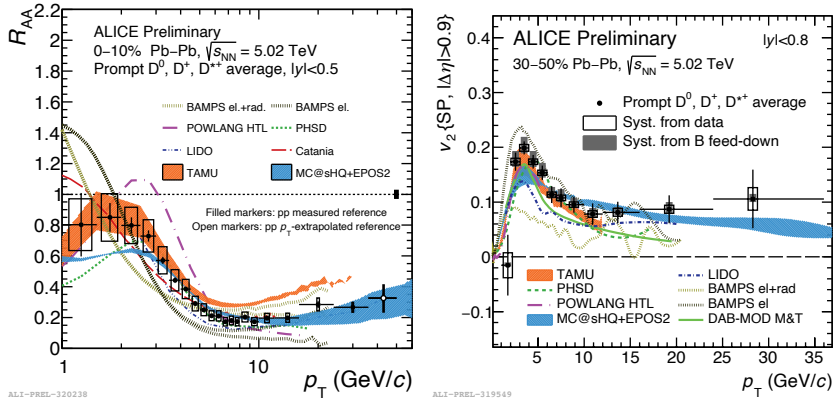


FIGURE 6.25: Average p_T -differential R_{AA} of D^0 , D^+ , and D^{*+} in the 0–10% centrality class (left panel) and the average v_2 in the 30–50% centrality class (right panel) [64], compared to model predictions.

The simultaneous comparison of the average R_{AA} for non-strange D mesons in the 0–10% centrality class (left panel) and v_2 in the 30–50% centrality class (right panel) with transport models is shown in figure 6.25. It can provide an input to models to constrain the implementation of the interaction and hadronisation processes for heavy quarks in the QGP. Most of the models provide a fair description of the data in central events for $p_T < 10$ GeV/ c , while POWLANG [55] and BAMPS [21], in which

the interactions are only described by collisional (i.e. elastic scattering) processes, show some tension with respect to the R_{AA} data points. The TAMU [18] model, with improved space-momentum correlations between charm quarks and underlying hydro medium, describes well the D-meson v_2 for $p_T < 12$ GeV/ c . The MC@sHQ+EPOS2 [20] model provides a fair description of v_2 , as PHSD [23] and TAMU [18] do for $p_T < 12$ GeV/ c , while BAMPS [21] model overestimates the maximum value of v_2 . In addition, the LIDO [60] and DAB-MODE [65] models describe the shape of v_2 but underestimate its magnitude.

6.10 D^{*+} meson nuclear modification factor as a function of centrality

Centrality is an important parameter in studying the properties of QCD matter created at high temperature and energy density. It is related to particle multiplicity produced in the collisions. Centrality is quantified as the average number of participant nucleons in the collisions, $\langle N_{\text{part}} \rangle$, which is estimated with a Monte Carlo Glauber model implementation [29, 30, 31]. The $\langle N_{\text{part}} \rangle$ is the number of nucleons which underwent at least one inelastic nucleon-nucleon collisions. In central collisions, the average number of participant nucleons in the collisions is higher than in more peripheral collisions. Therefore, the created QGP medium is expected to be larger and denser in central collisions with respect to the one in peripheral. Hence, the heavy quarks are expected to lose more energy in central collisions than in peripheral collisions due to the interaction with the larger and denser medium. Therefore, the nuclear modification factor measured in higher centrality classes is expected to be closer to unity with respect to lower centrality classes till virtually should reach the value of about one for 100% centrality events in the assumption of negligible cold nuclear matter effects. By performing the measurement of the nuclear modification factor as a function of centrality, we can investigate the system-size dependence of the in-medium energy loss.

The centrality dependence of the nuclear modification factor in Pb–Pb collisions at $\sqrt{s_{NN}} = 5.02$ TeV was studied in the two transverse momentum intervals $3 < p_T < 5$ GeV/ c and $8 < p_T < 12$ GeV/ c [66]. This study was performed in six centrality classes ranging from 0–10%, 10–20%, 20–30%, 30–50%, 50–60%, and 60–80%. The measurement results of the R_{AA} dependence on the centrality are given in figure 6.26, where R_{AA} is given as a function of the average number of participant nucleons in a collision $\langle N_{\text{part}} \rangle$. In figure 6.26, from right to left on the x -axis, higher $\langle N_{\text{part}} \rangle$ corresponds to more central collisions while lower $\langle N_{\text{part}} \rangle$ corresponds to more peripheral collisions. For $8 < p_T < 12$ GeV/ c , the suppression increases with increasing $\langle N_{\text{part}} \rangle$. The trend of the suppression increases from peripheral to central collisions and, therefore, with increasing energy density.

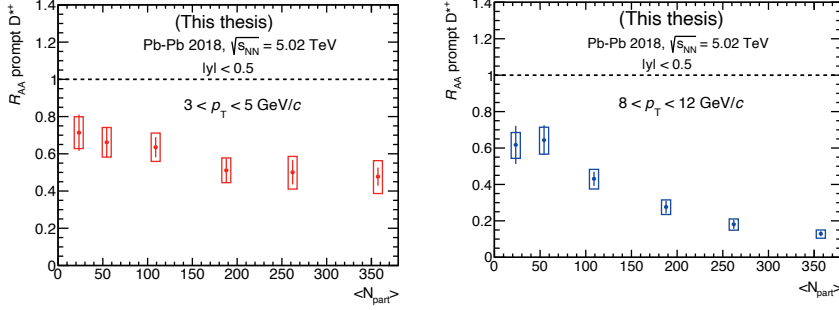


FIGURE 6.26: R_{AA} of D^{*+} meson as a function of the average number of participants $\langle N_{part} \rangle$ at p_T ranges 3–5 GeV/c (left) and 8–12 GeV/c (right) [66]. Statistical (bars) and systematic (empty boxes) uncertainties are shown.

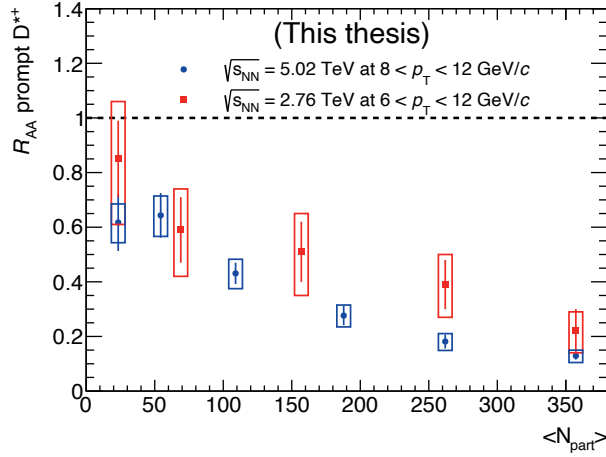


FIGURE 6.27: R_{AA} of D^{*+} meson as a function of the average number of participants measured in Pb–Pb 2018 at $\sqrt{s_{NN}} = 5.02$ TeV (blue) [66] compared with Run 1 at $\sqrt{s_{NN}} = 2.76$ TeV (red) [46]. Bars represent the statistical uncertainties and empty boxes represent the systematic uncertainties. The data points of Run 1 measurement (red) are taken from [46].

Figure 6.27 shows the new measurement R_{AA} as a function of centrality with Pb–Pb 2018 data at $\sqrt{s_{NN}} = 5.02$ TeV compared with the same measurement in LHC Run 1 at $\sqrt{s_{NN}} = 2.76$ TeV [46]. The new measurement is performed in six centrality classes with p_T range 8–12 GeV/c while the old one is measured in five centrality classes ranging from 0–10%, 10–20%, 20–40%, 40–60%, and 60–80% with p_T range 6–12 GeV/c.

In particular the new measurement is promising since now we have more statistics in Pb–Pb 2018 data with respect to Run 1 data. The current measurements have smaller statistical and systematic uncertainties than the one measured at $\sqrt{s_{NN}} = 2.76$ TeV

[46], of a factor 2–5 depending on centrality.

The ΔM invariant-mass of D^{*+} candidate for each centrality in both transverse momentum intervals, $3 < p_T < 5$ GeV/ c and $8 < p_T < 12$ GeV/ c are shown in figures 6.28, 6.29, 6.30, 6.31, 6.32 and 6.33. The measurement presented in this section is still in a preliminary phase and, therefore, is intended as a preview of the possible physics reach. While the central points are final, additional work is still needed on the systematic uncertainties. However, as is clear from the statistical precision achievable, the new measurement can be an additional strong constraint on the theory models, in particular once considered together with the p_T dependence of the R_{AA} and the elliptic flow v_2 measurement.

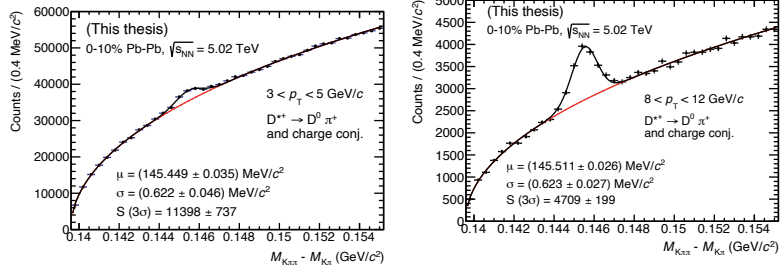


FIGURE 6.28: ΔM invariant-mass of D^{*+} in the 0-10% centrality class in the transverse momentum ranges $3 < p_T < 5$ GeV/c (left) and $8 < p_T < 12$ GeV/c (right) [66].

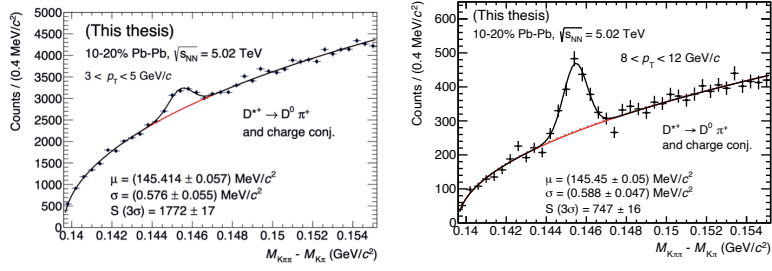


FIGURE 6.29: ΔM invariant-mass of D^{*+} in the 10-20% centrality class in the transverse momentum ranges $3 < p_T < 5$ GeV/c and $8 < p_T < 12$ GeV/c [66].

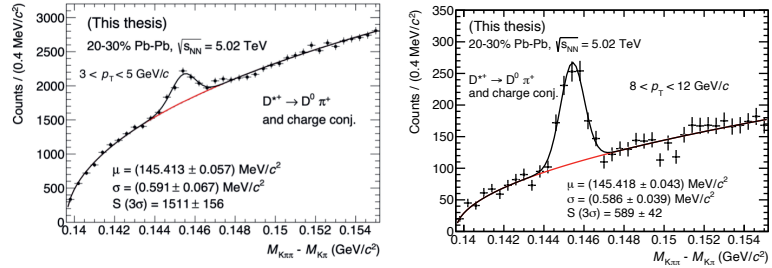


FIGURE 6.30: ΔM invariant-mass of D^{*+} in the 20-30% centrality class in the transverse momentum ranges $3 < p_T < 5$ GeV/c and $8 < p_T < 12$ GeV/c [66].

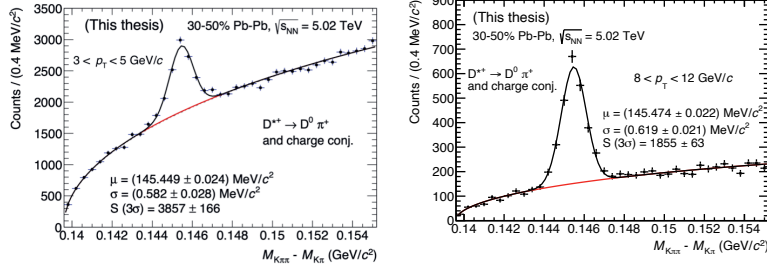


FIGURE 6.31: ΔM invariant-mass of D^{*+} in the 30–50% centrality class in the transverse momentum ranges $3 < p_T < 5$ GeV/c and $8 < p_T < 12$ GeV/c [66].

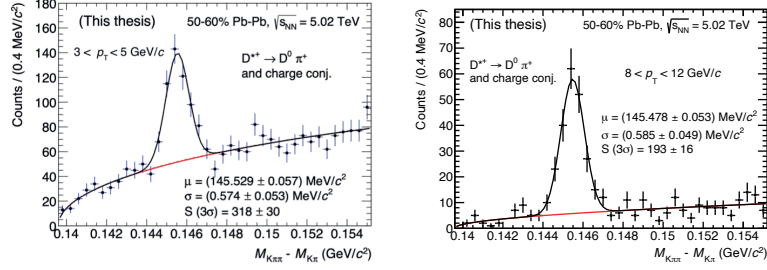


FIGURE 6.32: ΔM invariant-mass of D^{*+} in the 50–60% centrality class in the transverse momentum ranges $3 < p_T < 5$ GeV/c and $8 < p_T < 12$ GeV/c [66].

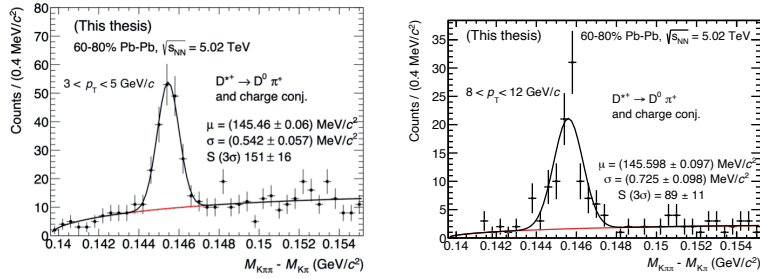


FIGURE 6.33: ΔM invariant-mass of D^{*+} in the 60–80% centrality class in the transverse momentum ranges $3 < p_T < 5$ GeV/c and $8 < p_T < 12$ GeV/c [66].

Chapter 7

Conclusions and outlook

7.1 Conclusions

Measurements of the p_T -differential production yields of prompt D^{*+} -meson in Pb–Pb collisions in the two centrality classes 0–10% and 30–50% at a center-of-mass energy per nucleon pair $\sqrt{s_{NN}} = 5.02$ TeV are presented. For the 2015 data sample, the R_{AA} of the D^{*+} -meson shows minimum values of about 0.2 and about 0.4 in the centrality classes 0–10% and 30–50%, respectively, at transverse momentum range of 6–10 GeV/ c . Furthermore, the average R_{AA} of the non-strange D-meson shows similar values at the same p_T interval. The average R_{AA} values are compatible with those measured at $\sqrt{s_{NN}} = 2.76$ TeV, showing at the same time an improvement in terms of statistical and systematic precision and p_T reach up to 50 GeV/ c in central collisions. The similar R_{AA} values at the two energies were predicted by the Djordjevic model, and it results from the combination of a higher medium temperature with a harder p_T distribution of charm quarks at $\sqrt{s_{NN}} = 5.02$ TeV. While the 2015 measurement is surely good of quality and gives some good hints about charm in medium energy loss, it still misses the precision required to compare with theoretical models and extract more firm conclusions. With this caveat in mind, we decided to analyze the 2018 high-statistic Pb–Pb sample.

The 2018 sample allows us to perform the measurements in finer p_T bins for transverse momentum range lower than 10 GeV/ c . Moreover, the average non-strange D-meson R_{AA} as a function of p_T can go down to 0 p_T at 0–10% centrality classes. The new sample grants an improvement in statistical precision of the order of 3 in the same p_T region opening for the possibility of a more detailed comparison of the non-strange D mesons R_{AA} with the light flavour sector (pions), the strange sector (D_s^+) and with theoretical models including collisional and radiative energy loss. On the comparison with the light flavour sector, we showed a significant difference between the R_{AA} of charged pions and D mesons in the low p_T region. Such difference would be naively expected in case of mass dependence of the in medium energy loss. However, while striking, this difference cannot be directly used to claim a mass dependence due to several factors that can play a role in defining the shape of the R_{AA} in such p_T region

(i.e. cold-nuclear matter effect, fragmentation). Therefore, theoretical calculations are mandatory to draw, once compared with data, more firm conclusions.

The R_{AA} measurements with the latest Pb–Pb data show that radiative and collisional energy loss are needed to explain the non-strange D-meson nuclear modification factor. Radiative processes are successful to describe the R_{AA} at high p_T while at low p_T it is well reproduced by collisional processes with an exchange of importance among the two processes around 5–8 GeV/ c . The comparison between the non-strange and strange D mesons with model predictions indicates that hadronisation mechanism of c -quark via recombination in the Quark-Gluon Plasma (QGP) takes place. It means that the hadrons are produced by recombining the quarks, which are collectively moving in the QGP medium. In particular, the TAMU model reproduces well the D_s^+ -meson enhancement with respect to the average non-strange D-meson R_{AA} for $p_T < 10$ GeV/ c , which is expected in case of hadronisation via coalescence due to the enhanced production of strange quarks in the QGP.

7.2 Future direction

The ALICE Collaboration is preparing an experimental apparatus upgrade, which will also involve the Inner Tracking System (ITS) detector. The main goals of the ALICE ITS detector upgrade are an improved reconstruction of primary and secondary vertices as well as an improved performance in the tracking capability of low-momentum particles. The new ITS detector will be installed during the second LHC long shut-down [67]. In order to achieve the goals, the following changes will be applied:

- Replace the current ITS layers (6 layers) setup with seven layers of pixel detectors with an intrinsic spatial precision of about $5 \times 5 \mu\text{m}^2$, as shown in Fig. 7.1.
- Reduce the material thickness to 0.3% of a radiation length in the innermost layers.
- Use sensors with a pixel size of $27 \times 29 \mu\text{m}^2$, compared to $50 \times 425 \mu\text{m}^2$ in the current pixel detector.

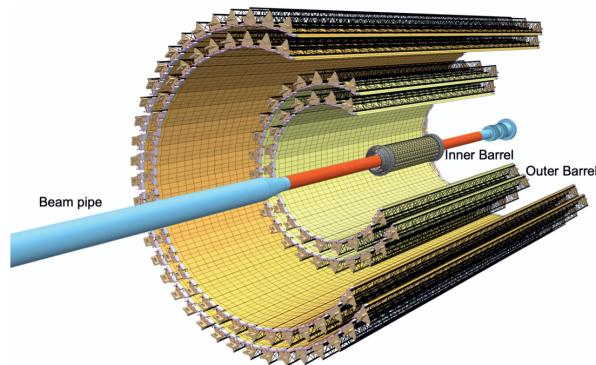


FIGURE 7.1: Layout of the new ITS detector [67].

One of the main features of the new ITS is the new pixel chip (ALPIDE). It requires high spatial resolution, which is $5 \mu\text{m}$, and extremely low material budget, in particular for inner layers. Based on the aforementioned considerations, Monolithic Active Pixel Sensors have been selected as the technology for all layers of the ITS upgrade to replace the existing ITS detector. With the new ITS detector, the impact-parameter resolution will be improved by a factor 3 in the direction transverse to the beam line, in the xy -plane, and by a factor 5 in the longitudinal direction, down to values of about $20 \mu\text{m}$ for tracks with $p_T = 1 \text{ GeV}/c$. Figure 7.2 shows the comparison between the existing impact-parameter resolution (in blue) and the expected one (in red) with the upgraded ITS, obtained with a Monte Carlo simulation, in central Pb–Pb collisions

[67]. In addition, figure 7.3 shows the ITS stand-alone tracking efficiency performance for current ITS (in blue) and upgraded ITS (in red) obtained from MC simulations.

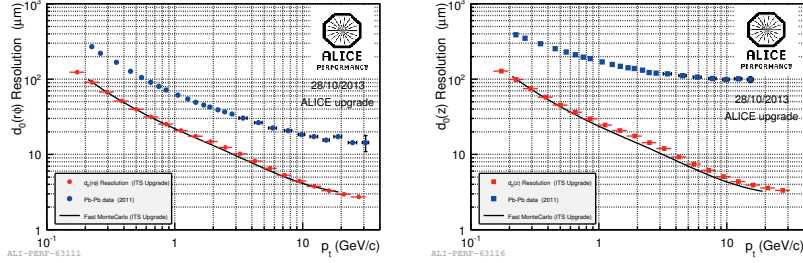


FIGURE 7.2: Impact-parameter resolution for primary charged pions as a function of the transverse momentum for the current ITS and the upgraded ITS in the transverse plane (left panel) and in the longitudinal direction (right panel) [67].

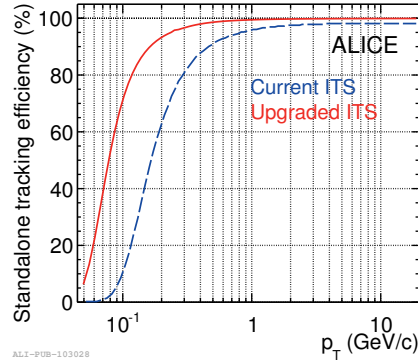


FIGURE 7.3: Stand-alone tracking efficiency for current ITS and upgraded ITS [67].

The new ITS will have seven layers in two separate barrels, Inner Barrel and Outer Barrel as shown in Fig. 7.1. The Inner Barrel consists of the three innermost layers, and the Outer Barrel contains the four outermost layers. The ITS layers are azimuthally segmented in units called Staves, which are mechanically independent. Staves are fixed to a support structure, half-wheel shaped, to form the Half-Layers. The term Stave will be used to refer to the complete detector element. The Stave of the Outer Barrel is further segmented in azimuth in two halves, named Half-Stave, as shown in figure 7.4 on the left. Each Half-Stave consists of several modules glued on a common cooling unit.

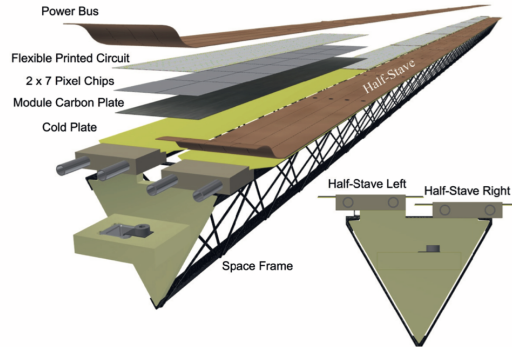


FIGURE 7.4: Schematic exploded view and cross section of the Outer Barrel Stave [67].

Nikhef-Utrecht group took part in chip design, assembling of the detector staves as well as physics studies for the new detector. Nikhef contributed to produce 25% of the Outer Barrel Staves of the upgraded ITS. The assembly process took place in the clean room at Nikhef, Amsterdam. The Outer Barrel assembly was started in March 2018 till 2019. The production rate was 25 Staves in the year before commissioning of the ITS started. It took two weeks to assemble a Stave, which consists of two Half-Stave, meaning that one Half-Stave per week was produced. Once a Stave was fully assembled and tested, then it was delivered to CERN with a special storage transport unit. At the moment this manuscript is written all the staves are completed and shipped at CERN. Figure 7.5 shows the half Outer Barrel at CERN assembled for test and commissioning. The on-surface commissioning is ongoing with several activities, such as threshold equilibration of the detector, cosmic data taking. In addition, some checks have to be done before installing the new ITS in the ALICE cavern planned in January until March 2021.

During my PhD work, I was involved in the upgrade studies with a particular focus on working on the half-stave assembly in the Nikhef clean room. Figure 7.6 was taken while I was working in the clean room at Nikhef, assembling the Half-Stave. It was posted on CERN and Nikhef social media with the hashtag @FollowFriday campaign. Each Half-Stave consists of a Cold Plate on which a number of Modules are glued, namely four and seven for Middle Layers and Outer Layers, respectively. There are some checks that have to be done before a Half-Stave was assembled, such as performing the quality assurance of the Hybrid Integrated Circuit (HIC), and preparing and testing the HIC. Afterward, the HIC has to be glued on the Carbon Cold Plate and again quality assurance tests need to be performed.

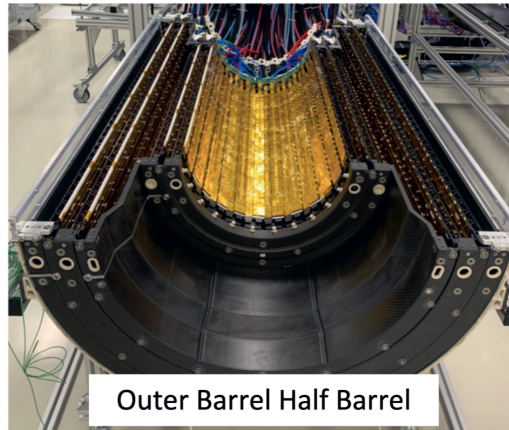


FIGURE 7.5: Half Outer Barrel installed at CERN (photo credit ITS CERN).



FIGURE 7.6: Photo of the week posted at Nikhef and CERN social media with the hashtag @FollowFriday campaign.

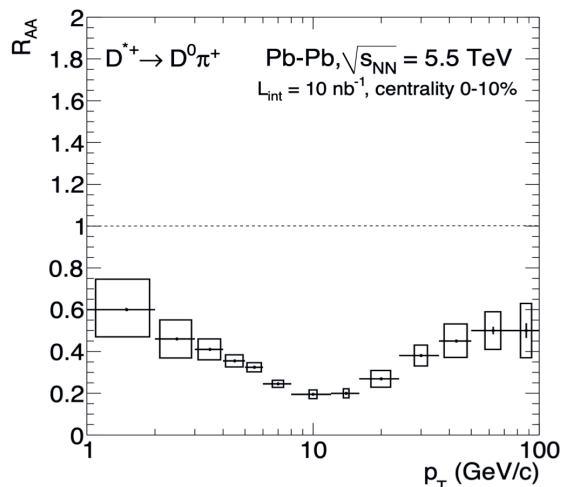


FIGURE 7.7: Performance of the upgraded ITS on the nuclear modification factor of D^{*+} for central Pb–Pb collisions [67].

The new detector once in operation during LHC Run 3 is expected to grant large improvements in every heavy flavour analysis thanks to the largely improved capability of reconstructing decay vertices. In particular, figure 7.7 shows the expected performance on the nuclear modification factor as a function of transverse momentum of D^{*+} with the upgraded ITS [67] for an integrated luminosity of 10 nb^{-1} . The $D^{*+} R_{AA} p_T$ reach is expected to go down to $p_T = 1 \text{ GeV}/c$ and up to $100 \text{ GeV}/c$ with respect to the current measurements. In particular, the statistical precision of the new measurement will be better than 1% in most of the available p_T range, especially at $1 < p_T < 10 \text{ GeV}/c^2$ while the precision of the current measurement is of the order of 5–10%. Therefore, the new ITS will clearly open a precision era on the charm production studies in heavy-ion collisions. A special mention is deserved by the systematic uncertainties in the measurement of figure 7.7. As of now, it is clear that the systematic uncertainties are about factor 10 larger than the statistical one. In principle, such a fact would largely reduce the physics reach of the new measurement. However it is worth to mention that the reported systematics are surely overestimated since they are based on the systematics obtained in the present data measurement. In particular, if we take a look at the $D^{*+} R_{AA}$, the largest contribution of the systematic comes from the tracking efficiency, which is 13% in central Pb–Pb collisions (see Table 6.4 and 6.5).

The second-largest contribution of the systematic is cut variation, which is around 6–12% at low p_T . Of the aforementioned sources, the tracking efficiency is data sample and detector dependent. It can be expected that the new, higher performances and low material budget detector will help in reducing it substantially. For the cut variation, a similar situation can be expected. In particular, the lower material budget,

together with improved detector alignment will allow realistically to bring this source of systematic uncertainty close to 0–1%. Finally, an additional point is that the improved performance of the detector together with the larger data samples expected ($\times 10$) will open the possibility of precise estimation of charmed mesons and baryons production in heavy-ion collisions as well as a detailed study of the direct, elliptic and triangular flow harmonics.

Bibliography

- [1] V. Borka Jovanovic, S.R. Ignjatovic, D. Borka, and P. Jovanovic. Constituent quark masses obtained from hadron masses with contributions of Fermi-Breit and Glazman-Riska hyperfine interactions. *Phys. Rev. D*, 82:117501, 2010.
- [2] X. Zhu, M. Bleicher, S.L. Huang, K. Schweda, Horst Stoecker, N. Xu, and P. Zhuang. D anti-D correlations as a sensitive probe for thermalization in high-energy nuclear collisions. *Phys. Lett. B*, 647:366–370, 2007.
- [3] K.A. Olive. Review of particle physics. *Chinese Physics C*, 40(10):100001, oct 2016.
- [4] Standard model figure. <https://www.physik.uzh.ch/en/researcharea/lhcb/outreach/StandardModel.html>, August 2020.
- [5] George Sterman, John Smith, John C. Collins, James Whitmore, Raymond Brock, Joey Huston, Jon Pumplin, Wu-Ki Tung, Hendrik Weerts, Chien-Peng Yuan, Stephen Kuhlmann, Sanjib Mishra, Jorge G. Morfin, Fredrick Olness, Joseph Owens, Jianwei Qiu, and Davison E. Soper. Handbook of perturbative qcd. *Rev. Mod. Phys.*, 67:157–248, Jan 1995.
- [6] Antonin Maire. Phase diagram of QCD matter : Quark-Gluon Plasma. General Photo, Jun 2015.
- [7] Markus H. Thoma and Miklos Gyulassy. Quark Damping and Energy Loss in the High Temperature QCD. *Nucl. Phys. B*, 351:491–506, 1991.
- [8] Eric Braaten and Markus H. Thoma. Energy loss of a heavy fermion in a hot plasma. *Phys. Rev. D*, 44:1298–1310, 1991.
- [9] Eric Braaten and Markus H. Thoma. Energy loss of a heavy quark in the quark - gluon plasma. *Phys. Rev. D*, 44(9):2625, 1991.
- [10] Miklos Gyulassy and Michael Plumer. Jet Quenching in Dense Matter. *Phys. Lett. B*, 243:432–438, 1990.
- [11] R. Baier, Yuri L. Dokshitzer, Alfred H. Mueller, S. Peigne, and D. Schiff. Radiative energy loss and p(T) broadening of high-energy partons in nuclei. *Nucl. Phys. B*, 484:265–282, 1997.
- [12] David d’Enterria. *Jet quenching*, volume 23, page 471. 2010.

-
- [13] Magdalena Djordjevic and Miklos Gyulassy. Where is the charm quark energy loss at RHIC? *Phys. Lett. B*, 560:37–43, 2003.
 - [14] P. Braun-Munzinger. Quarkonium production in ultra-relativistic nuclear collisions: Suppression versus enhancement. *J. Phys. G*, 34:S471–478, 2007.
 - [15] Magdalena Djordjevic and Marko Djordjevic. Predictions of heavy-flavor suppression at 5.1 tev pb + pb collisions at the cern large hadron collider. *Phys. Rev. C*, 92:024918, Aug 2015.
 - [16] Jiechen Xu, Jinfeng Liao, and Miklos Gyulassy. Bridging Soft-Hard Transport Properties of Quark-Gluon Plasmas with CUJET3.0. *JHEP*, 02:169, 2016.
 - [17] Zhong-Bo Kang, Felix Ringer, and Ivan Vitev. Effective field theory approach to open heavy flavor production in heavy-ion collisions. *JHEP*, 03:146, 2017.
 - [18] Min He, Rainer J. Fries, and Ralf Rapp. Heavy Flavor at the Large Hadron Collider in a Strong Coupling Approach. *Phys. Lett.*, B735:445–450, 2014.
 - [19] Min He, Hendrik van Hees, Pol B. Gossiaux, Rainer J. Fries, and Ralf Rapp. Relativistic langevin dynamics in expanding media. *Phys. Rev. E*, 88:032138, Sep 2013.
 - [20] Marlene Nahrgang, Joerg Aichelin, Pol Bernard Gossiaux, and Klaus Werner. Influence of hadronic bound states above T_c on heavy-quark observables in Pb + Pb collisions at the CERN Large Hadron Collider. *Phys. Rev.*, C89(1):014905, 2014.
 - [21] Jan Uphoff, Oliver Fochler, Zhe Xu, and Carsten Greiner. Elastic and radiative heavy quark interactions in ultra-relativistic heavy-ion collisions. *J. Phys.*, G42(11):115106, 2015.
 - [22] Shanshan Cao, Tan Luo, Guang-You Qin, and Xin-Nian Wang. Heavy and light flavor jet quenching at RHIC and LHC energies. *Phys. Lett.*, B777:255–259, 2018.
 - [23] Taesoo Song, Hamza Berrehrah, Daniel Cabrera, Wolfgang Cassing, and Elena Bratkovskaya. Charm production in Pb + Pb collisions at energies available at the CERN Large Hadron Collider. *Phys. Rev.*, C93(3):034906, 2016.
 - [24] P. Braun-Munzinger and J. Wambach. The Phase Diagram of Strongly-Interacting Matter. *Rev. Mod. Phys.*, 81:1031–1050, 2009.
 - [25] A. Andronic et al. Heavy-flavour and quarkonium production in the LHC era: from proton–proton to heavy-ion collisions. *Eur. Phys. J. C*, 76(3):107, 2016.
 - [26] Fu-Ming Liu and Sheng-Xu Liu. Quark-gluon plasma formation time and direct photons from heavy ion collisions. *Phys. Rev. C*, 89(3):034906, 2014.
 - [27] Shreyasi Acharya et al. Measurement of prompt D^0 , D^+ , D^{*+} , and D_S^+ production in p–Pb collisions at $\sqrt{s_{NN}} = 5.02$ TeV. *JHEP*, 12:092, 2019.

- [28] Jaroslav Adam et al. D -meson production in p -Pb collisions at $\sqrt{s_{NN}}=5.02$ TeV and in pp collisions at $\sqrt{s}=7$ TeV. *Phys. Rev. C*, 94(5):054908, 2016.
- [29] Michael L. Miller, Klaus Reygers, Stephen J. Sanders, and Peter Steinberg. Glauber modeling in high energy nuclear collisions. *Ann. Rev. Nucl. Part. Sci.*, 57:205–243, 2007.
- [30] R.J. Glauber and G. Matthiae. High-energy scattering of protons by nuclei. *Nucl. Phys. B*, 21:135–157, 1970.
- [31] B. Alver, M. Baker, C. Loizides, and P. Steinberg. The PHOBOS Glauber Monte Carlo. 5 2008.
- [32] C. Loizides, J. Nagle, and P. Steinberg. Improved version of the PHOBOS Glauber Monte Carlo. *SoftwareX*, 1-2:13–18, 2015.
- [33] Large hadron collider sketch. www.nikhef.nl/en/news/ten-years-on-and-the-lhc-accelerator-is-still-not-done-colliding, August 2020.
- [34] K Aamodt et al. Alignment of the ALICE Inner Tracking System with cosmic-ray tracks. *JINST*, 5:P03003, 2010.
- [35] Betty Bezverkhny Abelev et al. Performance of the ALICE Experiment at the CERN LHC. *Int. J. Mod. Phys. A*, 29:1430044, 2014.
- [36] J. Alme et al. The ALICE TPC, a large 3-dimensional tracking device with fast readout for ultra-high multiplicity events. *Nucl. Instrum. Meth. A*, 622:316–367, 2010.
- [37] Luigi Rolandi Walter Blum and Werner Riegler. *article Detection with Drift Chambers, 2nd edn.* Springer-Verlag, <http://www.springer.com/physics/elementary/book/978-3-540-76683-4>, 2008.
- [38] E. Abbas et al. Performance of the ALICE VZERO system. *JINST*, 8:P10016, 2013.
- [39] Centrality dependence of the charged-particle multiplicity density at midrapidity in Pb-Pb collisions at $\sqrt{s_{NN}} = 5.02$ TeV. Dec 2015.
- [40] Betty Abelev et al. Centrality determination of Pb-Pb collisions at $\sqrt{s_{NN}} = 2.76$ TeV with ALICE. *Phys. Rev. C*, 88(4):044909, 2013.
- [41] Torbjorn Sjostrand, Stephen Mrenna, and Peter Z. Skands. PYTHIA 6.4 Physics and Manual. *JHEP*, 05:026, 2006.
- [42] Xin-Nian Wang and Miklos Gyulassy. HIJING: A Monte Carlo model for multiple jet production in p p, p A and A A collisions. *Phys. Rev.*, D44:3501–3516, 1991.

- [43] René Brun, F. Bruyant, Federico Carminati, Simone Giani, M. Maire, A. McPherson, G. Patrick, and L. Urban. GEANT Detector Description and Simulation Tool. 1994.
- [44] Matteo Cacciari, Mario Greco, and Paolo Nason. The p(T) spectrum in heavy flavor hadroproduction. *JHEP*, 05:007, 1998.
- [45] D. J. Lange. The EvtGen particle decay simulation package. *Nucl. Instrum. Meth.*, A462:152–155, 2001.
- [46] Betty Abelev et al. Suppression of high transverse momentum D mesons in central Pb-Pb collisions at $\sqrt{s_{NN}} = 2.76$ TeV. *JHEP*, 09:112, 2012.
- [47] Jaroslav Adam et al. Transverse momentum dependence of D-meson production in Pb-Pb collisions at $\sqrt{s_{NN}} = 2.76$ TeV. *JHEP*, 03:081, 2016.
- [48] Jaroslav Adam et al. Measurement of D_s^+ production and nuclear modification factor in Pb-Pb collisions at $\sqrt{s_{NN}} = 2.76$ TeV. *JHEP*, 03:082, 2016.
- [49] Jaroslav Adam et al. Centrality dependence of high- p_T D meson suppression in Pb-Pb collisions at $\sqrt{s_{NN}} = 2.76$ TeV. *JHEP*, 11:205, 2015. [Addendum: JHEP06,032(2017)].
- [50] Matteo Cacciari, Stefano Frixione, and Paolo Nason. The p(T) spectrum in heavy flavor photoproduction. *JHEP*, 03:006, 2001.
- [51] S. Acharya et al. Measurement of D^0 , D^+ , D^{*+} and D_s^+ production in Pb-Pb collisions at $\sqrt{s_{NN}} = 5.02$ TeV. *JHEP*, 10:174, 2018.
- [52] Shreyasi Acharya et al. Measurement of D-meson production at mid-rapidity in pp collisions at $\sqrt{s} = 7$ TeV. *Eur. Phys. J.*, C77(8):550, 2017.
- [53] Matteo Cacciari, Stefano Frixione, Nicolas Houdeau, Michelangelo L. Mangano, Paolo Nason, and Giovanni Ridolfi. Theoretical predictions for charm and bottom production at the LHC. *JHEP*, 10:137, 2012.
- [54] Betty Bezverkhny Abelev et al. Measurement of prompt D-meson production in $p - Pb$ collisions at $\sqrt{s_{NN}} = 5.02$ TeV. *Phys. Rev. Lett.*, 113(23):232301, 2014.
- [55] A. Beraudo, A. De Pace, M. Monteno, M. Nardi, and F. Prino. Heavy flavors in heavy-ion collisions: quenching, flow and correlations. *Eur. Phys. J.*, C75(3):121, 2015.
- [56] Gao-Liang Zhou, Zheng-Xin Yan, Xin Zhang, and Feng Li. Glauber Gluon Effects in Soft Collinear Factorization. 8 2017.
- [57] Shreyasi Acharya et al. Measurement of D^0 , D^+ , D^{*+} and D_s^+ production in pp collisions at $\sqrt{s} = 5.02$ TeV with ALICE. *Eur. Phys. J.*, C79(5):388, 2019.

-
- [58] S. Acharya et al. Transverse momentum spectra and nuclear modification factors of charged particles in pp, p-Pb and Pb-Pb collisions at the LHC. *JHEP*, 11:013, 2018.
- [59] Magdalena Djordjevic. Heavy flavor puzzle at LHC: a serendipitous interplay of jet suppression and fragmentation. *Phys. Rev. Lett.*, 112(4):042302, 2014.
- [60] Weiyao Ke, Yingru Xu, and Steffen A. Bass. Linearized Boltzmann-Langevin model for heavy quark transport in hot and dense QCD matter. *Phys. Rev.*, C98(6):064901, 2018.
- [61] Salvatore Plumari, Vincenzo Minissale, Santosh K. Das, G. Coci, and V. Greco. Charmed Hadrons from Coalescence plus Fragmentation in relativistic nucleus-nucleus collisions at RHIC and LHC. *Eur. Phys. J.*, C78(4):348, 2018.
- [62] Taesoo Song, Hamza Berrehrah, Daniel Cabrera, Juan M. Torres-Rincon, Laura Tolos, Wolfgang Cassing, and Elena Bratkovskaya. Tomography of the Quark-Gluon-Plasma by Charm Quarks. *Phys. Rev.*, C92(1):014910, 2015.
- [63] Min He and Ralf Rapp. Hadronization and Charm-Hadron Ratios in Heavy-Ion Collisions. *Phys. Rev. Lett.*, 124(4):042301, 2020.
- [64] Shreyasi Acharya et al. D -meson azimuthal anisotropy in midcentral Pb-Pb collisions at $\sqrt{s_{NN}} = 5.02$ TeV. *Phys. Rev. Lett.*, 120(10):102301, 2018.
- [65] Caio A. G. Prado, Jacquelyn Noronha-Hostler, Roland Katz, Alexandre A. P. Suaide, Jorge Noronha, Marcelo G. Munhoz, and Mauro R. Cosentino. Event-by-event correlations between soft hadrons and D^0 mesons in 5.02 TeV PbPb collisions at the CERN Large Hadron Collider. *Phys. Rev.*, C96(6):064903, 2017.
- [66] Justus van der Velden (Bachelor thesis). *Measurement of the centrality dependent nuclear modification factor of the D^{*+} -meson*. Physics Department, Utrecht University, Domplein 29, 3512 JE Utrecht.
- [67] B Abelev et al and. Technical design report for the upgrade of the ALICE inner tracking system. *Journal of Physics G: Nuclear and Particle Physics*, 41(8):087002, jul 2014.

Summary in English

In this thesis, measurements of the p_T -differential production yields of prompt D^{*+} -meson in Pb–Pb collisions in the two centrality classes 0–10% and 30–50% at a center-of-mass energy per nucleon pair $\sqrt{s_{NN}} = 5.02$ TeV are presented. The high statistic data sample collected at the end of 2018 by the ALICE collaboration, allows us to perform the measurements in finer p_T bins for transverse momentum range lower than 10 GeV/ c . Moreover, the average non-strange D-meson R_{AA} (nuclear modification factor) as a function of p_T can go down to 0 p_T at 0–10% centrality classes. The new sample grants an improvement in statistical precision of the order of 3, with respect to 2015 data, opening for the possibility of a more detailed comparison of the non-strange D mesons R_{AA} with the light flavour sector (pions), the strange sector (D_s^+) and with theoretical models including collisional and radiative energy loss. On the comparison with the light flavour sector, we showed a largely significative difference between the R_{AA} of charged pions and D mesons in the low p_T region. Such difference would be naively expected in case of mass dependence of the in medium energy loss. However, while striking, this difference can not be directly used to claim a mass dependence due to several factors that can play a role in the defining the shape of the R_{AA} in such p_T region (i.e. cold-nuclear matter effect, fragmentation). Therefore theoretical calculations are mandatory to draw, once compared with data, more firm conclusions.

The nuclear modification factor (R_{AA}) measurements with the latest Pb–Pb data show that radiative and collisional energy loss are needed to explain the non-strange D-meson nuclear modification factor. Radiative processes are successful to describe the R_{AA} at high p_T while at low p_T it is well reproduced by collisional processes with an exchange of importance among the two processes around 5–8 GeV/ c . The comparison between the non-strange and strange D mesons with model predictions indicates that hadronisation mechanism of c -quark via recombination in the Quark-Gluon Plasma (QGP) takes place. It means that the hadrons are produced by recombining the quarks which are collectively moving in the QGP medium. In particular, the TAMU model reproduces well the D_s^+ -meson enhancement with respect to the average non-strange D-meson R_{AA} for $p_T < 10$ GeV/ c , which is expected in case of hadronisation via coalescence due to the enhanced production of strange quarks in the QGP.

Samenvatting in het Nederlands

In dit proefschrift worden metingen gepresenteerd van de p_T -differentiële productieopbrengst van prompt D^{*+} mesonen in Pb–Pb botsingen in de twee centraliteitsintervallen 0–10% en 30–50% bij een massamiddelpuntsenergie van $\sqrt{s_{NN}} = 5.02$ TeV per nucleonenpaar. Voor deze metingen zijn Pb-Pb data verzameld door de ALICE-samenwerking geanalyseerd. De grote hoeveelheid data die eind 2018 door de ALICE-detector is verzameld, stelt ons in staat om de metingen uit te voeren in smalle p_T -intervallen voor transversale momenta van minder dan 10 GeV/ c . Bovendien kan de gemiddelde R_{AA} (nucleaire modificatiefactor) als functie van p_T voor niet-Strange D-meson gemeten worden tot 0 p_T bij een centraliteitsinterval van 0–10%.

De nieuwe data geeft een verbetering van de statistische precisie met een factor van 3 in hetzelfde p_T -gebied. Dit opent de mogelijkheid van een meer gedetailleerde vergelijking van de niet-Strange D-meson R_{AA} met de lichte smaaksector (pionen), de Strange-sector (D_s^+) en theoretische modellen waarin botsings- en stralingsenergieverlies verwerkt zijn. In de vergelijking met de lichte smaaksector, tonen we dat er een grotendeels significant verschil is tussen de R_{AA} van geladen pionen en D-mesonen in het lage p_T -gebied. Een dergelijk verschil zou naïef gezien te verwachten zijn in geval van massa-afhankelijkheid van energieverlies in het medium. Hoewel het verschil opvalt, kan dit niet direct worden gebruikt om een massa-afhankelijkheid te claimen vanwege verschillende factoren die een rol kunnen spelen bij het bepalen van de vorm van de R_{AA} in een dergelijk p_T -gebied (d.w.z. effect van koude nucleaire materie, fragmentatie). Daarom zijn theoretische berekeningen noodzakelijk om, wanneer vergeleken met data, stevigere conclusies te trekken.

De nucleaire modificatiefactor R_{AA} metingen met de nieuwste Pb–Pb data laten zien dat zowel stralings- als botsingsenergieverlies nodig zijn om de niet-Strange D-meson nucleaire modificatiefactor te verklaren. Stralingsprocessen zijn succesvol om de R_{AA} te beschrijven bij hoge p_T , terwijl de R_{AA} bij lage p_T goed wordt gereproduceerd door botsingsprocessen. Het belang van de bijdragen van deze processen wisselt rond 5–8 GeV/ c . De vergelijking tussen de niet-Strange en Strange D-mesonen met modelvoorspellingen geeft aan dat het hadronisatiemechanisme van c -quark via recombinitie in het Quark-Gluon Plasma (QGP) plaatsvindt. Dit betekent dat de hadronen worden geproduceerd doordat de quarks die gezamenlijk in het QGP-medium bewegen zich opnieuw samenvoegen. In het bijzonder reproduceert het TAMU-model goed de D_s^+ -mesonversterking met betrekking tot de gemiddelde niet-Strange D-meson R_{AA} voor

$p_T < 10 \text{ GeV}/c$, die wordt verwacht in het geval van hadronisatie via coalescentie als gevolg van de verhoogde productie van Strange quarks in het QGP.

Curriculum Vitae

- **2016–2021**

PhD in Particle Physics, Utrecht University

Thesis: Measurement of the D^{*+} -meson production in Pb–Pb collisions at $\sqrt{s_{\text{NN}}} = 5.02$ TeV with ALICE

- **2012–2015**

MSc in Theoretical Physics, University of Indonesia

Thesis: Point-Coupling Model Density Dependent Coupling Constants

- **2007–2011**

BSc in Theoretical Physics, University of Indonesia

Thesis: Dirac Quantisation for Interaction Lagrangian with Time Derivative Terms

Acknowledgements

Alhamdulillah. Thanks to Allah swt for everything.

Thanks to my supervisor, Alessandro, who took great patience with everything and introduced me to ALICE. Thank you for the opportunity given to me working on the data analysis with ALICE at Utrecht group.

Thanks to Raimond for welcoming me to the ALICE Nikhef-Utrecht group. Thanks for the late. Andre, your kindness, knowledge, and passion to contribute to science. I will never forget you.

Thanks to all my colleagues, Thomas, Marta, Henrique, Lennart, Luuk, Auro, Zhanna, Davide (Lodato), Davide (Caffari), Rihan, Cristina, Barbara, Jacopo, Annelis, Peter, Olaf, Justus, Rene, Thon, Monique and others.

Alhamdulillah. Puji dan syukur kepada Allah SWT, yang telah memberikan saya segalanya hingga saat ini. Salah satunya ialah ilmu pengetahuan yang saya dapat selama menempuh program PhD di Utrecht. Terima kasih kepada orang tua saya, Bahriah dan Ruslan (RB), tanpa doa mereka rasanya mustahil saya bisa menempuh pendidikan di luar negeri, di Belanda selama 4 tahun. Saat pertama kali diberi tahu kalau saya diterima di Utrecht, rasanya seperti mimpi. Terima kasih kepada istri saya, Sri Devi Herawati yang telah bersabar selama ini dan mendukung saya.

Terima kasih kepada keluarga besar SGB, yang telah memberikan tempat selama saya di Utrecht, tempat berkumpul dengan warga muslim di Utrecht dan sesama pelajar baik dalam rangka ibadah maupun kegiatan keislaman lainnya.

Terima kasih kepada kang Afil dan kang Yana sudah berbagi pengalaman hidup. Saya banyak belajar dari pengalaman kalian. Kesulitan yang saya alami, masih jauh lebih ringan dari apa yang sudah kalian alami. Hal tersebut terus memotivasi saya bahwa setiap orang memiliki tantangan dan cerita hidup masing-masing dan jangan pernah menganggap diri kita lebih hebat dari orang lain hanya karena status sosial, harta atau jabatan yang kita miliki.

Alhamdulillah. Thanks to Allah, my parents and everyone.

